Department of Precision and Microsystems Engineering

Pull-out force of grippers with initially-curved fingers based on Pseudo-Rigid Body modelling

Mark Kuntz

Report no : 2024.007
Coach : ir. A. Huisjes
Professor : Prof. dr. ir. J.L. Herder
Specialisation : Mechatronic System Design
Type of report : Master Thesis
Date : 13 February 2024

Abstract

This thesis presents the state-of-the art gripping literature and the implementation and extension of an existing Pseudo-Rigid Body Modelling (PRBM) method for modelling initially-curved compliant grippers out of which a circular object is extracted. From the existing literature, challenges are found in the design and evaluation of concepts of initially-curved compliant grippers, mainly involving the relevant design parameters, such as the thickness and enclosing angle of the finger.

The main goal of this thesis is therefore to present and validate the pull-out force modelling for these fingers within defined load conditions to provide comprehensive insights into the relation between important design parameters, such as the enclosing angle and thickness of the finger.

This goal is accomplished by extending an existing 3R PRB-model for initially-curved beams with a fifth link that represents the object and analysing the kinematics and kinetics to determine the relation for the pull-out force of a gripper finger with defined dimensions and a known load case.

This model is validated by designing and building an experimental test setup in which the reaction forces of a initially-curved testpiece of PLA and stainless steel material are measured. Errors for the kinetics between 12 and 32 percent were determined, consisting primarily of systematic errors.

The validated model is used for a parametric study, where relations between relevant design parameters, such as the enclosing angle and thickness of an initially-curved compliant gripper finger, are determined and visualized in a design chart that are be applied in the design of an initially-curved enclosing gripper prototype.

Preface

This thesis concludes my master's degree in High-Tech Engineering, a track of the Mechanical Engineering master at the Delft University of Technology and therefore also my time as a student. This final project was a great way to implement all theoretical knowledge gained throughout the studies in a practical application.

First of all, I would like to thank my daily supervisor, Ad Huisjes, for his guidance throughout the project, as well as my professor, Just Herder, for his advice and expertise on the project. Furthermore, I would like to thank my fellow students in our research group for their collaborative feedback and inspiring insights in the weekly meetings. Lastly, I would like to thank my friends and family for their support throughout my studies.

Mark Kuntz
Delft, February 2024

Contents

Nomenclature

Abbreviations

Abbreviation	Definition
COM	Communication port
CNC	Computer numerical control
DoF	Degrees of freedom
FBD	Free body diagram
FEM	Finite-Element Modelling
MCA	Multi-criteria analysis
NPR	Negative Poisson Ratio
PE	Polyethylene
PES	Polyethersulfone
PETG	Polyethylene terephthalate glycol
PRBM	Pseudo-Rigid Body Modelling
PLA	Polylactic acid
SMA	Shape Memory Alloy
ZPR	Zero Poisson Ratio

Symbols

Symbol	Definition	Unit
α	Trapezium angles in the kinematic solving of the extended application of the model.	$[rad]$
c	Scaling constant for algorithm boundaries	$[-]$
$\delta\theta$	Deformation angle of the PRB mechanism.	$[rad]$
Δy	Step size of the displacement vector y.	$[m]$
e	The percentile error between the maximum force values of the experimental and simulated results.	$[\%]$
$e_{\lvert\Delta\rvert}$	The absolute error between the maximum force values of the experimental and simulated results.	$[N]$
E	Young's modulus.	$[Pa]$
F	Force on the tip of the PRB mechanism.	$[N]$
F_x	x-component of the force on the tip of the PRB mechanism.	$[N]$
F_x^i	x-component of the force contributed by the inner linkage in the extended application of the model.	$[N]$

Symbol	Definition	Unit
F_x^o	x-component of the force contributed by the outer linkage in the extended application of the model.	$[N]$
F_y	y-component of the force on the tip of the PRB mechanism. Pull-out force.	$[N]$
F_y^e	Scaled maximum pull-out force of the experimental results for error determination.	$[N]$
F_y^i	y-component of the force contributed by the inner linkage in the extended application of the model.	$[N]$
F_y^o	y-component of the force contributed by the outer linkage in the extended application of the model.	$[N]$
F_y^s	Scaled maximum pull-out force of the simulated results for error determination.	$[N]$
F_z	Force limit in parametric study.	$[N]$
g	Gravitational constant.	$[m/s^2]$
h	Thickness of the backbone.	$[m]$
I	The area moment of inertia of the backbone.	$[m^4]$
C_e	Error scaling factor.	$[-]$
K_θ	Stiffness of the torsion springs at the joints of the PRB mechanism.	$[N/m]$
K_θ^i	Stiffness of the torsion springs at the joints of inner linkage in the extended application of the model.	$[N/m]$
K_θ^o	Stiffness of the torsion springs at the joints of outer linkage in the extended application of the model.	$[N/m]$
k_θ	Pseudo-stiffness of the torsion springs at the joints of the PRB mechanism.	$[-]$
l	Vector loop lengths.	$[m]$
l_b	Lower boundary of the optimization algorithm.	$[rad]$
l_i	Link length of the inner linkage in the extended application of the model.	$[m]$
l_o	Link length of the outer linkage in the extended application of the model.	$[m]$
L	Arc length of the initially-curved finger.	$[m]$
L_i	Arc length of the inner linkage in the extended application of the model.	$[m]$
L_o	Arc length of the outer linkage in the extended application of the model.	$[m]$
M	Moment on the tip of the PRB mechanism.	$[Nm]$
m	Mass of the object.	$[kg]$
n	Ratio between x- and y-components of force F.	$[-]$
n_b	Number of backbones.	$[-]$
n_e	Ratio between the difference of the measured force and displacement of two data points in the Young's modulus test.	$[N]$

Symbol	Definition	Unit
n_f	Number of fingers in the parametric study.	$[-]$
n_i	Interpolation constant.	$[-]$
R	Radius of the object.	$[m]$
R_i	Radius of the inner linkage in the extended application of the model.	$[m]$
R_o	Radius of the outer linkage in the extended application of the model.	$[m]$
t	Distance between inner and outer linkage in the extended application of the model.	$[m]$
T	Reaction torque due to the PRB torsion springs.	$[Nm]$
u_b	Upper boundary of the optimization algorithm.	$[rad]$
V	Potential energy of the torsion springs at the joints of the PRB mechanism.	$[J$
w	Width of the backbone.	$[m]$
X_{tip}	x-coordinate of the tip of the mechanism.	$[m]$
Y_{tip}	y-coordinate of the tip of the mechanism.	$[m]$
y	Displacement of the object in the y-direction.	$[m]$
y_e	Ending point of the displacement vector y.	$[m]$
y_s	Starting point of the displacement vector y.	$[m]$
γ	Pseudo-length of the links of the PRB mechanism.	$[-]$
$\delta\theta$	Deformation angle of the PRB mechanism.	$[rad]$
ζ	Initial angle of the PRB mechanism.	$[rad]$
θ	Vector loop angles w.r.t. the x-axis	$[rad]$
θ_{tip}	Exit angle of the tip of the mechanism.	$[rad]$
ϕ	Angle of force F w.r.t. the x-axis.	$[rad]$
ψ	Enclosing angle of the backbone.	$[rad]$

1

Introduction

The agri-food industry is undergoing rapid technological advancements, particularly in the domain of automated food grasping and distribution, aiming to enhance efficiency, hygiene, and safety. Developing grippers for grasping robots is one of the big challenges in this automation topic, as the agri-food industry contains objects that are hard to grasp, due to their changing geometry, hard-to-reach locations, slippery surfaces, and fragility. Therefore, it is important to design grippers that provide low damage to the object and environment, while functioning in cluttered environments.

Several types of grippers exist, categorized as force-closed grippers and form-closed grippers, often used with fingers encompassing the object. These fingers can comprise rigid linkages, soft robotic bellows, or be a compliant mechanism. The latter gain their motion from elastic deformation and are therefore gaining popularity as scientists see the advantages of these mechanisms, such as the use of monolithic mechanisms, that eliminate the use of lubrication and minimize wear, simplified manufacturing, which reduces cost and weight, high performance, which increases precision and shape-adaptive abilities, which reduce the high force peaks and therefore minimize damage. Compliant mechanisms are found in several gripper designs, such as the fin ray gripper, topology-optimized structures, and initially-curved fingers. The latter is very suitable for agri-food grippers, as they encompass the object without applying force on the surface. Therefore, they are suitable for grasping fragile objects in a cluttered environment. Strategies to further reduce undesirable forces on the object and environment include using the principle of zero-slip in design, such as the implementation of eversion mechanisms, and sleeve mechanics to reduce traction at the surface of the object and its surrounding environment.

The main challenge of incorporating the existing initially-curved gripper technology is that the pull-out force for an initially-curved finger with a defined enclosing angle and thickness is unknown beforehand. Knowing the pull-out force is crucial to evaluate the performance of the gripper, as it is a measure of the maximum payload of a gripper before an object escapes the fingers. Essential design parameters, such as the enclosing angle and thickness of the gripper finger, directly influence the pull-out force and therefore exert a substantial influence on the evaluation of performance metrics during the generation of concepts for comprehensive gripper designs.

Therefore, the goal of this study is to present and validate the pull-out force modelling for an initially-curved gripper with a specified enclosing angle and thickness within defined load conditions to provide insightful comprehension of these critical design parameters in compliant gripper design, through a parametric study.

To reach this goal, a model-based approach will be adopted, in which pseudo-rigid body modeling (PRBM) is used as the foundational framework, which will be implemented such that it applies to compliant gripper design. PRB-modelling offers advantages over other modeling methods, as it is parametric-based and enables rapid and accurate computations of complex non-linear force-deflection behavior, making it suitable for parameter-based conceptual design.

Existing PRB models offer a suitable foundation for this model-based approach. However, implementing these models for pull-out force modelling is challenging, as these models often determine the kinematics of a mechanism by applying a load to the mechanism, while when applying these models to gripper design, the force is the variable that has to be determined due to the extraction of an object that deforms the mechanism. An existing PRB-model, specifically designed for analyzing the kinematics and kinetics associated with extracting a spherical object from initially-curved gripper fingers, by modelling the motion of the object as a fifth rigid link connected to the tip of the pseudo linkage. The model is developed for a spherical object, modelled as a planar disk, that is extracted from a gripper with initially-curved fingers, that encapsulate the object, while assuming frictionless contact. Due to the parametric-based nature of PRB methods, this implementation enables the evaluation of crucial design parameters through a parametric study. The parametric study is conducted for fingers made of polylactic acid (PLA) and stainless steel materials, comparing the thickness and enclosing angle of the finger for a specified load case, resulting in insightful design charts, that are applied to design an actual gripper prototype.

The structure of this thesis is as follows. In chapter 2 the literature study of state-of-the-art gripper technology for compliant zero-slip grippers in cluttered environments is presented. In chapter 3 a description is given of the transition from the objective that was described in the literature review to the main project focus. In chapter 4 the main methodology for determining the pull-out force for an initially-curved finger is described. In chapter 5 the methodology for validating the developed model is presented. In chapter 6 the necessary steps and variables that are required for the parametric study are described. Following, in chapter 7 the results of the experimental validation and the parametric study are presented. in chapter 8 a comprehensive discussion of the results and method is given as well as suggestions for future research. In chapter 9 the research of this thesis applied to the design of an actual initially-curved gripper prototype. Finally, in chapter 10, the main conclusions of this thesis are presented.

The appendices provide the source code of the used MATLAB models (Appendix A), a different method for determining the kinetics via the implementation of a Jacobian (Appendix B), an elaboration about the designs of the test setup and final gripper prototype (Appendix C), a description about implementing and controlling the stepper motor in the test setup (Appendix D), an elaboration about the different testpieces that were designed (Appendix E), an elaboration of the test to determine the Young's modulus of a 3D printed PLA testpiece (Appendix F), a visualization of the LABVIEW environment and code for acquiring test data (Appendix G), an elaboration about further results of the parametric study (Appendix H), an extended implementation of the model for a complex gripper design (Appendix I) and finally the detailed drawings for the part of the final prototype (Appendix J).

2

Zero-slip compliant robotic manipulators for the agri-food industry: a review

2.1. Introduction

In the agri-food sector, the importance of automation has been increasing in the last years. With continuous growth in world population and higher demands on food quality since the COVID-19 pandemic, it is necessary to make the agri-food sector as efficient and hygienic as possible. [14]
However, it is hard to find enough skilled manual labor in this sector. The work environment has often harsh conditions which makes the work physically exhausting and unappealing.
A solution to this problem is to let robots do the work. Robots are often more efficient and precise than humans, can keep the work going for twenty-four-seven, and are capable of doing dangerous tasks.

The Delft University of Technology has started a program with four other Dutch universities, WUR, TUe, UT, and UvA, named FlexCRAFT, which has the primary focus on improving the functioning of robotics in the agri-food sector. [11]

The focus in the engineering department of the Delft University of Technology is mostly on the mechanical design of the end-effector of the robot. Therefore, in this literature review, the main focus is also on this part of the robot.
The challenge of designing a gripper for the agri-food sector is that it has to be able to grasp and move non-rigid food products that are most of the time fragile and are located in changing environments. Therefore, a compliant design of the gripper would be a possible solution. Compliant grippers have the ability to adapt their shape to the surface of the food object and are due to their low stiffness flexible in propagating through changing environments. Furthermore, the low stiffness has a beneficial aspect of low risk of harming any humans or other food products in the environment.

In this review, further elaboration is done on the existing literature concerning compliant grippers with their application in the agri-food industry, where a more in-depth focus lies on functioning in cluttered environments and minimizing damage to the food products. The main research question is therefore:

*What are the **challenges** in designing a **compliant zero-slip gripper** for the agri-food sector that propagates through a **cluttered environment**?*

The process in this literature research is not linear, which means that not continuously the only focus was on finding literature, but also on gaining knowledge by prototyping and gaining insight into new solutions, which then causes new challenges, which then give a new focus. This is a circular

process which is visualized in Figure 2.1.

Figure 2.1: Illustration of the iterative process in the literature study.

2.2. Literature Retrieval

The literature is retrieved with the help of the main functions that the gripper has to have. These functions are described in the first section of this chapter. The literature that is relevant for certain functions is then elaborated in the further sections.

2.2.1. Main functions

From the research question, the following main functions can be digested:

- Grasping
- Minimizing damage
- Propagating through a cluttered environment
- Adapting to the shape of the food product

2.2.2. Grasping

A lot of different gripper types exist. To give a clear overview of these grippers, the grippers are divided into different categories, based on the grasping location of the gripper.
The following categories are made. [32]
Grasping is handled at:

- top surface (I)
- side surface (II)
- bottom surface (III)
- top and side surfaces (IV)
- side and bottom surfaces (V)
- top, side and bottom surfaces (VI)

These categories are visualized in Figure 2.2 where the red lines show the contact area between the object and the gripper.
For grasping an object two main divisions are made. Grasping can be done by either force-closed design, which means that the resulting force of the reaction forces on the object is in the direction in which the object is sturdy locked. These types are for example grippers that use a vacuum/sucking technique or a two-finger pinching gripper. The other main division is form-closed design. This means that the object is closed off with the gripper in such a way that it is geometrically impossible to leave

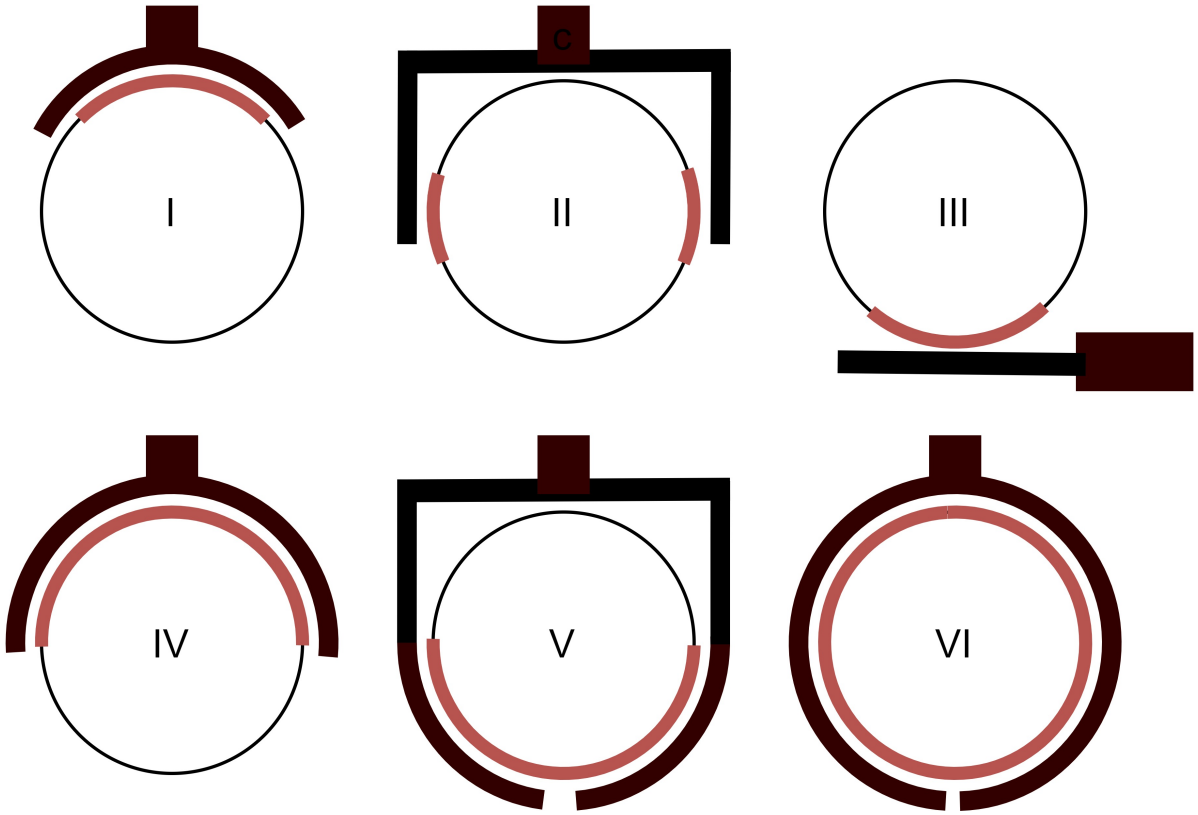

Figure 2.2: Six main gripper categories: I, II, III and IV are force-closed grippers and V and VI are form-closed grippers.

the gripper while moving the robot arm.
Grippers in categories I, II, III, and IV, as stated in Figure 2.2 are based on force-closed design. Grippers in categories V and VI are based on form-closed design.

Force-closed grippers

There are several grippers that use the top surface of an object as a grasping location. There are grippers that are based on using airflow to create a vacuum in which the object gets sucked towards the surface of the gripper. Examples of these grippers are suction cups, grippers based on Bernoulli's Principle [31], and grippers based on the Coanda effect [8]. Other top surface grippers are based on using adhesion principles. Examples of these grippers are grippers based on adhesion by using rollers, for example, a pasta roller [7], or grippers that use the adhesion principle with certain types of fluids, like a capillary gripper [10]. Furthermore, a type of gripper that is less popular in the agri-food industry is the needle gripper, which is a gripper with a lot of small needles that penetrate the surface of an object to grasp the product. However, it damages the food, which makes it often not suitable for application in the field of this research [17].
Side surface grippers are a common type of gripper. It is based on clamping the object on between two or more fingers with a high enough force such that the friction force on the sides of the object is high enough to resist the weight of the object.
A lot of these types of grippers exist, but interestingly for application in the agri-food industry are the soft type grippers, such as the SoftGrippers [2] that are specially designed for food handling or the Festo Multichoice gripper [19] that also adapts to fragile food products.
A gripper that uses solely the bottom surface of an object is very uncommon, as it is often not a stable way to grasp an object. However, there are a few grippers made that make use of only the bottom surface of an object. An example of this type of gripper is a spatula-like gripper that is used for grasping soft, viscous fluids like sauces [27]. When top and side surfaces are the grasping location often a combination of different gripper principles are found e.g. a combination of suction cups and grasping fingers. Also forming around the surface can be found in the form of adhesion principles.

Form-closed grippers

As in the agri-food sector the products are often very deformable, slippery, and fragile it is valuable to have an insight into the form-closed grippers. These grippers will have no problems with friction issues, when a slippery product has to be grasped, and it adapts to the shapes of the products.
A certain type of gripper that has gripping fingers to grasp objects to their side, but also has base support is a spatula gripper. For instance, the quad-spatula gripper has four grasping fingers with base plates that interlock when the fingers close.
Grippers that are fully enclosed are counted in this category. Not many of these types of grippers yet exist. A few examples are the meat gripper of Applied Robotics [25] and grippers that use a combination of the above-described gripper types, like a combination of using the Bernoulli principle and fingers.

Conclusion

What can be concluded from the research about the main categories of grippers is that for the application of the agri-food industry, where products are fragile, deformable, and often slippery, the preference goes to a form-closed design for the gripper, as that has no exceeding forces on the surface of the food product, is enclosing the object and is therefore not dependent on the surface roughness and shape. Furthermore, what can be concluded is that most grippers use the principle of two or more fingers approaching the product with an opening and closing method. However, this is not feasible in a situation where the product is in a cluttered environment. Force-closed design also causes problems in situations where the product is, for instance, hanging in a plant in the greenhouse instead of laying on a rigid surface such as a table, as the product is then much more sensitive to disturbances, which can cause the gripper to push the product away instead of grasping it.

2.2.3. Minimizing damage

Damage to the food product can be minimized primarily by designing such that a zero or low force is applied to the object. The resulting force on an object can be split up into a force along the surface of the object, which are traction forces, and a force perpendicular to the surface of the object, which are the pinching forces.

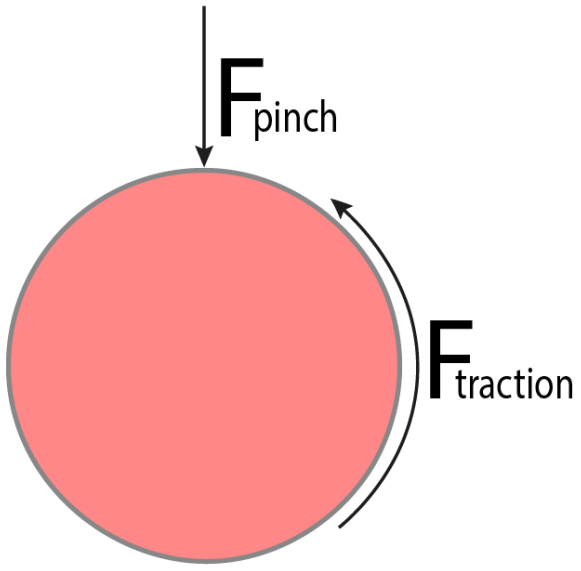

Figure 2.3: Visualisation of the pinching and traction forces on the surface of a tomato.

Low traction

One type of force is the traction on the surface of the object. This traction could cause rupture of the skin and therefore has an impact on the food quality. One method to reduce the traction on the surface is to make use of the principle of zero slip. This means that all the contact points of the mechanism concerning the food object are at the same location and thus no slip between the contacts and therefore no friction force.

This zero-slip can be created in different ways. One convenient type is to use eversion. Eversion can be found in different applications. There exist so-called vine-robots, that grow from the tip of an everting balloon-like tube. A specific type of vine-robot is one that is designed to explore coral reefs and therefore propagates through the ocean [16]. These vine-robots have therefore no relative motion between the exterior of the robot and the environment. There are already further developed types of vine robots that can be steered passively, like for example with knitted or taped stiff, but flexible patches [23], or in an active way, like for example when inflatable pouches are used [1]. Furthermore, based on lengths and curvatures of the path of the robot already types of modelling and control of these robots are developed [3].
These vine robots make good use of the eversion principle, but there are a few disadvantages of using these types of inflatable robots. First of all, a fluid or pressure has to build up to make sure that the stiffness of the fingers is high enough to grasp an object. Furthermore, these types of robots are hard to control. Therefore, it would be interesting to investigate if there are other ways to implement this eversion principle.
One way would be to use a stiff preformed backbone with rollers [12] that guide a belt as can be seen in Figure 2.4.

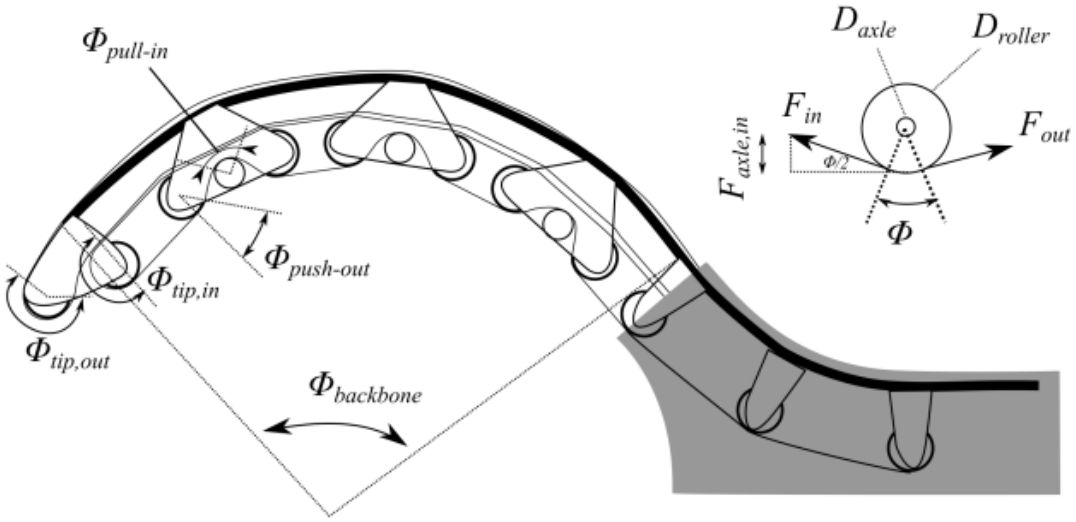

Figure 2.4: A design of a mechanical eversion mechanism with rollers [12].

Low pinching force

Pinching forces are caused by the actuating force of the actuator of the gripper. When these actuation forces are high and the tip surface of the gripper finger is small this causes high stresses on the surface of the approached food product. The main solution to minimize these stresses and therefore the pinching force on the surface of the food object is to adjust the fingertip. When this fingertip is rounded, the stress is distributed over a greater surface. Another way the pinching forces can be minimized is to use softer materials at the tip of the finger.

2.2.4. Shape adaptive possibilities

To adapt to the shape and encountered environment it is also possible to use steering of the grasping fingers. This can be done actively or passively.

Active steering

Active steering can be done by using a combination of multiple elongation methods. It is possible, for instance, to use a silicon tube with patches of a certain textile or material with a certain structure and stiffness that can then be configured in axial elongation and bending. A common way to change the behavior of elongation and bending is to use a rubber body, a strain limiting layer, and a combination of helical coils in either clockwise or counter-clockwise direction around the rubber body [22]. The types of fingers that can be made in this way are shown in Figure 2.5 This concept of making use of a

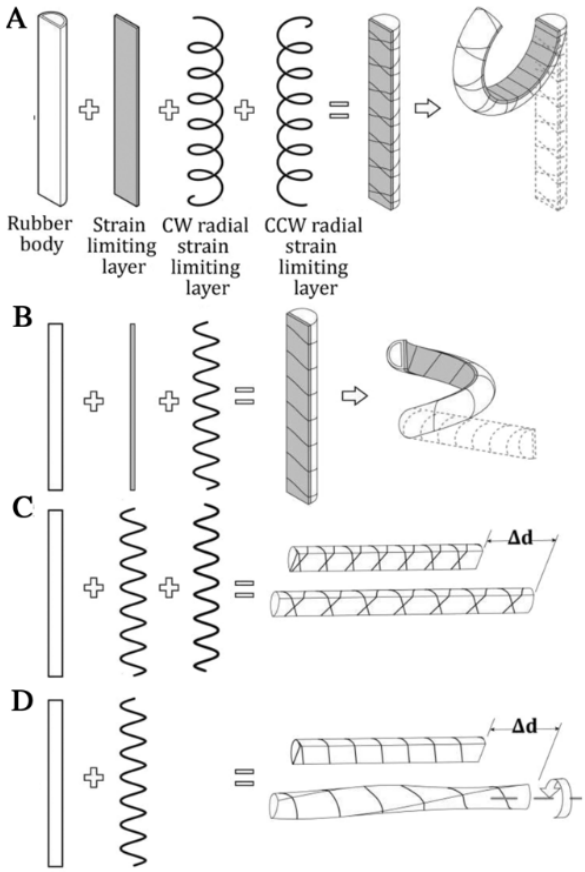

Figure 2.5: Different types of bending and elongating fingers of a compliant glove [22].

combination of stiffness in certain directions is a convenient way to create bending shapes. This can also be done with the help of crimp-braided sleeves [9] or making use of ZPR (Zero Poisson Ratio) or NPR (Negative Poisson Ratio) textiles [33] or auxetic textiles [28], which are textiles that behave different in mechanics, as the Poisson Ratio is not positive, as is and therefore the stress is distributed in the direction of tension and the stiffness is also adjusted in certain directions. These textiles can be attached to compliant materials to guide the gripper fingers in the desired direction and path. A concept similar to the crimp-braided sleeves is the clothing that is made by Omniskins [4], which uses robotic skins, driven in a pneumatic way or by the use of SMA (Shape Memory Alloy), that therefore influence the stiffness in certain directions. Another way of steering the gripper fingers is by using the concept where one side of a structure is made shorter or longer than the other side of the structure. In this way, this difference in length gives room for bending. This change of length can be caused by for instance making use of so-called pneumatic muscles, also known as McKibben muscles [13], which are mechanical versions of human muscles, in which the balloon with fibers around it shortens when the balloon is pressurized with either air or another fluid [21]. Another way this could also be done is by using electroactive polymers [20]. These are polymers that change in stiffness when an electromagnetic field is applied. In this way, the length and stiffness of a gripper finger can be actively changed in which the finger can be steered in a certain direction.

Passive steering

When it comes to passive steering this means that the finger automatically adapts to the shape of the object that it encounters. Within the field of compliant mechanisms, there are several versions of mechanisms that adapt to the object. One concept is the underactuated gripper finger. An underactuated gripper is such a way that the fingers close when certain parts, e.g. the phalanges of the finger, are touching an object. The phalanges are connected in such a manner that they behave on the forces on one, or multiple, of these phalanges. These underactuated grippers can be found in either rigid mechanisms with for instance cables and springs, but also in the version of compliant mechanisms.

Examples of rigid underactuated mechanisms [24] are tendon-actuated mechanisms, which use a cable transmission, linkage mechanisms, differential mechanisms, or a hybrid version. These types are shown in Figure 2.6.

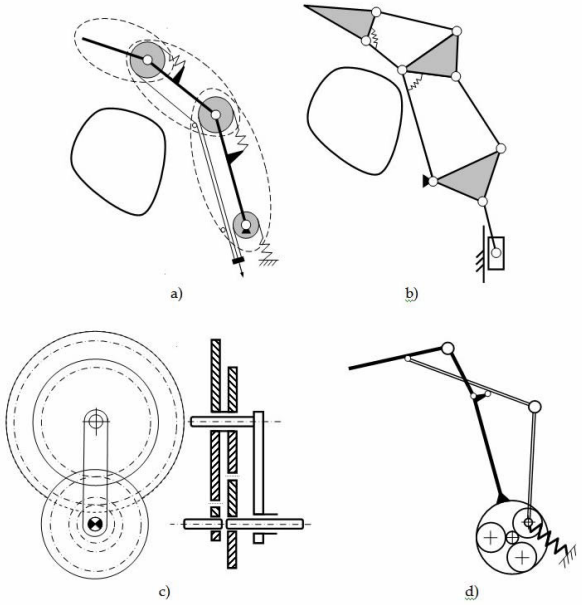

Figure 2.6: Types of (rigid) underactuated mechanisms: a) tendon-actuated, b) linkage mechanisms, c) differential mechanisms, d) hybrid mechanisms.

A compliant version of these underactuated mechanisms also exists. A bistable version [18] of these types of mechanisms can be found in Figure 2.7.

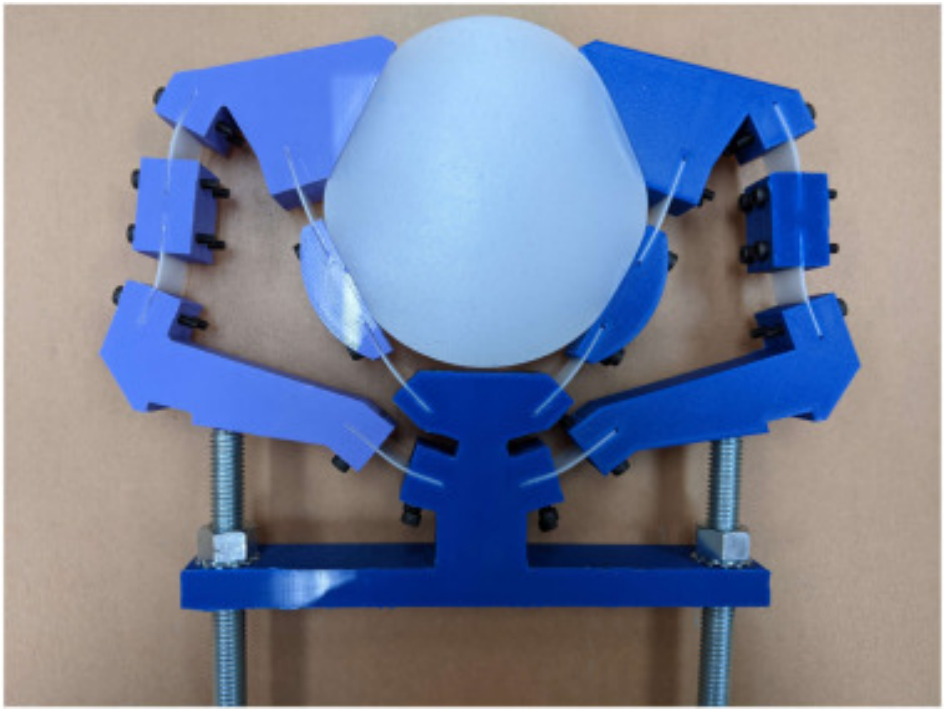

Figure 2.7: An example of a compliant bi-stable underactuated mechanism.

2.2.5. Propagating in a cluttered environment

To be able to propagate in a cluttered environment it is necessary to have a design that can get through small gaps. Also, the flexibility of the structure should be such that it can adapt to the available gaps. These gaps are not always the same and therefore a flexible or compliant design would be a good option for fulfilling this functional requirement.
To get a thinner design it is useful to look at the material properties, but also the single components of the finger. When components, such as rollers, can be removed this would have a great influence on the thickness of the finger.

2.2.6. Further relevant literature

Materials

For different applications, different materials are required. In the process of researching the possibilities of a sleeve design, different materials were tested to get an idea of how materials behave when a finger-like structure is pushed through it.
The important material properties that depend on the performance of a sleeve are:

- Stretchability (axial stiffness)
- Bending stiffness
- Waterproofness
- Friction coefficient

Different textiles are available. Types of textiles that are used in the industry and are possibly suitable for the production of a sleeve are:

- Stocking
- Outdoor-textile (80% PES, 20% PE)
- Lycra
- Latex
- Fish-gripping material (used by MAREL [26])
- Neoprene
- Leather
- Satin
- Rubber

These materials were tested by hand to make observations. The main categories that were observed were stretchability, and therefore axial stiffness, bending stiffness, and waterproofness, as the material should be washable, due to the hygienic environment and friction coefficient, as the sleeve will have a moving finger inside it, which should not be blocked due to high friction. The observations can be found in Table 2.1.

2.3. Literature Synthesis

2.3.1. Concept design

In the process of researching the literature to find answers to the research question, multiple insights, and ideas were found. In this section the three main concepts that seem the most promising are described.

Concept 1: Sleeve

The first idea that came to mind to improve the eversion finger as already designed and described in Figure 2.2.3 and shown in Figure 2.4 is to get rid of the rollers as these rollers are the parts that foremost determine the thickness of the finger and therefore have a low performance on the 'cluttered environment'-criteria and causes higher pinching force on the objects when they are situated in such cluttered environment.
However, when the rollers are taken away from the design the belt that functions as the eversion

Table 2.1: An evaluation of the performance of the studied materials for the sleeve design.

	Stretchability	**Bending stiffness**	**Waterproofness (washable)**	**Friction coefficient**
Stocking	High	Low	Not good	Low
Fish-gripping material	Low	Relatively high	Good	Medium
Outdoor-textile	Low	Low	Good	Low
Lycra	Relatively high	Low	Not good	Low
Latex	High	Low	Good	High
Neoprene	Medium	Medium	Good	Medium
Leather	Low	Medium	Medium	Relatively high
Satin	Low	Low	Relatively good	Low
Rubber	Relatively high	Low	Good	High

mechanism between the gripper and the object will not have any guidance anymore. A solution for a new type of eversion concept is to implement a closed 3D sleeve around a backbone. The backbone pushes through the sleeve and in that way, the sleeve has no relative movement between the sleeve surface and the food object, but only between the inside surface of the sleeve and the backbone of the finger. A schematic view of the working principle of the sleeve concept is shown in Figure 2.8

However, this concept also has challenges. These challenges were found when the concept was

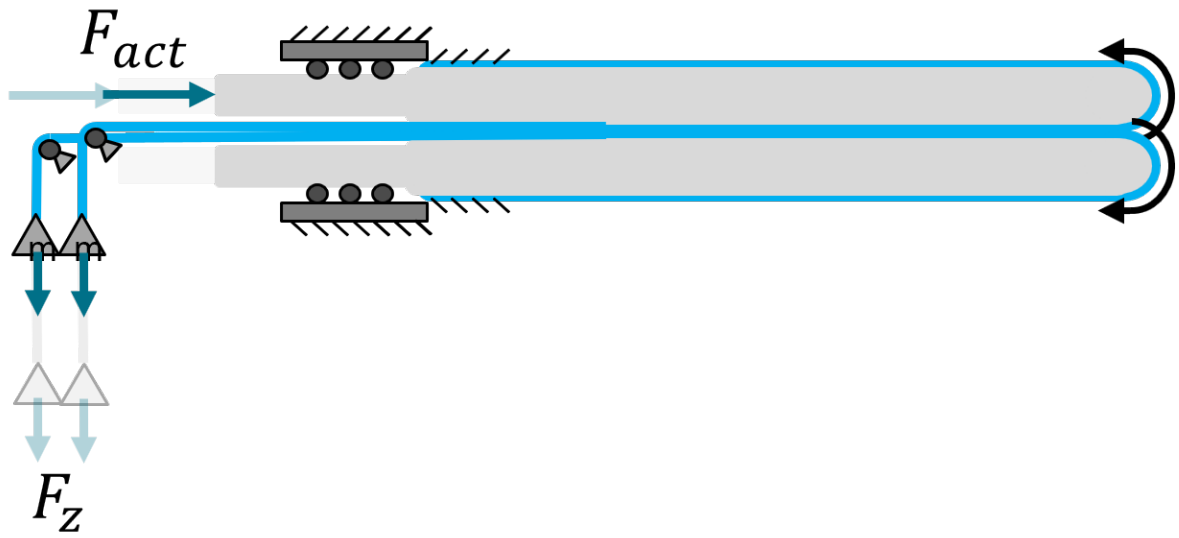

Figure 2.8: Illustration of the sleeve concept: the blue line depicts the sleeve that has tension due to a weight F_z. The grey solid represents the backbone that moves through the sleeve due to an actuation force F_{act}.

prototyped and unforeseen problems occurred. Because the sleeve has a closed shape and this shape changes when the finger changes from a straight to bending shape, the outer surface w.r.t. the product has to travel a longer distance than the inner surface, which causes strain in the material. This can not be completely solved by using stretchable sides as shown in Figure 2.9.

What was visible when making the prototype was that the sleeve would not evert in a good way, mostly caused by this displacement error, but also due to the stiffness of the sleeve material. Therefore, multiple materials were tested based on the stiffness. This test is already described in subsection 2.2.6 and the results of these tests can be found in Table 2.1. Besides this test, also tests were done to find the coherence between the radius of the fingertip of the backbone and the stiffness, e.g. stretchability,

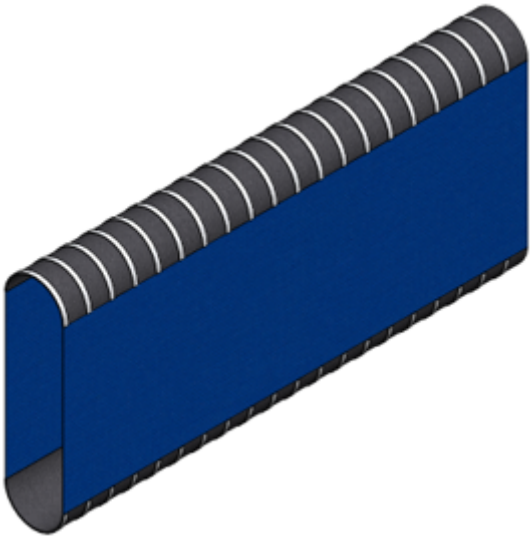

Figure 2.9: Illustration of a concept for a sleeve with stretchable sides.

of the sleeve material. An observation was made that for a small radius the stretchable materials often would not evert well over the backbone, but the backbone would have the preference to pinch through the sleeve. For the eversion around the fingertip therefore a material with high axial stiffness would be a good option. However, when it comes to these materials, often the bending stiffness is also higher, which makes it harder to follow the trajectory of the backbone and causes bulky movement of the sleeve, which later causes jamming of the sleeve. Another observation was that when a stretchable material is used instead of an axial stiff material, the sleeve would, besides everting, also stretch along the way due to friction on the inside. This means that the relative motion between the sleeve and the food object is not zero and therefore zero-slip is not fulfilled. The challenge in the design of the sleeve is therefore the material choice. An optimum has to be found between the bending stiffness and the axial stiffness.

Concept 2: Push

The sleeve concept gave challenges when combining an everting sleeve structure with a moving solid backbone. This gave inspiration to a new concept, the pushing concept. This concept is based on the idea of completely abandoning the combination of a sliding belt or sleeve with a backbone. In this concept, the whole finger is made of one part that is pushed forward and therefore rolls over the surface of the object. Different ways to propagate exist, which are based on the steering methods as already discussed in subsection 2.2.4. For instance, propagating forward with air or with electroactive polymers would be an effective way. However, air pressure makes it harder to control the fingers and the electroactive polymers are not responding quickly to the addition of an electromagnetic field, which would make the gripper slow. Therefore, this concept is based on actuation from the base with a motor and a pully over which the finger is enrolled. A visualization of this concept is shown in Figure 2.10. The challenge of this concept is again the material choice. Due to the removal of the backbone, the stiffness also disappears. A first small prototype was made with textile-like materials like neoprene, which has still axial stiffness, and a small bending radius, but also the flexibility to adapt to the shape of the object. A stiff and still flexible material could be found, like for instance a leaf spring. This seemed a first good option to make a small prototype of. However, when trying out the leaf spring as a grasping finger it was discovered that the bending radius of leaf springs becomes high, which means that in that way the finger would still be big at the fingertip and therefore would not be an improvement of the original mechanical design of the eversion finger concept. A balance between the buckling problem of non-stiff materials and the bending radius of stiff materials has to be found, which is the main challenge in this design.

Concept 3: Pull

From the challenge of the buckling, a new concept was formulated. This pulling concept is based on the caterpillars which have a belt and a pulley that causes forward motion. Using this concept of

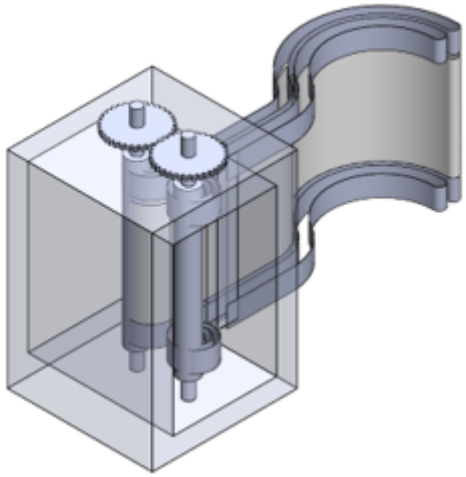

Figure 2.10: Illustration of the pushing concept.

the caterpillar in a grasping finger means that the eversion mechanism and the propagating force are caused by the same actuator at the same position, which is in the front instead of the back of the finger. This means that the finger is not pushed, which is sensitive for buckling, but is pulled and therefore is continuously finding the path through the cluttered environment. However, the backbone needs to be re-introduced for this concept to keep the belt in tension and to have a mounting place for the motor. The improvement with respect to the original eversion finger design is that this concept is not sensitive to buckling and still can be relatively small, as small motors with a diameter below 5 mm, which is the current tip radius of one side of the eversion concept, exist. A schematic drawing of this concept can be found in Figure 2.11.

Figure 2.11: Illustration of the pulling concept, where at the tip small motors provide the actuation of the finger.

Furthermore, in this concept, the rollers that are used in the original eversion concept are not present, which means that the belt is not guided and will hang loose, as shown in Figure 2.12. However, while

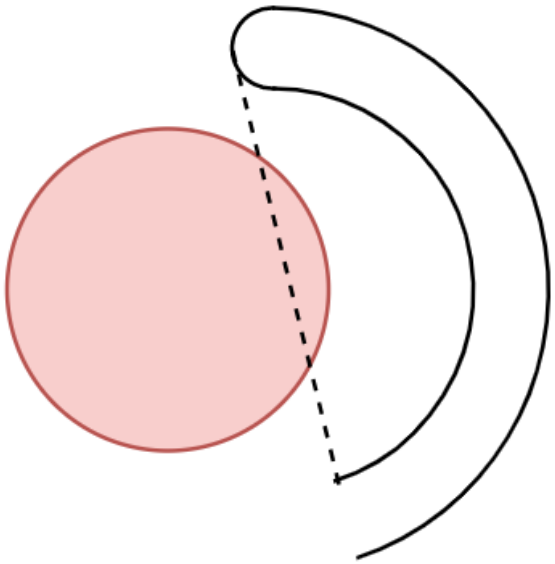

Figure 2.12: An illustration of the possible challenge of concept that has no guidance of the belt, where the belt is hanging loose, depicted by the dashed line.

generating this concept a new question was asked if it even was necessary to guide the belt along the curved surface of the finger if the belt is rolled out over the surface of the food object from the tip of the finger. Therefore, a small prototype is made of a pulling mechanism without guidance to test the necessity of the guidance. This prototype can be found in Figure 2.13. However, as this is not part of the literature review this will be further elaborated in the detailed design phase. However, to improve

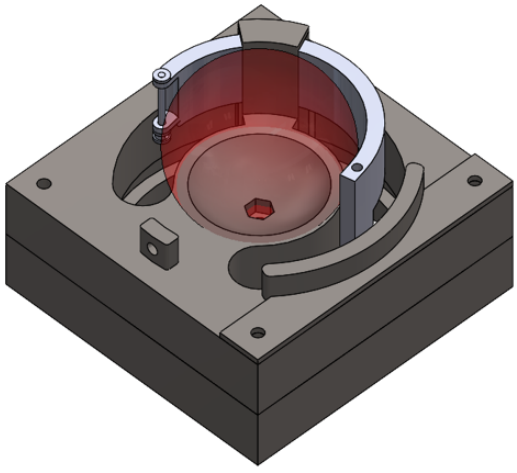

Figure 2.13: An illustration of the designed prototype for testing the necessity of guidance, where a curved finger rotates with an everting belt around a spherical object.

the thickness of the overall finger either a smaller motor needs to be found or a hybrid concept has to be found. A possible hybrid concept could be a concept between the pulling concept and the pushing concept, where the inner finger, which makes contact with the object, is only a single component finger as described in the pushing concept and the outer finger which makes contact with the environment and has to determine the S-shape of the finger can be made of the pulling concept. A schematic drawing of a possible hybrid concept is shown in Figure 2.14.

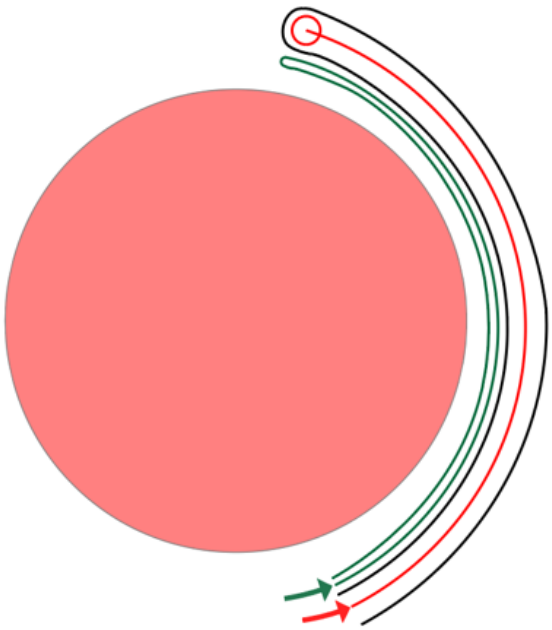

Figure 2.14: An illustration of the hybrid concept. The green part is the inner thin finger, made of a single component that everts inside the curvature of the outer finger, based on the pushing concept. The outer finger, depicted in red, is based on the pulling concept, where a motor actuates a curved finger with a backbone.

2.3.2. Performance metrics

To get insight into how well a concept would perform it is necessary to set performance metrics. These performance metrics will also be used when the model is validated and a conclusion can be drawn about the performance of the final design. The performance metrics that will be used in the concept choice are:

- **Complexity**: The concept has to be able to be built, modelled, and tested in approximately half a year, which is the duration of the rest of the graduation project. Therefore, the concept should not be overly complex.
- **Robustness against misalignments**: The concept should be able to deal with certain inaccuracies of the robot. These are inaccuracies in the XY-plane which is the plane perpendicular to the propagating direction of the finger and in the Z-plane, which is in line with the propagating direction.
- **Volume occupation**: The concept should not occupy too much volume. This is split into occupation at the fingertip, which has to propagate through the cluttered environment, and occupation at the robot mount. Here the volume occupation at the fingertip is more important because it influences the ability to propagate well through the cluttered environment. An added category to the volume occupation metric is that it should fulfill the grasping force limit, which means that the structure that changes through minimizing volume should still have enough stiffness to be able to grasp the food products robustly.
- **Damage minimization**: The concept should minimize the excited forces on the object and the forces on the environment. These forces are split up into traction forces and pinching forces.

A first evaluation of the three concepts is done with the help of these performance metrics. Later in the process, when after rapid prototyping more knowledge is gained about the concepts, these concepts will be weighed in detail with the help of the performance metrics in a MCA, multi-criteria analysis. The first evaluation can be found in Table 2.2.

Table 2.2: Elaborate evaluation of the performance of the three main concepts. The first column represents the weighing criteria. The other columns represent the performance evaluation for the three main concepts.

	Sleeve design	**Pushing design**	**Pulling design**
Complexity	Relatively high, due to textile mechanics.	Medium, easy to produce, but hard to find suitable material.	Medium, relatively easy to produce, but hard to find small enough motors.
Robustness against misalignments	Robust, due to flexible shape.	Predetermined path, so small errors possible.	Robust, due to flexible shape.
Volume occupation	Relatively high, due to required thickness in order to evert sleeve instead of pinching.	Low volume occupation, due to single part design.	Medium, small motors exist (D <5 mm). Still no great improvement w.r.t. original eversion design.
Grasping performance	With backbone able to fulfill grasping force limit	Hard to find suitable material that fulfills bending radius and axial stiffness in order to fulfill grasping force limit.	Able to fulfill grasping force limit.
Damage reduction	Good. When a sufficient material is found, the concept has zero-slip and a small backbone.	Still sides of the finger exposed to environment, which could cause some minor damage. Zero-slip is provided. Small tip, so small pinching force.	Still sides of the finger exposed to environment, which could cause some minor damage. Zero-slip is provided.

2.4. Discussion

In the process of doing literature research, a circular path is followed, which means that not always a well-structured way of research has been used. Often the focus of the research was changed and therefore a different function was used to find suitable solutions and concepts. This means that some concepts fulfill certain functions better with respect to the originally found eversion finger, but also not in all aspects. The sleeve design improves on thickness and damage but increases in complexity. The pushing design improves on thickness and pinching damage, but makes it hard to find suitable materials to build it from. The pulling design improves buckling but does not necessarily become thinner than the original design.

Another point of discussion is that this research topic is quite new and therefore there is not much literature available about similar eversion type, compliant mechanisms that have a propagating behavior instead of opening/closing behavior. This means that besides the small available literature, a lot of small tests had to be done to gain knowledge about the behavior of certain backbones, concepts, sleeves, and materials. This is not always done in a thorough research setup, but often with simple tests. This is not a well-founded base, but gave easy and fast insights.

2.5. Conclusion

The main question of this literature study was:

*What are the **challenges** in designing a **compliant zero-slip gripper** for the agri-food sector that propagates through a **cluttered environment**?*

In the research, a lot of different challenges were encountered, like the effect of material properties on the performance. These material properties are the bending stiffness and axial stiffness of thin, flexible materials. In this challenge, an optimum has to be found.

Another challenge that was found was the ability to move through a cluttered environment without damaging the environment, which could be minimized by using the eversion principle and soft materials, but also not getting too soft to prevent buckling from happening.

These challenges are tackled in three main concepts, that have the functions of the finger embodied and all have benefits and disadvantages. A hybrid concept could be a solution but is yet to be determined in a structured way with the help of a multi-criteria analysis that is based on performance metrics.

3

Research Gap

In academic research, the unexplored or underexplored area of an existing body of knowledge on a topic is often called a research gap. For a good foundation of the research, it is essential to identify the gap and have a good understanding of the missing knowledge, as this missing knowledge defines the scope and purpose of the stud

The research gap is often found by reviewing existing literature to gain insight into the state of the art, the challenges of a topic, and the scope in which development and advancement on a certain topic is facilitated. When a research gap is found this gap helps by formulating the research question of the main project that will have a contribution to the academic field.

In this chapter a recap is given about the main challenges that were found from the literature study and the main focus of the project is given such that the found gap in existing research can be further closed. With this focus, a research question will be formulated.

3.1. Design challenges

From the literature review of certain types of compliant grippers, as can be read in chapter 2, challenges were found when an encompassing gripper has to be designed. In the formulation of the three concepts, different design parameters have different influences on the performance metrics. In the case of an encompassing compliant gripper with a sleeve for friction reduction, as described in the literature review, the parameters that greatly influence the performance of the functionality of the gripper are the enclosing angle and the thickness of the gripper finger. The enclosing angle affects the performance of the sleeve, as the sleeve mechanics cause tension problems when the enclosing angle becomes bigger. The thickness influences the overall performance of the gripper, as the pinching forces on the environment become lower and the ability to propagate through cluttered environments becomes higher when the thickness of the finger is reduced.

3.2. Project focus

In the previous section, the challenges in designing a compliant encompassing gripper are described and it is concluded that the thickness and enclosing angle are the main parameters of interest. Therefore it is necessary to gain knowledge about the relation of these design parameters in the context of a defined load case, such that academic design choices can be made. This is done by determining the pull-out force for a gripper with defined design parameters, such that certain designs can be evaluated based on the maximum payload.

The research question, therefore, is formulated as:

*How can in a structured way knowledge be gained about the **relation** between important design parameters, such as **thickness** and **enclosing angle**, for a certain case study, with the help of a **model-based approach**?*

To answer this question a model has to be built that simulates a curved compliant gripper finger out of which a circular object, such as a tomato, is pulled out in order to find the maximum pull-out force for an object with certain properties and for a gripper finger with certain defined design parameters, which are the geometrical parameters, such as thickness, width and enclosing angles, as well as material properties. When this model is developed, the model should be validated such that the accuracy of the model is known. By this validation then a reliable model can be presented, that will give results that can safely be used in the actual design. The validated model then can be used in a parametric study, such that design charts of different parameters can be made for certain case studies.

4

Methodology

In this chapter, the methodology of the project is described. This contains a detailed explanation of the modelling method that is used to reach the design goal. This modelling method is called Pseudo-Rigid Body Modelling (PRBM). By implementing and extending an existing PRBM model, the model is translated into a usable form that has an application in the field of gripper design. The kinematics are solved by introducing a vector loop that is solved by an optimization algorithm. With the results of the optimization, the kinematics are determined, in which the pull-out force is the most important result.

4.1. Pseudo-Rigid Body Modelling (PRBM)

A commonly used modelling method in the design of compliant mechanisms is Pseudo-Rigid Body Modelling (PRBM). PRBM is a method where a compliant mechanism is approximated as a rigid mechanism. This approximation is done by making use of 'pseudo' rigid beams, which are beams with a certain length, that have a smaller length than the actual length of the mechanism. Besides the beams, the compliance of the compliant mechanism is emulated by adding torsion strings at the joints of the pseudo-rigid beams.

4.1.1. Advantages of PRBM

There are multiple advantages of using PRBM as a modelling method in the design of compliant mechanisms.
Firstly, due to the approximation of the compliant mechanism as a multi-rigid body mechanism, the model approximates the deformations and displacements of the mechanism accurately up to high deformations, whereas simple Euler-Bernoulli beam equations are only valid for small deformations. This makes the PRBM method suitable for the nonlinear behavior of compliant links.

Another advantage of the PRBM method is that it is fully parametric based and therefore suitable for gaining knowledge about parametric relations which is in line with the goal of this research. These base PRBM parameters are often determined experimental or by detailed analytical modelling. Therefore, the computational load of a parametric study for a PRBM, compared to for instance FEM-modelling is much lower and therefore easier to use in a design setting. This gives room to making fast parametric or geometrical changes and iterating fast through different design cases, which gives fast and easy insight into determining a good design plan and is very suitable for rapid prototyping.

Furthermore, due to its parametric nature, it is much easier to implement it in optimization algorithms, than for instance FEM. The optimization algorithm would be much more computationally efficient with PRBM. Therefore, by using PRBM the optimal design of a compliant gripper is possible in an efficient way.

4.1.2. The 3R PRB model for initially curved beams

Existing PRB models [6, 30], where large deformations for different types of beams are described, such as initially curved beams [29, 15], offer a suitable foundation for extension into a model applicable to

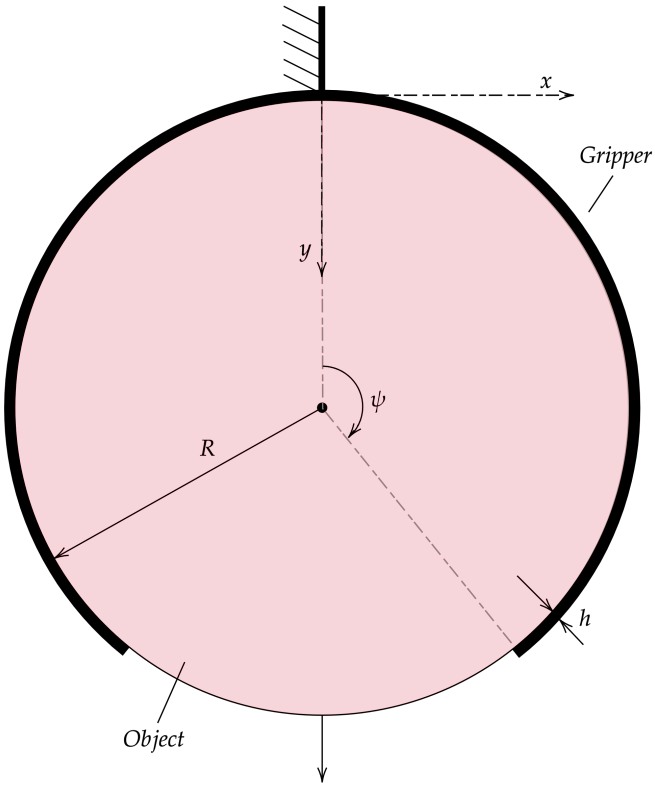

Figure 4.1: Problem definition: a gripper with two initially-curved fingers with thickness h and enclosing angle ψ out of which a circular object with radius R is extracted.

gripper design. In an existing PRB model [29] where an initially curved compliant beam is modelled already exists. In this model, the initially curved compliant beam is split up into four segments with three joints. This results in a three DoF mechanism, which therefore can be mapped to a square Jacobian from the joint space to the actuation space. The setup of this model is chosen to be the base of the model in this project that will be extended such that it facilitates the parametric study for compliant gripper design.

The case study of the model as shown in Figure 4.1 consists of a circular object with a radius R and a gripper with two initially curved fingers that have an enclosing angle ψ and thickness h. The arc length L of the initially curved finger is equal to $L = \psi R$.

The PRB base of the model is defined with the following parameters:

- Four segments with length l_i, where $l_i = \gamma_i L$, for i = 1, 2, 3, 4
- Three pivot joints with torsion springs of $K_{\theta i}$, for i = 2, 3, 4
- Initial relative angles ζ_i, where i = 1, 2, 3, 4
- Deformation angles $\delta\theta_i$, where i = 2, 3, 4
- Tip force F

The initial angle of the first link ζ_1 is defined relative to the x-axis. The initial angle of the remaining three links is defined as the angle relative to the direction of the previous link. The schematic of the model definition can be found in Figure 4.2, where the undeformed and deformed states of the mechanism are illustrated.

As there are only torsion springs at the joints, there is no deformation of the first segment. This is considered because a cantilever support of the mechanism is assumed. Therefore, the deformation of

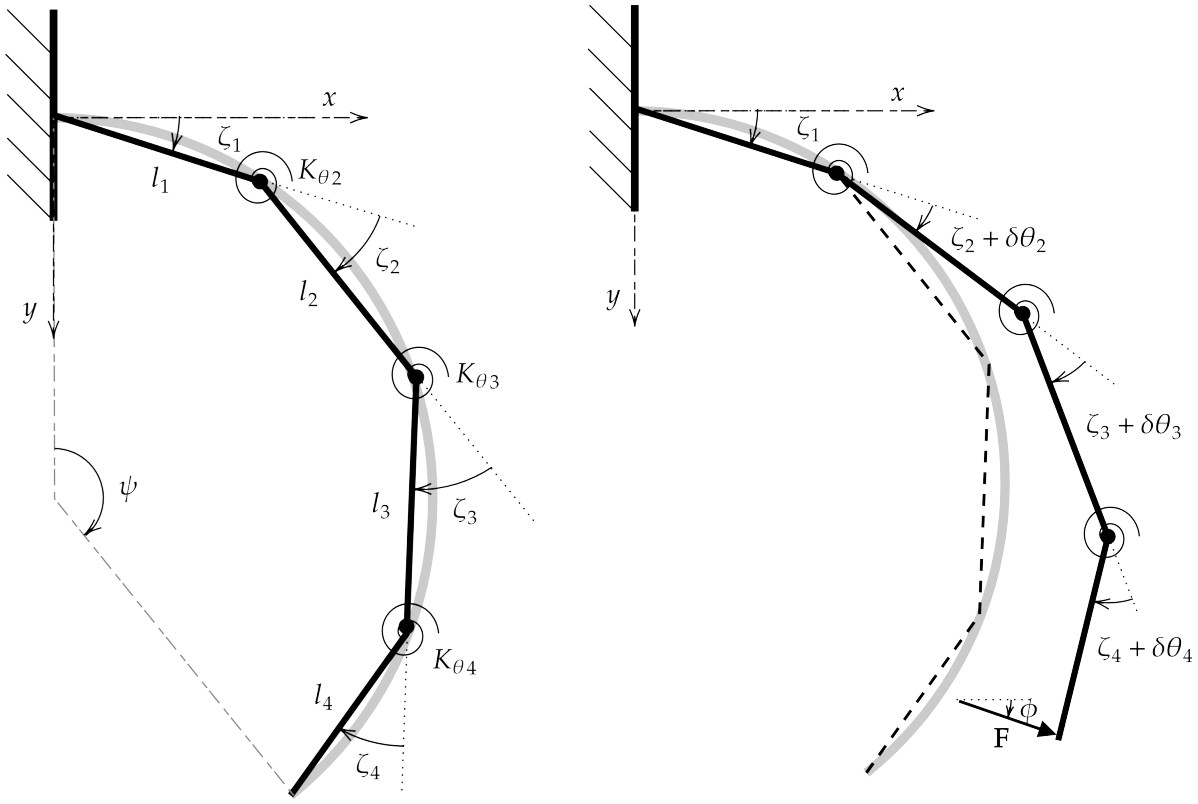

(a) Undeformed state **(b)** Deformed state

Figure 4.2: Model definition: a Pseudo-Rigid Body model with four linkages and three torsion springs at the joints, depicted in the undeformed and deformed state. When a force F is applied at the tip, the linkage deforms.

the first segment is so low compared to the other deformation that this is simplified to be a rigid support.

The stiffness of the torsion springs is determined by the relation as given in Equation 4.1. Here the constant $k_{\theta i}$ is the pseudo stiffness of each joint.

$$K_{\theta i} = k_{\theta i}\frac{EI}{L}, \quad i = 2, 3, 4 \tag{4.1}$$

In this equation, E is the Young's modulus, which is a material property that depicts the relation between tensile stress and tensile strain of a material and therefore gives information about how easily a material stretches under a certain load. The parameter I is the area moment of inertia, which gives information about how much resistance a shape (like the cross-section of a beam), has to bend because of its geometry. The cross-section of the finger has a rectangular shape with width w and height h and therefore the area moment of inertia is defined as depicted in Equation 4.2.

$$I = \frac{wh^3}{12} \tag{4.2}$$

The PRB parameters are therefore γ_i, ζ_i, and $k_{\theta i}$ as they are the constant values that approximate the kinematics of the real compliant mechanism. These PRB parameters are determined via an optimization by K. Venkiteswaran [29]. Here the values are determined for different geometrical configurations, where the enclosing angle, or the angle of curvature ψ changes with instances of 15 degrees. The optimized values can be found in Table 4.1.

A few assumptions were made.

Table 4.1: The PRB values of the 3R initially curved PRB model [29].

$\psi\ (deg)$	ζ_1	γ_1	$k_{\theta 2} = k_{\theta 4}$	$k_{\theta 3}$
0	0.0000	0.1337	3.1570	2.7389
15	0.0174	0.1329	3.1735	2.7132
30	0.0339	0.1294	3.2388	2.6210
45	0.0502	0.1277	3.2722	2.5769
60	0.0666	0.1271	3.2944	2.5491
75	0.0824	0.1257	3.3260	2.5117
90	0.0979	0.1244	3.3519	2.4830
105	0.1126	0.1226	3.3872	2.4456
120	0.1292	0.1230	3.3894	2.4432
135	0.1456	0.1231	3.3966	2.4352
150	0.1625	0.1235	3.3955	2.4349
165	0.1812	0.1251	3.3768	2.4528
180	0.2008	0.1269	3.3546	2.4764
195	0.2217	0.1292	3.3235	2.5106
210	0.2430	0.1313	3.2944	2.5439
225	0.2641	0.1329	3.2727	2.5706
240	0.2859	0.1346	3.2517	2.5973
255	0.3085	0.1364	3.2314	2.6233
270	0.3342	0.1392	3.2011	2.6629

First, the symmetry of the model is assumed, and therefore

$$\gamma_4 = \gamma_1, \quad \gamma_3 = \gamma_2, \quad \zeta_4 = \zeta_2 = \frac{\psi}{4}$$

and the joints are on the beam in the undeflected position, thus

$$\gamma_1 = \frac{2}{\psi}, \quad \gamma_2 = \frac{2}{\psi} \sin\left(\frac{\psi}{4} - \zeta_1\right), \quad \zeta_3 = \frac{\psi}{2} - 2\zeta_1$$

The angles of deformation are $\delta\theta_2$, $\delta\theta_3$ and $\delta\theta_4$, as depicted in the deformed configuration showed in Figure 4.2b. When all PRB parameters and deformation angles are known, the x- and y-coordinate can be calculated by respectively Equation 4.3 and Equation 4.4 and the exit angle of the tip can be calculated by Equation 4.5.

$$X_{tip} = L \sum_{j=1}^{4} cos\left(\sum_{i=1}^{j}(\zeta_i + \delta\theta_i)\right)\gamma_i \tag{4.3}$$

$$Y_{tip} = L \sum_{j=1}^{4} sin\left(\sum_{i=1}^{j}(\zeta_i + \delta\theta_i)\right)\gamma_i \tag{4.4}$$

$$\theta_{tip} = \psi + \delta\theta_2 + \delta\theta_3 + \delta\theta_4 \tag{4.5}$$

4.1.3. PRB implementation and extension

The existing model is suitable for finding the position of a compliant mechanism when a certain load at a certain direction is applied on the tip. However, in the case of an object being extracted from a mechanism, such as in a gripper configuration, the magnitude and direction of the force are unknown. Moreover, the direction of the force changes as the object descends through the fingers during the opening of the gripper, influenced by the load of the object.

To make the method applicable for this use case, a fifth link is pinned in series to the pseudo-linkage and a joint on a slider to simulate the motion of the object. The link has length l_5, which is equal to R, the radius of the object. The slider constrains the base of this added link, such that it only has one degree of freedom in the y-direction, the direction in which gravity would apply. This configuration allows the tip of the linkage to trace the circular path of the surface of the object and rotate freely at the contact point. The extended PRB mechanism is shown in Figure 4.3.

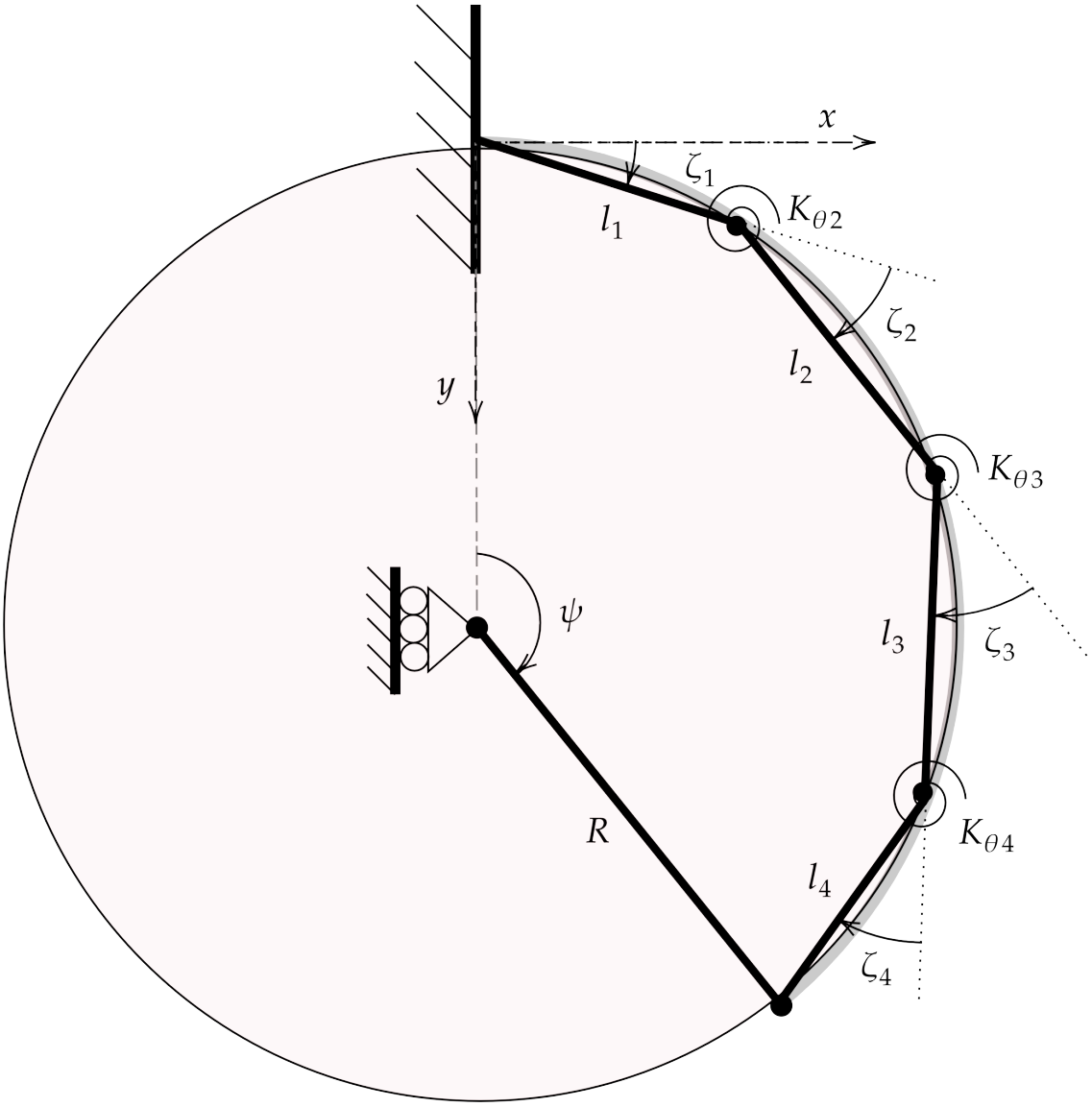

Figure 4.3: Model extension: adding a fifth link with radius R in series to the existing linkage to a joint on a slider to mimic the displacement of an object in the y-direction.

When the model is extended, the fifth link will move in the y-direction in small steps dy and for each iteration, the configuration of the mechanism can be calculated. The configuration of the mechanism can be calculated by minimizing the potential energy of the mechanism, caused by the torsion springs at the joints. The definition of the potential energy in the system that will be minimized is defined in Equation 4.6.

$$V = \frac{1}{2}K_{\theta 2}\delta\theta_2^2 + \frac{1}{2}K_{\theta 3}\delta\theta_3^2 + \frac{1}{2}K_{\theta 4}\delta\theta_4^2 \tag{4.6}$$

With the calculated configuration of the mechanism at each iteration then the load vector can be calculated and therefore the pull-out force, which is the force on the tip in the pull-out direction, the y-direction, can be determined and visualized. This maximum value of this pull-out force then can be linked to the maximum load a certain mechanism design can hold.

4.2. Kinematics

4.2.1. Vector loop

To solve the kinematics in the extended model the vector loop equations have to be set. The vector loop is defined from the base to the tip. The schematic of this vector loop is shown in Figure 4.4.

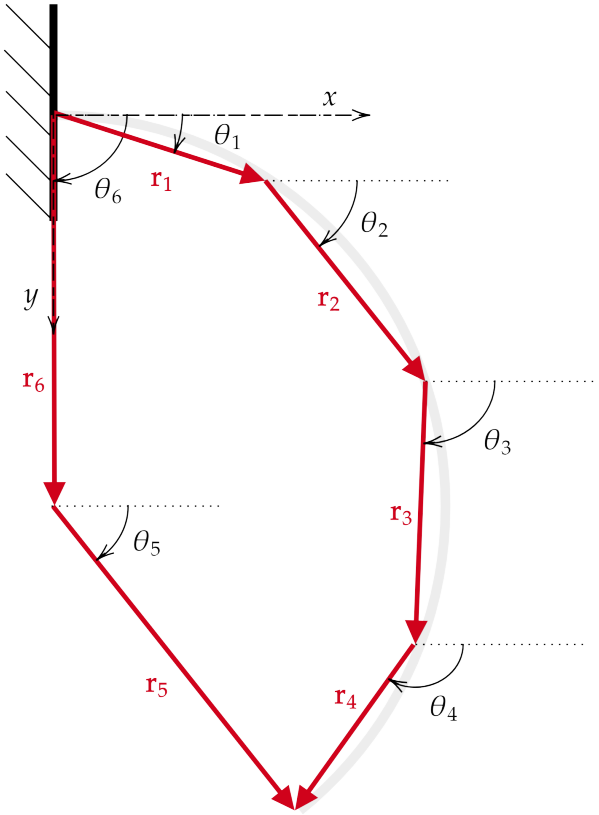

Figure 4.4: Vector loop: the vectors $\vec{r}_2$, $\vec{r}_3$ and $\vec{r}_4$ follow the paths and directions of the finger links. Vector $\vec{r}_5$ represents the object. Vector $\vec{r}_6$ represents the displacement of the object in the y-direction.

In this vector loop $\vec{r}_1$, $\vec{r}_2$, $\vec{r}_3$ and $\vec{r}_4$ are the vectors following the paths and directions of the finger links. Vector $\vec{r}_5$ is the vector following the path and direction of the center of the object to the contact point of the object to the fingertip. Vector $\vec{r}_6$ is the vector that depicts the displacement of the center of the object in the y-direction. By definition, the vector loop should be closed and therefore the relation between the six vectors is as shown in Equation 4.7.

$$\vec{r}_1 + \vec{r}_2 + \vec{r}_3 + \vec{r}_4 = \vec{r}_5 + \vec{r}_6 \tag{4.7}$$

When $\cos(\theta_i)$ and $\sin(\theta_i)$ are abbreviated to c_i and s_i, the vector loop equations can be rewritten as depicted in Equation 4.8.

$$\begin{cases} l_1c_1 + l_2c_2 + l_3c_3 + l_4c_4 - l_5c_5 - l_6c_6 = 0 \\ l_1s_1 + l_2s_2 + l_3s_3 + l_4s_4 - l_5s_5 - l_6s_6 = 0 \end{cases} \tag{4.8}$$

The lengths l_i and angles θ_i are defined as shown in Equation 4.9.

$$l = \begin{cases} l_1 = \gamma_1 L \\ l_2 = \gamma_2 L \\ l_3 = \gamma_3 L \\ l_4 = \gamma_4 L \\ l_5 = R \\ l_6 = R + y \end{cases} \qquad \theta = \begin{cases} \theta_1 = \zeta_1 \\ \theta_2 = \theta_1 + \zeta_2 + \delta\theta_2 \\ \theta_3 = \theta_2 + \zeta_3 + \delta\theta_3 \\ \theta_4 = \theta_3 + \zeta_4 + \delta\theta_4 \\ \theta_5 = \psi - \frac{\pi}{2} + \delta\theta_5 \\ \theta_6 = \frac{\pi}{2} \end{cases} \tag{4.9}$$

From these values the value l_6, θ_2, θ_3, θ_4 and θ_5 are unknown, as the length y, object angle θ_5 and the deformation angles $\delta\theta_2$, $\delta\theta_3$ and $\delta\theta_4$ are not known.
This results in five unknowns, while there are only two equations, which are the vector loop equations in Equation 4.8. To reduce the number of unknowns, the direction value y can be used as an input for the model with incremental steps Δy.
To solve the vector loop equations an optimization algorithm is implemented, where $\delta\theta_2$ and $\delta\theta_5$ are used as optimization variables when the potential of energy in the system is minimized. The potential energy of the system is described by Equation 4.6. At minimal energy, the value of the optimization variables $\delta\theta_2$ and $\delta\theta_5$ are known and they can therefore be used to determine the remaining angles, $\delta\theta_3$ and $\delta\theta_4$.

4.2.2. Optimization algorithm

Initialisation

The initial values for the algorithm first have to be calculated to have to correct input for the optimization algorithm. The initial values of vector $\vec{\boldsymbol{\delta\theta}}$, that will be used in the algorithm are the values contained in the third column of Table 4.2. The vector $\vec{\boldsymbol{x}}$ contains the optimization variables, which will have the initial values of $\delta\theta_2$ and $\delta\theta_5$ at the first iteration. The vector $\vec{\boldsymbol{\delta\theta_{34}}}$ contains the values of the angles of the mechanism that are solved in the algorithm besides the optimization variables.

Table 4.2: The initial values for the optimization algorithm, containing the initial deformation angles of the mechanism $\vec{\boldsymbol{\delta\theta}}$, the optimization variables $\vec{\boldsymbol{x}}$, and the to-be solved unknown deformation angles $\vec{\boldsymbol{\delta\theta_{34}}}$.

Vector	**Variables**	**Initial values**
$\vec{\boldsymbol{\delta\theta}}$	$[\delta\theta_1 \quad \delta\theta_2 \quad \delta\theta_3 \quad \delta\theta_4 \quad \delta\theta_5 \quad \delta\theta_6]$	$[0 \quad 0 \quad 0 \quad 0 \quad 0 \quad 0]$
$\vec{\boldsymbol{x}}$	$[\delta\theta_2 \quad \delta\theta_5]$	$[0 \quad 0]$
$\vec{\boldsymbol{\delta\theta_{34}}}$	$[\delta\theta_3 \quad \delta\theta_4]$	$[0 \quad 0]$

For the displacement of the base joint of the fifth link, the displacement vector y is initialized, which contains the starting y-coordinate y_s, the stepsize,Δy, and the end y-coordinate y_e, as shown in Equation 4.10. The step size can be adjusted to reach the preferred accuracy and computational time. The starting point y_s is equal to zero and lies in the center of the disk. The endpoint y_e is equal to $2R$ to simulate the full extraction of the object from the gripper. Based on this initialization, the final coordinates of the sixth link will be the displacement y added to the radius R of the object, defined as l_6 in Equation 4.9.

$$y = [y_s : \Delta y : y_e] = [0 : \Delta y : 2R] \tag{4.10}$$

The optimization variables are bounded by upper boundaries, u_b, and lower boundaries, l_b. These boundaries are required, such that when the potential energy in the system is minimized the correct mechanism configuration is found. When minimizing potential energy multiple local minima can be found, which results in multiple possible kinematic configurations. In this case, the same angles are found, but for a certain couple of links, the configuration is a mirrored version, which would not be a realistic solution, as this kinematic configuration would penetrate the surface of the object. By imposing a constrained range of solutions, the physically plausible configuration is forced. However, the constraints should not constrain the optimization variables so much that the kinematics are not realistic anymore. Therefore, by trial and error, the upper and lower bounds are found for this study. The constrained space in which the optimization variables can find solutions is much bigger than the results

and therefore the kinematics are not constrained, but only the correct configuration of the kinematics is forced. The definition of these boundaries is given in Equation 4.11. The boundaries evolve with each iteration by using the results of the previous iteration as a starting point. The constrained space has an upper and lower value of respectively 3 and -3 degrees for $\delta\theta_2$ and the constrained space for $\delta\theta_5$ has an upper and lower value of respectively 15 and -15 degrees. The constrained spaces have a scaling factor, $c = 1000 \cdot \Delta y$, such that the correct scaling happens, when a higher or lower value of Δy is used, and such that the relative size of the boundaries stays correct. This dynamic constraint mechanism enables a substantial solution space without compromising the realism of the kinematics.

$$\begin{bmatrix} l_b \\ u_b \end{bmatrix} = \vec{x} + c \begin{bmatrix} -3 & -15 \\ 3 & 15 \end{bmatrix} \tag{4.11}$$

Algorithm description

The optimization variables are iterated within the interior-point solving algorithm, *fmincon*, in MATLAB. The objective function is to find the minimal potential energy as given in Equation 4.6. For all instances of the optimization values the potential energy will be calculated and the values of the optimization variable that has minimal potential energy, within the set tolerances, will be the values of $\delta\theta_2$ and $\delta\theta_5$ that will be used in solving the vector loop equations, as given in Equation 4.8, to find the remaining unknown values, $\delta\theta_3$ and $\delta\theta_4$. The values of the optimization vector $\vec{x}$ and objective vector $\boldsymbol{\delta\vec{\theta}_{34}}$ will be updated with the solved values of $\delta\theta_2$, $\delta\theta_3$, $\delta\theta_4$ and $\delta\theta_5$. These values will be stored in a dataset, such that the change of configuration for each step Δy can be studied after the algorithm is completed. This process will be iterated for each displacement of the disk in the y-direction, with stepsize Δy.

4.3. Kinetics

The result of the optimization is the kinematic configuration for each displacement y, which is used to determine the kinetics of the mechanism. To determine the maximum pull-out force of the mechanism only the fourth segment of the PRB mechanism is required, which is the segment at which contact is made between the object and the finger. A free-body diagram of the fourth PRB segment is illustrated in Figure 4.5. In this diagram, moment T_4 is the moment caused by the deformation of the torsion spring at the joint between segment three and segment four of the PRB mechanism. For this FBD the location of that joint is given as position B, while the contact point between the object and the fingertip is given as position A. At the tip the object applies a contact force, that is in the same direction as the direction of the fifth segment from the center of the disk to the tip of the mechanism. Therefore, the relation for the angle ϕ that the force has on the fourth segment is as given in Equation 4.12, where also the relation of angle ϕ_2 is given, which is derived by pure geometrically applying trigonometry. The force at position B, where also the reaction moment is depicted, is the reaction force of the tip force. This force is, therefore, the same in magnitude, but opposite in direction.

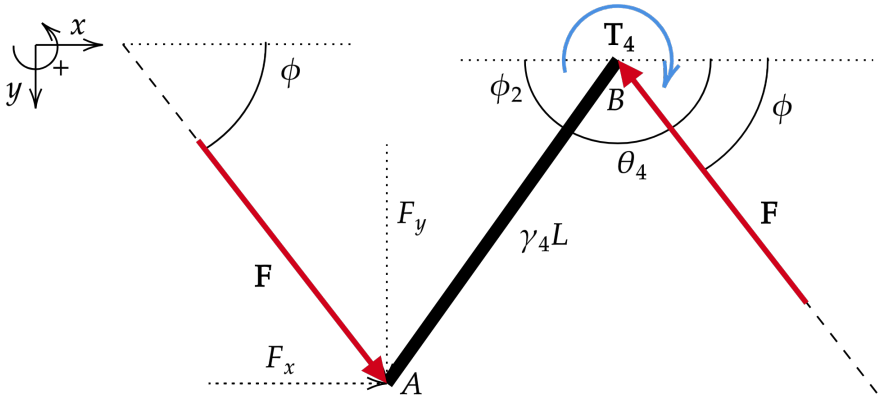

Figure 4.5: Free body diagram of the fourth PRB link: the force F at an angle ϕ, applied by the object on the fourth link of the PRB linkage, has an equal reaction force F at the joint between the third and fourth link. Furthermore, at this same joint, a reaction torque T_4, caused by the deformation of the torsion spring, is applied.

$$\begin{cases} \phi = \delta\theta_5 \\ \phi_2 = \pi - \delta\theta_4 \end{cases} \tag{4.12}$$

When static equilibrium is assumed there must be a force and moment balance, according to Newton's third law of motion. This results in the following static force balance, as depicted in Equation 4.13.

$$\begin{cases} \sum F_x = F\cos(\phi) - F\cos(\phi) = 0 \\ \sum F_y = F\sin(\phi) - F\sin(\phi) = 0 \end{cases} \tag{4.13}$$

To simplify the moment balance equation, the relation as shown in Equation 4.14 is defined, where F_x and F_y are the x- and y-components of the tip force F.

$$\frac{F_y}{F_x} = \tan(\phi) = n \tag{4.14}$$

When this relation is used the moment balance is as given in Equation 4.15.

$$\sum M_B = F_y\gamma_4 L(n\cos(\phi_2) + \sin(\phi_2)) - T_4 = 0 \tag{4.15}$$

By rewriting the moment balance the relation of the pull-out force F_y is given by Equation 4.16.

$$F_y = \frac{T_4}{\gamma_4 L(n\cos(\phi_2) + \sin(\phi_2))} \tag{4.16}$$

The kinematics can also be determined by using a load vector and a Jacobian with the mapping of the mechanism coordinates to the deformation angles. This method is used to provide smoother results of the force-deflection plots but is not used for the parametric study, as it has significantly greater computational time. A description of this method is given in Appendix B. Furthermore, in Appendix A the source code for the implemented model can be found. By following the procedure that is described in this section, the first and main sub-goal of this thesis is accomplished, which contains determining the pull-out force for a defined mechanism and object in a specified load case.

5

Experimental Validation

In the realm of engineering and scientific modelling it is very important to have a correct representation of real-world physics, in order for a model to be reliable and a design to be successful. The focus of this chapter is to describe the validation process, such that the accuracy of the model that is described in chapter 4 can be determined. With this validation not only the MATLAB model is validated, but also valuable insights are gained about the behavior of the system, reinforcing the practical applicability of our computational predictions.
In this chapter, the goal of the validation is described. Furthermore, the design process and iterations of designing an accurate test setup is described. Lastly, a test procedure is given in which the steps of an experimental test are described.

5.1. Validation goal

In chapter 4 an extensive description of the methodology of the extension of the PRB-model is given in order to predict the pull-out force for a certain load case with chosen design parameters. In this model, the design parameters of most interest are the enclosing angle ψ, and the thickness of the gripper finger h, which is in line with the main design goal of this project, as these parameters were found to be challenging parameters in the design of an encompassing, everting gripper for cluttered environments. In order to validate this model to gain insight into the accuracy of the model with respect to the real-world representation it is necessary to recreate the setup of the model as accurately as possible. The goal of this experimental validation is therefore to recreate an accurate real-world representation of the model, where the results of the model, which are the forces on the tip of the model, for several design parameters ψ and h can be compared to the real-world forces on testpieces with similar design parameters.
To translate the validation goal to functions that the test setup should have, the following parts of the model are considered essential:

1. Comparing modelled forces with reality: By adding load sensors in the xy-plane the reaction forces at the base of the curved gripper finger can be measured and compared to the modelled reaction forces.
2. Moving the object in the y-direction: To move the object in only one direction, the object can be constrained to one degree of freedom by using a linear guide. The object can be moved by using a linear actuator, such as a stepper motor that is coupled to a spindle.
3. Studying change in parameters ψ and h: Testpieces of several thicknesses and several enclosing angles should be made. By using 3D printing, these changes in parameters are easily satisfied in production.

A sketch of a these key elements in a test setup design is shown in Figure 5.1.

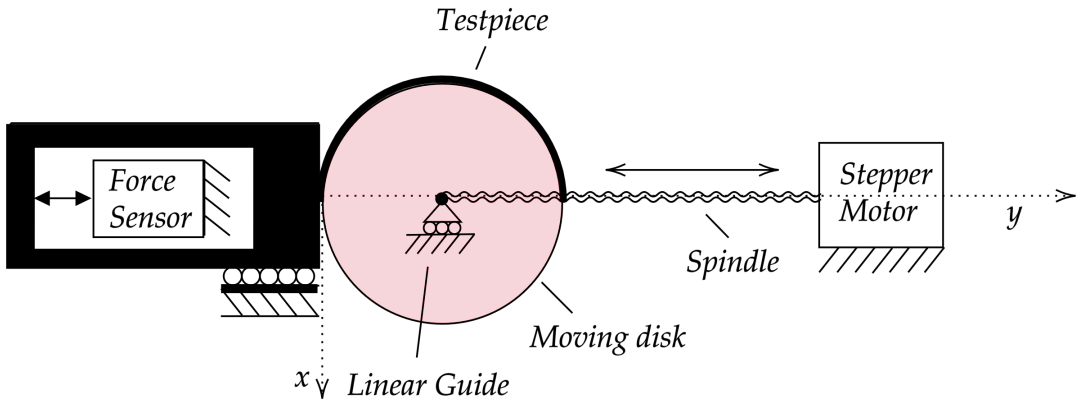

Figure 5.1: Illustration of the test setup: the moving disk is extracted in the y-direction from the curved testpiece with a linear stage consisting of a linear guide and a spindle, driven by a stepper motor. The reaction forces on the freely moving testpiece are measured by compressing on a force sensor mounted to the environment.

5.2. Test setup design

As the goal states, it is necessary to create a test setup that is an accurate representation of the model. Therefore, there are several key points of interest that have to be taken into account when designing a solid test setup, which translate in the following requirements:

1. The design has to be robust, such that unwanted deformations within parts of the setup are kept as small as possible. When measuring force any deformations in parts that are considered rigid reduces the accuracy of the measurements and increases the overall error of the force evaluation.
2. As the model is planar, the setup also has to be designed as if all forces act only in the xy-plane. In a three-dimensional environment this means that the median of the force that acts in the setup has to be at the same height in the z-direction.
3. The overall setup has to be correctly aligned, such that when force is measured in the x-direction the correct forces in that direction are measured, as well as for the y-direction. Misalignments in the xy-plane and in the z-direction result in additional moments that affect the accuracy of the measurements and add loads that are not modelled.
4. Load sensors are preferred to be loaded by compression instead of tension, as when a ball joint is added to the sensor the sensor measures the correct direction of the load when it is compressed, while when the load is applied in a tension-like structure, small misalignment could cause a change in the direction of the load.
5. Vibrations in the setup should be minimized, such that the amount of noise in the experimental data is small. This includes external vibrations, such as vibrations in the environments, as well as internal vibrations such as vibrations caused by actuators/motors.
6. Friction forces should be minimized, as these types of forces are neglected in the model.

5.2.1. Design iterations

In the process of designing a robust test setup, there were several iterations the design process went through. The first iteration did not satisfy all the requirements as described above, which gave insight into adding more requirements to the list of requirements. The first design iteration implemented the linear guide with a stepper motor as the motion stage, but this first concept was not designed with the planar view, which resulted in a design with a height difference in z-direction between the axis of motion and the location at which the forces where measured, which would result in moments around the x-axis.

The second iteration was already close to the final iteration, as this had a robust design and was designed with the planar view in mind. Several small detailed design iterations were implemented to result in the final design, which will be further described in the next section.

As only the final design is used for validating the model, the earlier stages of design are not further elaborated in the main matter of this thesis. More details about earlier design concepts can be found

in Appendix C.

5.2.2. Final test setup design

The test setup can be categorized into three main sections:

1. Motion stage: The moving object, disk, that is mounted on a linear guiding stage and is actuated via a spindle to a stepper motor.
2. Force measurement stage: The section where the testpieces are mounted and connected to the load cells such that the reaction forces can be measured.
3. Measurement devices: The different sensors in the test setup, such as the load cells to measure the reaction force and a distance sensor to measure linear displacement of the motion stage.

These sections are visualized in Figure 5.2, where the important parts of the setup are numbered.

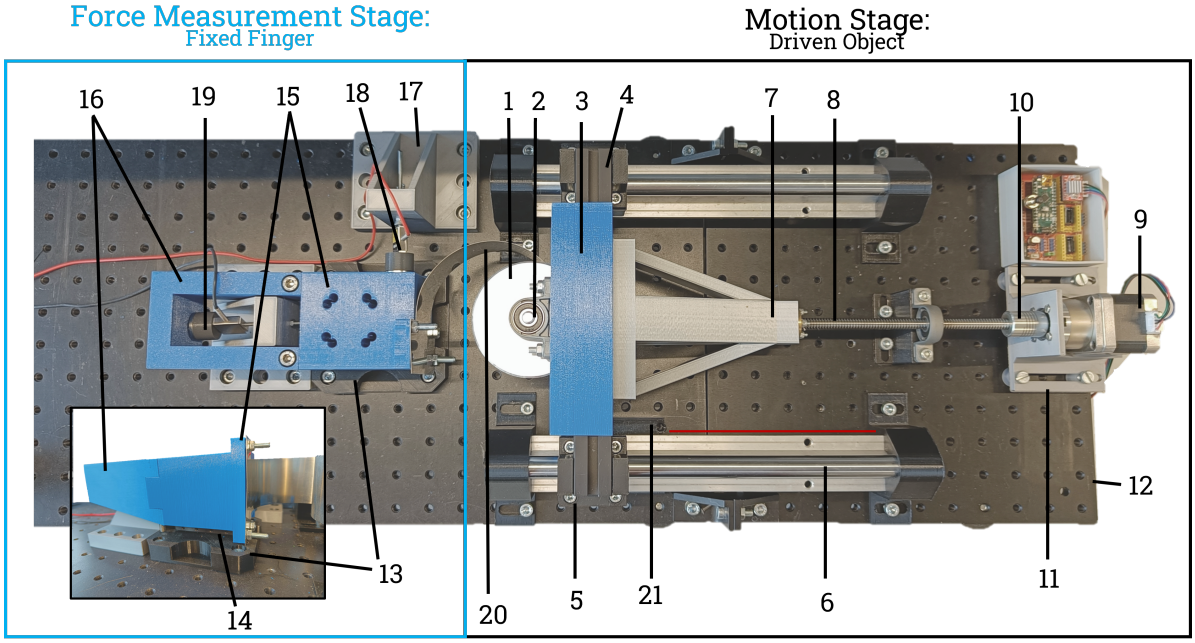

Figure 5.2: Numbered overview of the test setup: The motion stage (black) consists of a driven object (1) on a linear slider (5, 6) driven by a spindle (8) and a stepper motor (9) with bellow (10) without friction due to bearings (2). The force measurement stage (blue), consists of the testpiece (20) connected to a two-piece mounting hub (15, 16) on a linear slider (14). The measurement devices consist of a load cell for measuring reaction forces in the x- and y-direction (18, 19) and a laser sensor (21) for measuring the displacement of the object. The setup consists of 3D-printed mounting structures (3, 7, 11, 13, 17), optical rails (4), and a main breadboard (12).

Motion stage

The motion stage, as shown in Figure 5.3, consist of a steel disk (1) with a radius of 80 mm and a height of 50 mm (excluding the axis), which represent the circular object that is modelled and pulled out from the mechanism. This disk is manufactured using a lathe machine. An axis goes through the center of the disk that is connected to two KP8 ball bearings (2). This is done to let the disk rotate freely and therefore no slip occurs between the disk and the test piece, reducing errors due to friction. The ball bearings are connected to a 3D-printed mounting structure (3), which connects the upper and lower bearings and has a cap at the top to align the top surface of the disk parallel to the xy-plane. The mounting structure is connected to two THORLABS XE25L225/M optical rails (4), which are themselves connected to two SBR16UU linear bearings (5) that fit onto the SBR16 linear guiding stage (6). The optical rails also is connected to a 3D-printed stiff structure that holds the lead screw (7) which can move over the spindle (8). The spindle then is connected to the NEMA17-05GM stepper motor with gearbox (9) via a bellow coupling (10) to reduce vibrations of the motor and misalignments in the connection. The spindle is supported with a KP8 ball bearing (2). The motor is supported by a 3D-printed stage

that rests on soft plastic spacers (11) to reduce any more vibrations. The stepper motor is controlled using an Arduino Nano board and an A4988 stepper driver. In the Arduino Nano a GRBL script as provided in Appendix D is uploaded such that the stepper motor can be controlled via software called UGS Platform. In Appendix D also further instructions are given on working with this software. All parts are connected with M6 bolts and nuts to either the optical rails or the main THORLABS MB2020/M aluminum breadboard (12).

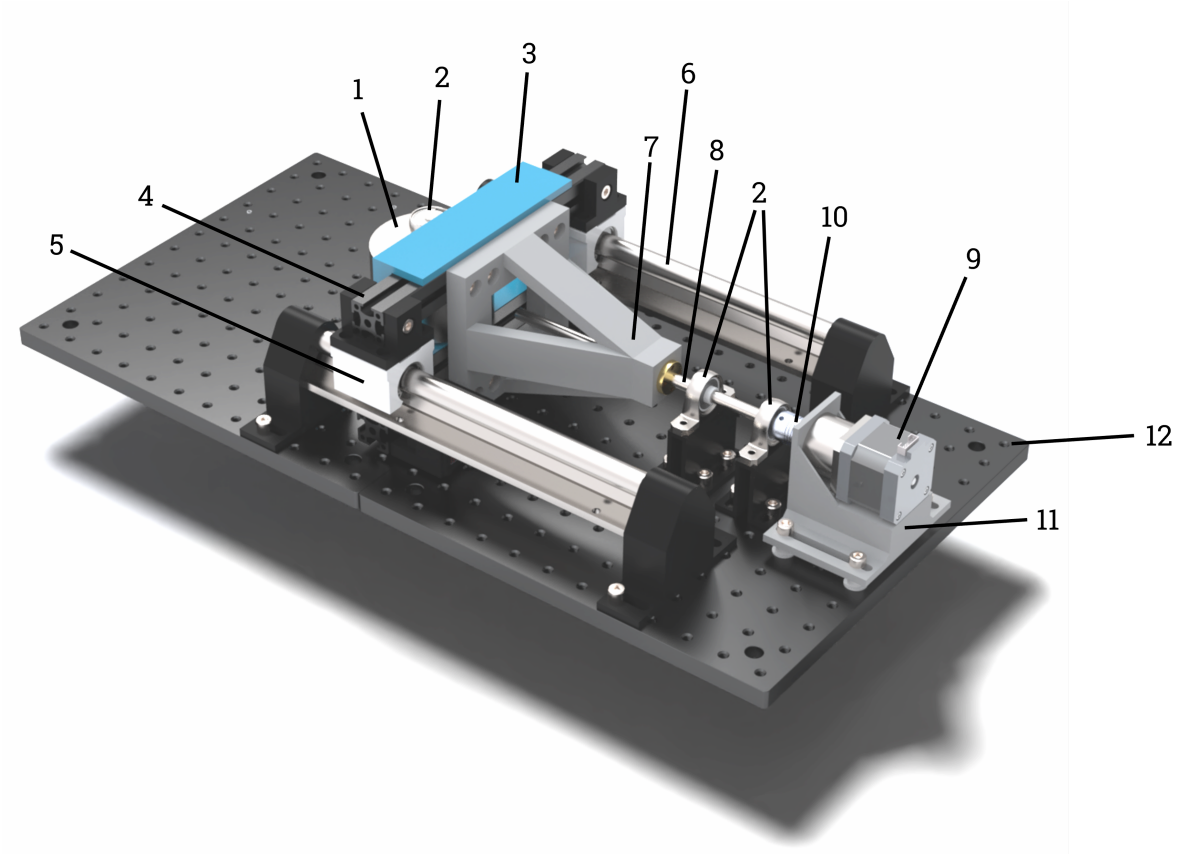

Figure 5.3: Numbered render of the motion stage: The motion stage consists of a driven object (1) on a linear slider (5, 6) driven by a spindle (8) and a stepper motor (9) with bellow (10) without friction due to bearings (2). The stage consists of 3D-printed mounting structures (3, 7, 11), optical rails (4), and a main breadboard (12).

Force measurement stage

The stationary stage, as shown in Figure 5.4, consists of a 3D-printed baseplate (13), which is mounted on top of the THORLABS MB2020/M aluminum breadboard (12). This baseplate has semi-circle cuts, to provide room for the lower ball bearing of the motion stage. Furthermore, the baseplate has in both x- and y-direction four holes such that the next part, the PMB RTS-2065 linear motion stage (14), could be mounted. This PMB RTS-2065 can therefore be connected for either the x- or y-direction at once, which gives the possibility to measure forces either in the x-direction or the y-direction. On top of the linear motion stage, the main 3D-printed testpiece mounting hub is connected via M3 screws. This mounting hub consists of two sections. The main section (15) will always be connected to the linear motion stage and provide the hub for the testpieces. When testing in the y-direction is done, the second section of the mounting hub (16) is connected via two M6 bolts and nuts to the first section of the mounting hub. In this way, the mounting hub gains a saddle that makes compression against the y-direction load cell possible. The load cells are connected to 3D-printed structures (17) and connected to the breadboard. There is a load cell for the x-direction (18) and a load cell for the y-direction (19). A diagonal slab is added to provide high stiffness and a rigid base for the load cells, reducing unnecessary deformation. Testpieces (2) are connected to the main hub. In the validation, two materials are used for the testpieces, which are stainless steel and PLA. The mounting hub as described is suitable for the stainless steel leaf spring testpieces, as they can be mounted with M4 bolts to the main hub. For the PLA testpieces

several types of connection hubs were designed and iterated, but the final design was a fully massive 3D-printed hub. More details about the early stage testpiece iterations can be seen in Appendix E.

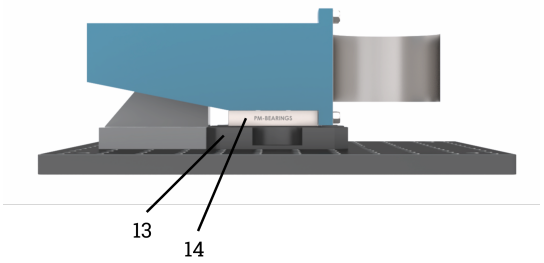

(a) Side view of the force measurement stage: the mounting hub rests on a linear slider (14) and a 3D printed mounting structure (13).

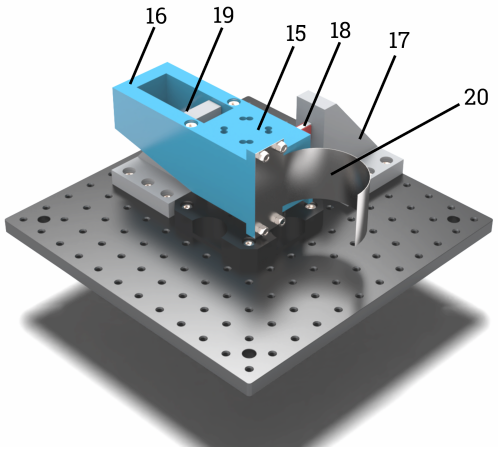

(b) Isometric view of the force measurement stage: The testpiece (20) connects to the two-piece test mounting hub (15, 16). Reaction forces are measured by load cells in the x-direction (18) and the y-direction (19), that are connected to 3D printing mounting structures (17).

Figure 5.4: Numbered side view and isometric view of the render of the force measurement stage: The force measurement stage consists of the testpiece (20) connected to a two-piece mounting hub (15, 16) on a linear slider (14). Reaction forces are measured by load cells in the x-direction (18) and the y-direction (19). The stage consists of 3D-printed mounting structures (13, 17), and a main breadboard (12).

Measurement devices

The main result of the PRB-model is the force-displacement relation when the object, disk, is moved. Therefore, the two main types of measurement are:

1. Measuring the reaction force
2. Measuring the displacement of the disk

The forces are measured by using a Futek LSB200 load cell of a resolution of 10 lbs and 5 lbs for respectively the measurement in y-direction (19) and x-direction (18). These load cells are connected to a base as described in the previous section and as shown in Figure 5.5a. The load cells are extended with a mount in which a roller ball is located. This is done such that the force applied is a point contact, the direction is in line with the measuring direction, and possibly friction, when tangential movement occurs, is not transferred to the load cell.
The displacement of the object is measured by using a Micro-Epsilon ILD1420-500 laser sensor (21). The laser sensor is mounted in a 3D-printed enclosure and connected with M6 bolts to the lower optical rails, as shown in Figure 5.5b. The laser shines at the mount for the linear guide, which is a black smooth surface and therefore suitable for optical measurements.
Both load cells and the laser sensor signals were processed using an NI USB 6008 I/O device. With the help of this data processor and the lab software LABVIEW, the analog sensor signals were converted to readable digital signals, that could give plots of the measured signal data over time. The LABVIEW script can be found in Appendix G.

5.3. Testpieces

For the experimental validation, multiple testpieces were manufactured. Several experiments were conducted to study the accuracy of a testpiece and eventually two main testpieces were used for the final result as they were found the most reliable and sturdy in the design and provided the best results. More details about the testpieces that were used to generate the final testpieces can be found in Appendix E. In this section a description is given about the two testpieces that are used for the final validation.
The final validation tests were conducted with a testpiece made of polylactic acid (PLA) and a testpiece made of stainless steel 1.4310. The dimensions and properties of these testpieces are depicted in Table 5.1.

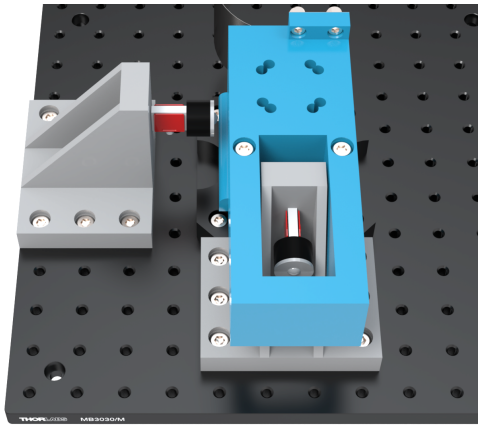

(a) Illustration of the location of the Futek LSB200 load cells.

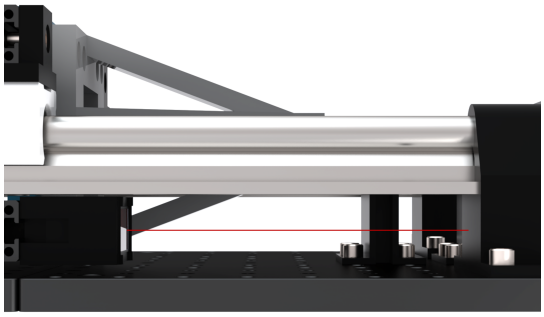

(b) Illustration of the location of the Micro-Epsilon ILD1420-500 laser sensor.

Figure 5.5: The location of the measurement devices. Figure 5.5a depicts the locations of the Futek LSB200 load cells and Figure 5.5b depicts the location of the Micro-Epsilon ILD1420-500 laser sensor.

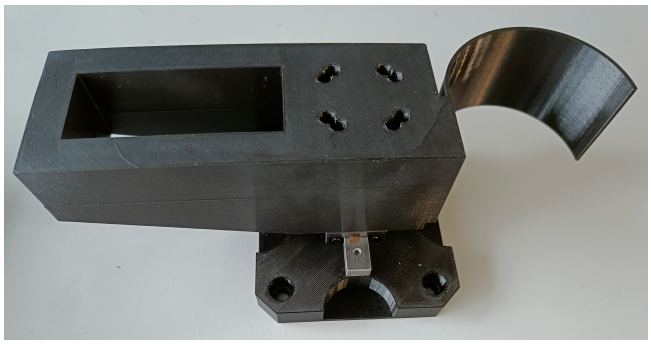

(a) The PLA testpiece, 3D-printed as one solid with the testpiece mounting hub.

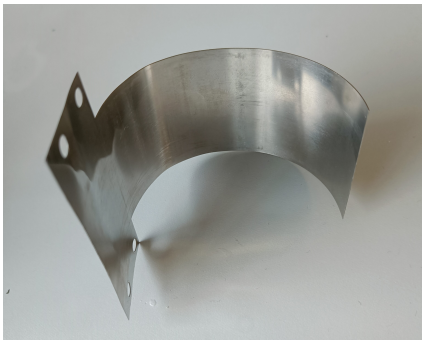

(b) The stainless steel testpiece, laser cut and curved.

Figure 5.6: Pictures of the testpieces that are used for the final validation.

The PLA testpiece is manufactured by 3D printing. It is printed as a solid with the testpiece mounting hub, such that a rigid connection is made between the testpiece and the mounting hub. The hub and the testpiece were printed with 100 $\%$ infill to ensure as much homogeneity of the material as possible. However, a characteristic of 3D printing is that the 3D printed material is not completely homogeneous and therefore the material properties are not exactly known. For this reason, a Young's modulus test is conducted such that a correct value is used for the simulation. The description of this Young's modulus test can be found in Appendix F. This resulted in a Young's modulus for the 3D printed PLA of 2.55 GPa, while the conventional Young's modulus is equal to 3.5 GPa.
The stainless steel testpiece is manufactured by laser cutting the profile of the testpiece out of a stainless steel leaf spring and bending it in the correct radius and curvature by using cylinders with a small radius such that the plastic region of the leaf spring is reached. The stainless steel testpiece is bolted to the testpiece mounting hub to obtain a rigid connection.
A picture of the testpieces can be found in Figure 5.6.

Parameter	PLA	Stainless steel 1.4310	Unit	Description
h	2	0.3	mm	Thickness of the finger
ψ	180	180	$^\circ$	Enclosing angle of the finger
w	50	50	mm	Width of the finger
E	2.55	195	GPa	Young's modulus of the material

Table 5.1: Dimensions and properties of the PLA and stainless steel testpieces that are used in the validation.

5.4. Test procedure

The experiments are done in a structured way, such that every time a measurement is taken, the same procedure is used. This reduces deviations in different measurements. The main steps of the experiments are written in a test procedure, which is described below.

1. Connect and set up the measurement devices.
   (a) Provide a power supply to the load cells and distance laser.
   (b) Connect the data acquisition system, NI USB 6008 I/O, to the PC/laptop via USB.
   (c) Open the LABVIEW code.
   (d) Select the correct analog to digital ports to provide an input signal in the LABVIEW software.
   (e) Check if the sensors work by applying force on the load cells and use a surface that can be moved when in line with the laser to check if the distance sensor works.
2. Connect and set up the stepper motor.
   - Provide a power supply to the Arduino NANO and therefore also the motor driver.
   - Open the Arduino IDE software and upload the GRBL code which is provided in Appendix D. This only has to be done the first time the Arduino is used.
   - Open the UGS Platform software.
   - Connect the stepper motor with the instruction provided in Appendix D.
   - Set the travel distance and speed of the stepper motor.
3. Calibration.
   - It is possible that the load cells have an initial value that is not equal to zero when it is unloaded. To measure the correct values of the reaction forces it is necessary to calibrate the load cells. This is done by making sure the load cells are unloaded and then setting the measured value in LABVIEW to zero with the offset function.
4. Test x-direction.
   - Connect the testpiece to the testpiece mounting hub.
   - Align the testpiece mounting hub to the center of the disk.
   - Align the load cell for the x-direction measurement to the surface of the tespiece mounting hub. Make sure the calibration is still right, else adjust it.
   - Move the disk to the initial position, which is the position in which the curved testpiece fully encloses the disk.
   - Add the path in which the data files should be saved.
   - Check the saving box in LABVIEW.
   - Run the LABVIEW code.
   - Start moving the disk with the UGS Platform software.
   - Stop running the software when the preferred travel distance is reached.
   - Uncheck the saving box in LABVIEW.
   - Move the disk back to the initial position.
5. Recalibrate.
   - When testing in one direction is finished, the setup has to be adjusted for the measurements in the other direction. First, the mounting hub and base plate have to be unscrewed from their surfaces to rotate these parts 90 degrees.
   - When testing in the y-direction will apply, add the saddle part of the testpiece mounting hub.
   - Make sure the load cell of the y-direction measurements is placed at the right distance of the saddle, such that the saddle compresses the load cell when the disk starts to move.

- Calibrate the load cell as described above.

6. Test y-direction.
   - Connect the testpiece to the testpiece mounting hub.
   - Align the testpiece mounting hub to the center of the disk.
   - Align the load cell for the y-direction measurement to the surface of the tespiece mounting hub. Make sure the calibration is still right, else adjust it.
   - Move the disk to the initial position, which is the position in which the curved testpiece fully encloses the disk.
   - Add the path in which the data files should be saved.
   - Check the saving box in LABVIEW.
   - Run the LABVIEW code.
   - Start moving the disk with the UGS Platform software.
   - Stop running the software when the preferred travel distance is reached.
   - Uncheck the saving box in LABVIEW.
   - Move the disk back to the initial position.
7. Data processing.
   - Find the path where the data is saved.
   - Import the data in MATLAB.
   - Process the data as preferred.
   - Determine the maximum values of the force plots in the experimental and simulated results.
   - Determine the error between the simulation and the experiment based on these maximum values. For the experimental values, the median of the maximum values is used.

6

Parametric Study

In the previous chapter, the validation of the model is described. When a model is validated it can be used for the purpose it is designed. To answer the research question of this thesis it is necessary to gain knowledge about the relation between relevant parameters. This knowledge is gained by adjusting the parameters in the model to determine how much a certain parameter influences the overall performance of a design. This is called a parametric sweep. In this chapter, the setup and methodology of the parametric study is described.

6.1. Load case and constant parameters

In the model, some constant values will not change during the parametric study. These parameters are determined by setting a certain load case for which the parametric study is relevant. The load case that is used in this research is described as follows:

- The gripper consist of three grasping fingers ($n_f = 3$) to prevent an object from falling out due to disturbances. Therefore, it is assumed that on each finger a third of the total weight of the object applies.
- The gripper fingers have a width w of 20 mm.
- The object that will be grasped is a sphere with a diameter of 60 mm and a mass m of 100 g, as this is an approximation of a tomato.
- The gravitational constant g is considered to be 9.81 m/s^2.
- The cross-sectional area of the finger is considered to be rectangular and therefore the area moment of inertia, I, is equal to $\frac{wh^3}{12}$, where w is the width of the finger and h is the thickness of the finger.

6.2. Variables

The variables parameters are the design parameters that are of interest when making design choices. These parameters are not known beforehand, but are preferred to be varied and directed in such an optimal way, that the best design can be generated. These variables are:

- Finger thickness, h.
- Enclosing angle, ψ.
- Material, where in this model only the Young's modulus, E, has to be known.

6.3. Parametric Sweep

The MATLAB model is executed iteratively for different combinations of the values of the variables h, ψ and E. This is called parametric sweep. For practical reasons, the model is executed with a for loop for the enclosing angle and a for loop for the thickness simultaneously and this process is repeated

manually for the two different materials that are used in the study, which are the 3D-print material polylactic acid (PLA) and the leaf spring steel material. Therefore, in total two parametric sweeps were performed.
The array values that were used for the sweep can be found in Table 6.1.

Table 6.1: The array values that are used in the parametric sweep.

Variable	Values sweep 1	Values sweep 2	Unit
E	3.5 (PLA)	195 (Stainless steel)	$[GPa]$
h	[0.5 : 0.05 : 2.5]	[0.1 : 0.01 : 1]	$[mm]$
ψ	[135 : 5 : 180]	[135 : 5 : 180]	$[°]$

For each value of the three variables shown in Table 6.1 all combinations are made and modelled. The process of one parametric sweep is therefore as follows:

1. Select a material and therefore the correct value of the Young's modulus.
2. The for loop starts and therefore a value for the thickness h and a value for the enclosing angle ψ, is taken.
3. For each combination of variables the model as described in chapter 4 is executed.
4. For each iteration the maximum value of the pull-out force F_y is stored in an array.
5. When all combinations for all values of the three variables are reached and therefore all values of the maximum pull-out force are calculated the iteration stops.
6. Each maximum value of the pull-out force is plotted with respect to an array of thickness values, as can be seen as an example in Figure 6.1. This plot can be made for each instance of the enclosing angle values, that were given in the array depicted in Table 6.1.
7. The pull-out force of the object for the chosen load-case is calculated, $F_z = mg$, and added to the plot of the maximum pull-out forces.
8. All maximum value plots can be interpolated in order to find to intersection point between the maximum value plots for each enclosing angle and the pull-out force of the object. This can be done with the help of Equation 6.1 and Equation 6.2.
9. All intersection points represent the limit for the thickness and enclosing angle at that load case. These intersection points can be plotted such that the relation between the thickness and enclosing angle for a certain load case and for a certain material can be seen.

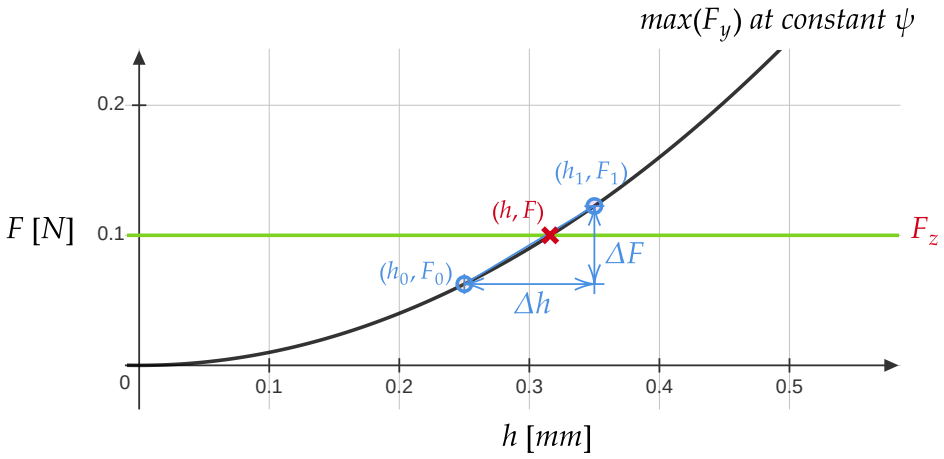

Figure 6.1: Plot of the maximum pull-out force with respect to the thickness (black line), for each value of the enclosing angle, and the pull-out force of the object in a certain load case (green line). The difference between the x-axis values and y-axis values of resp. the thickness and the force are shown for two coordinates in the plot in order to calculate the interpolation values. The intersection point (red cross) represents the relation between the the thickness and enclosing angle.

Below, the equations for the interpolation between the maximum force values at certain thicknesses is depicted. The h_0 and h_1 represent the x-coordinates, e.g. the thickness values, of two maximum force values and F_0 and F_1 represent the y-coordinates, e.g. the maximum force values. To find the correct thickness h in Equation 6.2 the value for F is equal to the value of the force limit F_z.

$$\frac{h - h_0}{F - F_0} = \frac{h_1 - h_0}{F_1 - F_0} = \frac{\Delta h}{\Delta F} = n_i \tag{6.1}$$

$$h = n_i(F - F_0) + h_0 \tag{6.2}$$

7

Results

In chapter 4, chapter 5 and chapter 6 the overall methodology of this thesis is described. In this chapter the results of this methodology are presented. First, the results from the experimental validation are presented, and lastly the results from the parametric study.

7.1. Experimental validation

Experiments were done with different test pieces. The main results of two testpieces with either PLA or stainless steel as material are described in the following sections. For each of the described results the test setup, as described in chapter 5, were used for ten iterations, which means that there were ten experimental results for the force-deflection measurement in either x- and y-direction.
Multiple tests were done for different types of testpieces, but during testing, several adjustments to the test setup were made to make the results more robust. Therefore, the final test results are shown in this chapter.

7.1.1. Test: polylactic acid (PLA)

The force-deflection plot that was generated during the measurements is shown in Figure 7.1, next to the simulated result. In this graph the red line depicts the reaction force in the y-direction and the blue line depicts the reaction force in the x-direction. The continuous line represents the modelled result and the dotted lines represent the experimental results.
For this test the testpiece was used that is described in chapter 5 and depicted in Figure 5.6a.

In the force-deflection plot, it can be observed that the force in the x- and y-direction have a nonlinear behavior with for the force in the y-direction a maximum of approximately 6.5 N for the simulation and 8 N for the experiment at at displacement of the disk at 15 mm. The maximum value of the reaction force in the x-direction is approximately 8.5 N for the simulation and 9.8 N for the experiment at a displacement of approximately 45 mm, which is a displacement a little further than the radius of the disk, which depicts a behavior that the reaction force in x-direction is not at a maximum at the most outer x-value, which would be the radius of the disk, but a little further. The trend of the force development of the simulated result is very similar to the measured result, where only a difference in the amplitude of the plot is observed.

For evaluating the quality of the experimental results for each force-deflection graph recognizable points were taken. The maximum force values were therefore taken and the error between the maximum values of the simulation and the maximum values of the experiment were determined. The errors are depicted in both the absolute error between the maximum results of the simulated and measured results and the percentile error, which is determined as a ratio of the absolute error and the measured result. These values can be found in Table 7.2.

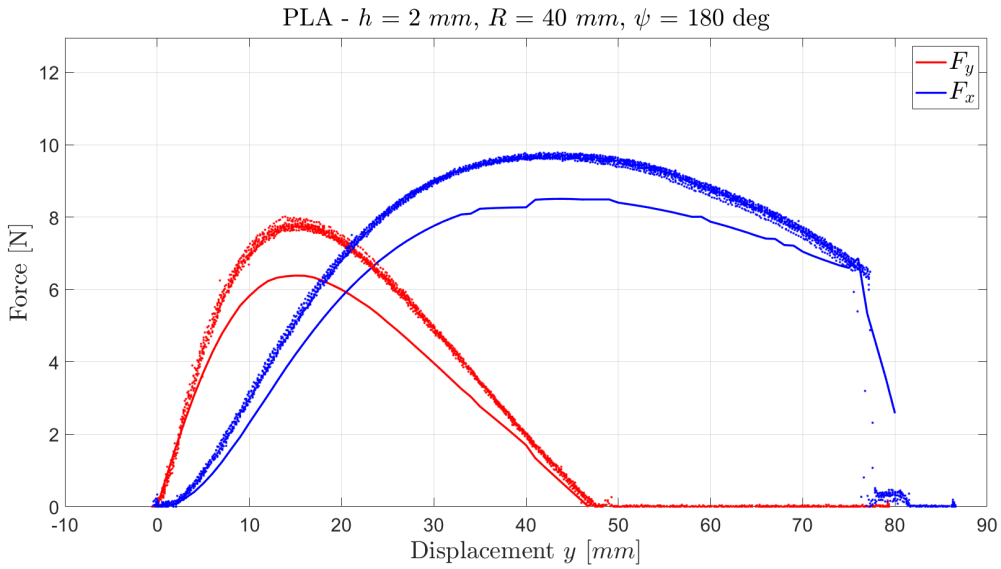

Figure 7.1: Graph of the simulated and experimental results of the tip force in the x-direction (blue line) and the y-direction (red line). The continuous line depicts the measured result and the dots represent the measured values. Material: PLA.

Table 7.1: Maximum and error values of the test with PLA testpieces. The errors are presented as absolute differences between the maximum values of the simulated and measured results ($e_{|\Delta|}$) and as a percentage of the measured values (e).

	Simulation $[N]$	**Experiment** $[N]$	$e_{\|\Delta\|}$ $[N]$	e [%]
max F_x	8.5036	9.6960	1.1924	12.30
max F_y	6.3847	7.7795	1.3948	17.93

7.1.2. Test: stainless steel 1.4310

The force-deflection plot that was generated during the measurements is shown in Figure 7.2, next to the simulated result. In this graph the red line depicts the reaction force in the y-direction and the blue line depicts the reaction force in the x-direction. The continuous line represents the modelled result and the dotted lines represent the experimental results. For this test a testpiece was used that was described in chapter 5 and depicted in Figure 5.6b.

In the force-deflection plot, it can be observed that the force in the x- and y-direction have a nonlinear behavior with for the force in the y-direction a maximum of approximately 1.6 N for the simulation and 1.4 N for the experiment at at displacement of the disk at 15 mm. The maximum value of the reaction force in the x-direction is approximately 2.3 N for the simulation and 1.6 N for the experiment at a displacement of approximately 45 mm, which is a displacement a little further than the radius of the disk, which depicts a behavior that the reaction force in x-direction is not at a maximum at the most outer x-value, which would be the radius of the disk, but a little further. It can be observed that the locations of the maxima for the testpiece of PLA and the testpiece of the leaf spring are at the same value of y and therefore the trend of the force-displacement graph in the simulation is the same as the trend of the force-displacement graph for the experiment. However, a slight deviation in the shape between the measured and simulated force development is observed.

For evaluating the quality of the experimental results for each force-deflection graph recognizable points were taken. The maximum force values were therefore taken and the error between the maximum values of the simulation and the maximum values of the experiment were determined. These values can be found in Table 7.2.

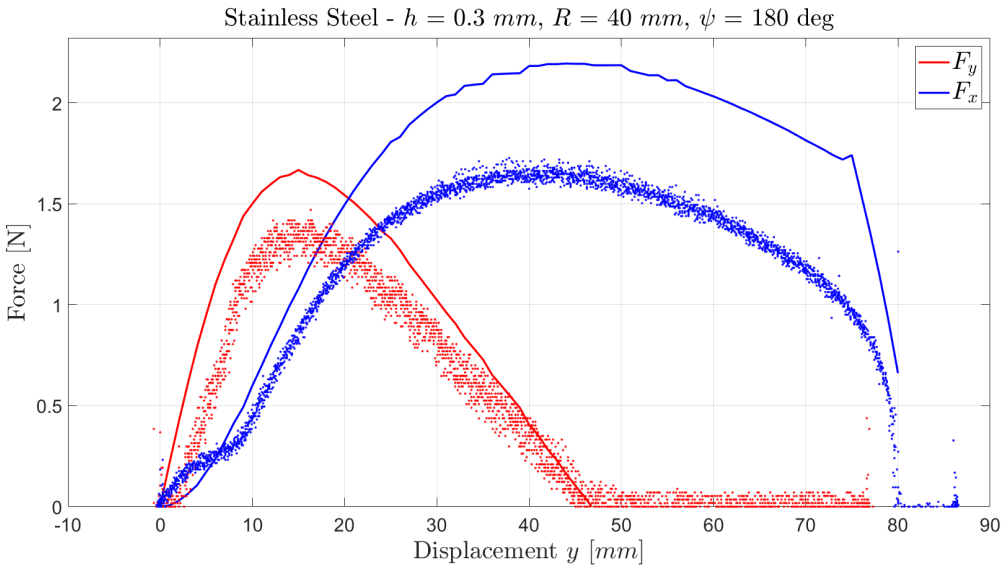

Figure 7.2: Graph of the simulated and experimental results of the tip force in the x-direction (blue line) and the y-direction (red line). The continuous line depicts the measured result and the dots represent the measured values. Material: Stainless Steel 1.4310.

Table 7.2: Maximum and error values of the test with leaf spring testpieces. The errors are presented as absolute differences between the maximum values of the simulated and measured results ($e_{|\Delta|}$) and as a percentage of the measured values (e).

	Simulation $[N]$	**Experiment** $[N]$	$e_{\|\Delta\|}$ $[N]$	e $[\%]$
max F_x	2.1956	1.6670	0.5286	31.71
max F_y	1.6540	1.4000	0.2540	18.14

7.2. Parametric study

The parametric study is done for multiple values of w, which is the width of the gripper finger. In this section, only the results when a width of 20 mm is chosen are shown, as this is the value in which the study is done for both PLA and stainless steel and therefore are easier to compare. Additional results can be found in Appendix H.

The parametric sweep is done for different values h and ψ and for different materials in a load case, which is also described in chapter 6. The results of the parametric sweep for PLA as material can be seen in Figure 7.3 and for stainless steel in Figure 7.4. In these plots, the nonlinear lines represent the relation between the maximum values of the pull-out force in relation to the finger thickness h, in which the enclosing angle ψ is kept at a constant value. Ten instances of this plot for a value of the enclosing angle ranging from 135 degrees to 180 degrees are depicted in the graph. The force limit, which is the payload of the tomato, is depicted in black and is divided by the number of fingers that the gripper has. The red crosses depict the intersection points between the ten plots and the force limit, resulting in the ultimate combination for a value for h and ψ where the finger can hold the payload.

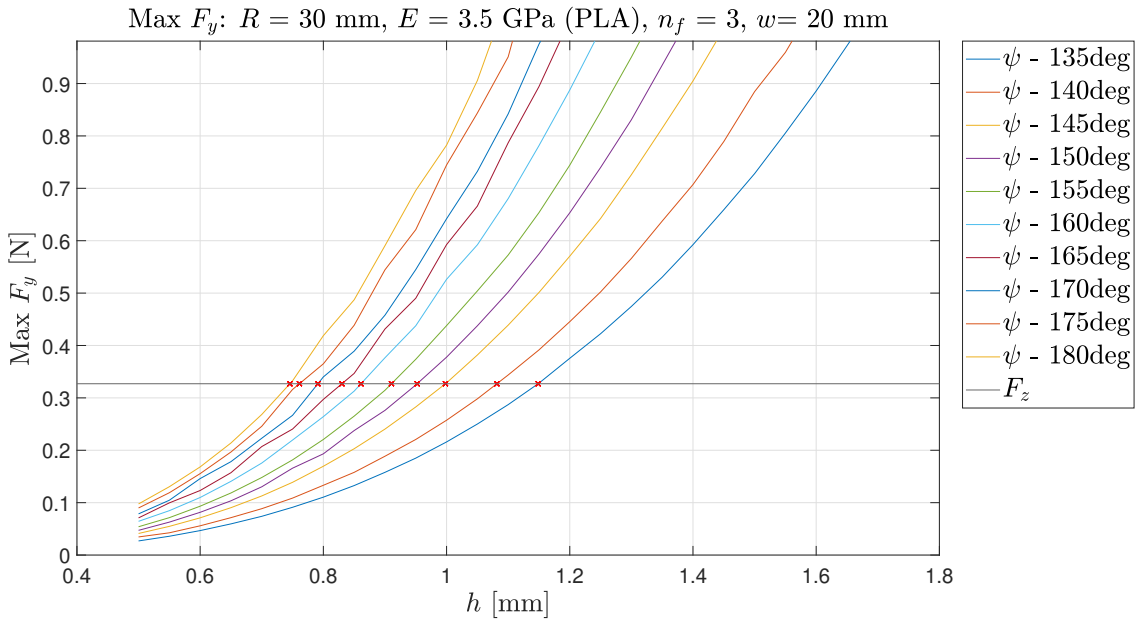

Figure 7.3: Relation between the maximum pull-out force F_y and the thickness h, at different constant values of the enclosing angle, ψ. The black line depicts the force limit in the parametric study, based on the gravitational force due to the weight of the object in the load case. The red crosses depict the intersection points between the maximum force-thickness plot and the force limit. Chosen material: PLA.

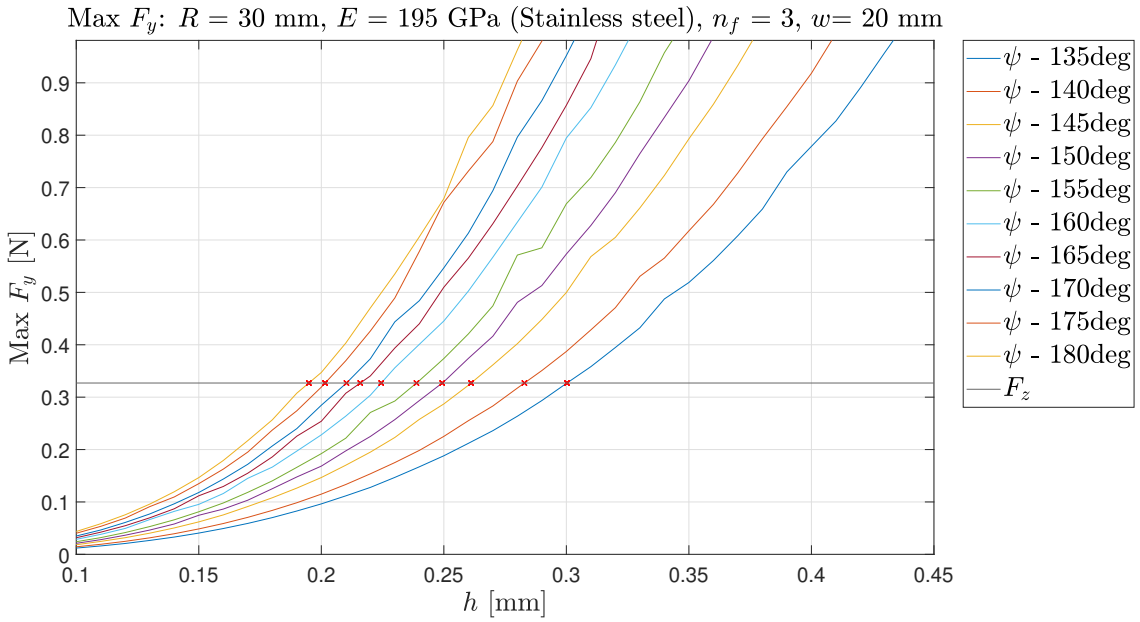

Figure 7.4: Relation between the maximum pull-out force F_y and the thickness h, at different constant values of the enclosing angle, ψ. The black line depicts the force limit in the parametric study, based on the gravitational force due to the weight of the object in the load case. The red crosses depict the intersection points between the maximum force-thickness plot and the force limit. Chosen material: Stainless Steel 1.4310.

By finding the intersection points between the nonlinear plots and the force limit, the relation between the enclosing angle ψ and thickness h can be found for a certain load case. This is done for both materials and these points are plotted in Figure 7.5. The circles represent the intersection points. A 3rd-degree polynomial is fitted for these intersection points, which is depicted in the figure by the continuous lines. This is done to give more insight into the guessed relation between the parameters in between the swept parameter values. By these polynomial fits a nonlinear relation between the

enclosing angle and finger thickness can be observed. A more detailed version of each of these plots apart from each other can be found in Appendix H in Figure H.4b and Figure H.3b. In Appendix H also the results of the sweep for multiple values of the width, w, for a stainless steel finger can be found in Figure 9.1.

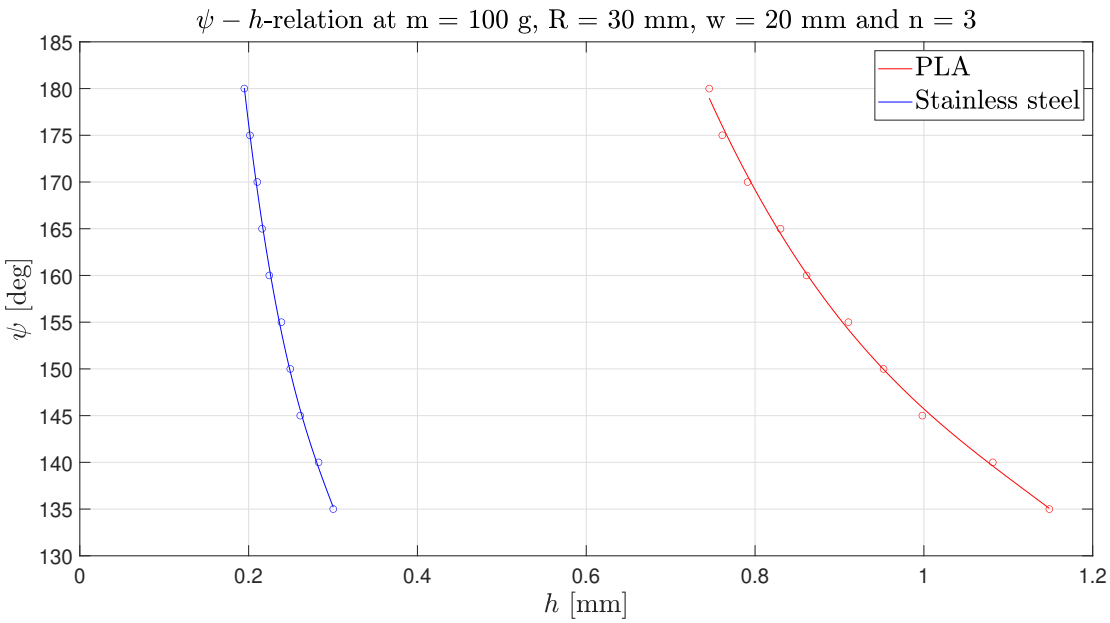

Figure 7.5: Design chart: The relation between the enclosing angle ϕ and finger thickness h for either stainless steel and PLA as material. The circles represent the intersection points of the force limit and the force-thickness plots and the continuous lines represent the fitted polynomial plots.

8

Discussion

8.1. Experimental validation

The results obtained by the experimental setup show a similar trend in the force development as the simulated results, showing that the model predicts the direction of the reaction force between the object and the fingertip accurately. Furthermore, recognizable locations of the force development, such as the maximum values and the intersection points with the x-axis of the plot, match both the measured and simulated results. This shows that the maximum reaction force in the x-direction and the change of direction in the force in the y-direction is at a displacement of 45 mm, which is a little further than the radius of the object. Furthermore, it is observed that the measured reaction force in the y-direction has no negative component, which is explained by the fact that the load cells were only compressed when the testpiece was being pulled due to the extraction of the object, while after 45 mm displacement the testpiece was pushed back by the object, resulting in loss of contact to the load cells.

However, also errors are observed between the measured and simulated results, primarily visible in the magnitude of the force and the deviating trend of the force development for the stainless steel testpiece. These errors are categorized as systematic errors and measurement errors, where the systematic errors lead to a scaling error of the overall results and the measurement errors lead to discrepancies between the results for each experiment iteration.

8.1.1. Systematic errors

Discrepancies in the parameters used in the model

Errors occur due to the incorrect assignment of certain values for parameters in the model, such as geometric parameters and material properties. In the fabrication process of the testpieces discrepancies in the desired geometry and the actual realized geometry could occur. This results in small deviations of the thickness, width, radius and enclosing angle of the testpiece compared to these parameters used in the simulation. These geometrical discrepancies can occur for various reasons. First of all, for the PLA testpiece due to the 3D printing manufacturing method, the dimensions have certain limitations and tolerances, due to the nozzle size and support types of the 3D printer. This could result for instance in a slightly bigger or smaller thickness of the PLA testpiece.

For the stainless steel testpiece the tolerances of the laser cutter have to be taken into account. A laser cutter has inaccuracy and therefore the width of the stainless steel test piece could vary slightly. Also, the laser cutter part has small ripples at the edges due to the laser and therefore the width is not a constant value. Furthermore, in the fabrication process of the stainless steel testpiece human errors resulted in geometrical discrepancies, for instance when using the cylinders to apply the correct curvature on the test piece. This is not an easy task and therefore creating the exact preferred radius and enclosing angle was hard and small inaccuracies would result.

Besides the errors in the geometry of the testpieces, the material properties influence the error between the simulated and experimental results. The PLA testpiece is, even though the piece was printed with

100 $\%$ infill, not made of a homogeneous material, due to the 3D printing manufacturing method. The material therefore consists of small cylindrical tubes that have the diametrical size of the printer nozzle. Due to the geometry of the printing layers, the stiffness of the testpiece is not the same in each direction. With the Young's modulus test, it was tried to compensate for these characteristics, but this test was only conducted in one direction and therefore the accuracy of the determination of the Young's modulus is also not perfect.

For the stainless steel testpiece, the Young's modulus is based on the known material properties of the leaf spring. However, due to the laser cutting manufacturing method, a lot of local heat was applied to the leaf spring, which also could have influenced the material properties of the testpiece and therefore discrepancies between Young's modulus that was used for the simulation and the actual Young's modulus of the testpiece.

Calibration of load cells

In Figure 7.2 a notable spread is observed in the experimental result. This spread can be explained due to the resolution of the load cells, which were designed for loads up to 5 lbs for the y-direction and 10 lbs for the x-direction, which is respectively the same as approximately 22 N for the y-direction and 44 N for the x-direction, while the actual reaction forces are not exceeding 2 N in this test. For more accurate results higher-resolution load cells should be used in the validation process. Also, the calibration of the load cells is a factor that could result in small deviations. At the start of each test, the load cells are calibrated, such that a zero force value is found when the load cells are unloaded. This is also taken into account by subtracting the first value of the measured force in the test from the total force, to reduce this initial error. However, the load cells have small deviations from the initial value, which could result in an error in the actual initial value and the used initial value of the load cell when plotting the experimental results.

8.1.2. Measurement errors

Alignment of the test setup

Misalignment of the test setup could cause errors in the measured force. Though the test setup is aligned using a caliper, small misalignments in the test setup could still occur. The main section in which misalignment easily occurs is in the force measurement stage, where the testpiece mounting hub and baseplate have to be rotated 90 degrees when switching from measuring force in the x-direction to the y-direction and vice-versa. The alignment of the testpiece for measuring in y-direction is not hard, as the slider of the testpiece hub is already centered and only the disk has to be aligned in the same y-axis. However, aligning the setup for measurements in x-direction is harder, as the testpiece hub has to be able to freely move in the x-direction, but the load cell also has to be extended such that it touches the testpiece mounting hub and the disk in the motion stage then also has to be aligned perfectly within the curvature of the testpiece, such that no pre-tension occurs in the testpiece when the disk is not moved, but as soon as the disk moves the reaction forces should be measured in the right direction. This requires very accurate alignment and small misalignments could immediately cause big deviations in the measurements, which was especially observed by measuring the reaction forces in the x-direction of the stainless steel testpiece, due to the imperfect curvature of this testpiece. These misalignments could therefore explain the deviations between the error of the tests in the x-direction and the tests in the y-direction and the geometrical error of the stainless steel testpiece and therefore also explains the relatively big error of the measured reaction force in the x-direction.

8.1.3. Error contribution

The contribution of the systematic or measurement errors to the total error value can be determined by using the scaling factor C_e. The scaling factor is determined as given in Equation 8.1.

$$C_e = \frac{F_y^e}{F_y^s} \tag{8.1}$$

In this equation F_y^s is the simulated result of the maximum pull-out force and F_y^e is the median of the measured results of the maximum pull-out force. By multiplying the simulated result by this scaling factor the error between the measurements and simulation in the y-direction becomes zero, as can

be seen in Figure 8.1, and therefore the error between the measurements of reaction forces in the x-direction and in the y-direction can be determined. The remaining error values are then assumed to be systematic errors.

The scaling factor for the measurements with the stainless steel testpiece is equal to 0.8464 and results in a measurement error between the resulted reaction forces in x- and y-direction of 8.75 %.
The scaling factor for the measurements with the PLA testpiece is equal to 1.2185 and results in a measurement error between the resulted reaction forces in x- and y-direction of 0.0687 %.

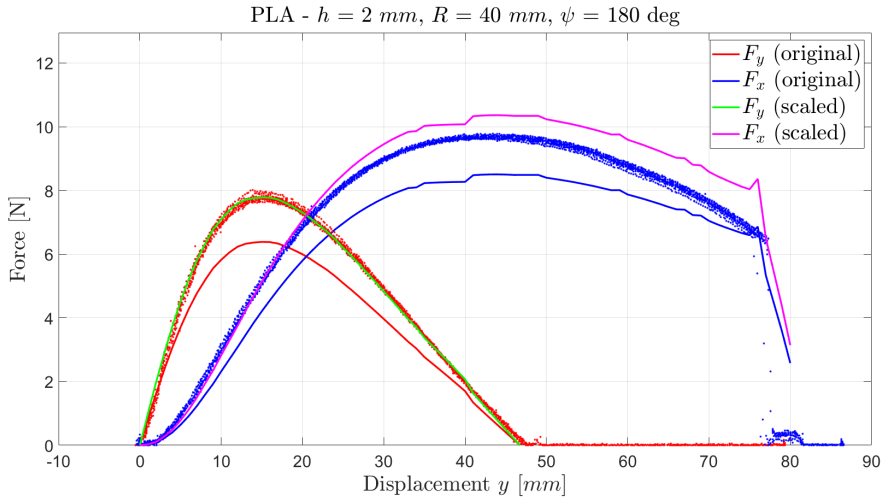

(a) Resulted and scaled reaction forces for the polylactic acid (PLA) testpiece, where $C_e = 1.2185$

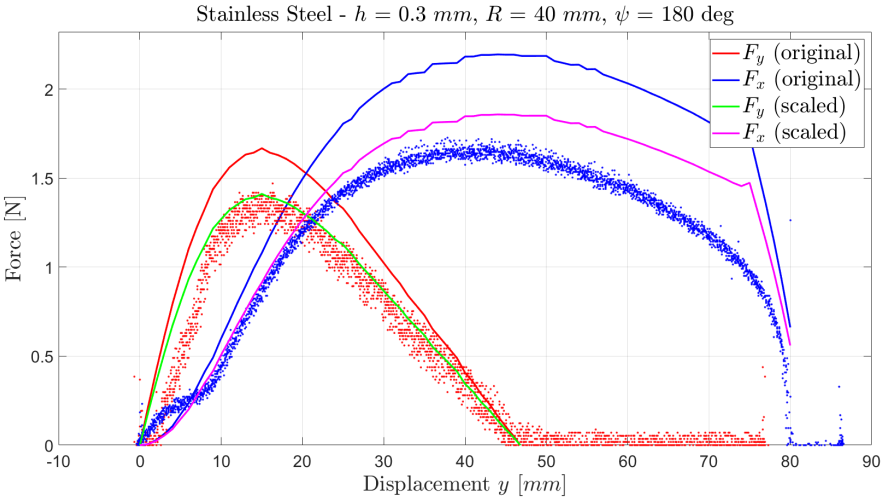

(b) Resulted and scaled reaction forces for the stainless steel 1.4310 testpiece, where $C_e = 0.8464$

Figure 8.1: Influence of the systematic errors on the results: the results scaled with error scaling factor C_e are depicted by the green and magenta lines. The original force results are depicted by the blue and red lines.

From Figure 8.1 it can be seen that when the systematic errors are reduced, which would, for instance, be possible by using the correct Young's modulus, the determination of the pull-out force over the whole displacement is very accurate and the determination of the reaction force in the x-direction is very accurate for approximately the first 30 mm of displacement, which is 75 % of the radius of the object and therefore the most important section of the simulation when it is implemented in design.

8.2. Parametric study

The results of the parametric study, depicted in Figure 7.3 and Figure 7.4, show a nonlinear correlation between the maximum pull-out force and the thickness. The distance between these plots for different enclosing angles increases when the forces become higher, showing an increased impact of the design

parameters h and ψ for higher forces. As the force limit is dependent on the number of fingers that are used, engineers can determine the appropriate number of fingers by identifying intersection points between this force limit and nonlinear plots within the desired range. Figure 7.3 and Figure 7.4 function therefore as a valuable tool for an engineer to determine the wide range of possibilities of design choices when the payload of the object is known.
The resulted design chart, which is depicted in Figure 7.5, illustrates a nonlinear relation between the main design parameters h and ψ. For stainless steel fingers, thickness values exhibit minimal change with varying enclosing angles, while for PLA, the effect is more pronounced. Engineers can select the value of the most crucial design parameter at the limit, determining the value for the other design parameter accordingly. Additionally, the chart helps the engineer to decide which material would fit the best to the desired design.

However, improvements to obtain better results can be made, as the result of the parametric sweep can be more accurate and smooth if the range of interest for the swept parameters is determined, such that a more local study could be done. While linear interpolation is currently used to find intersection points between maximum force plots and the force limit, it introduces some deviations.
Lastly, the assumption was made that the intersection points could be fitted by a 3rd-degree polynomial for the thickness-enclosing angle plot. This is chosen based on the trend that was observed in the intersection points. However, this polynomial fitting is only an approximation of the actual trend. Other polynomial fitting methods could be studied and used to increase the accuracy of this approximation, such as higher-order polynomial fitting.

8.3. Extendability of the method

The model could be extended such that more complex designs could be studied. In this thesis the method is applied for a single initially-curved beam with a rectangular solid cross-sectional area, that functions in an environment with solid, rigid spherical objects.
The method could be extended on the one hand at the object-oriented side of the model and on the other hand on the initially-curved side of the model.

8.3.1. Extendability on the initially-curved finger

More complex designs of the gripper finger can be made while using the developed model. One example of a more complex design rises when the implementation of a sleeve on the gripper is done.
For the sleeve to function well it is necessary to have two backbones that are connected at the tip, while one backbone is free to move. A schematic of this idea is given in Figure 8.2. Here R_o is the radius of the outer backbone, R_i is the radius of the inner backbone, L_o is the arc length of the outer backbone and L_i is the arc length of the inner backbone. The backbones are distanced a thickness t from each other. The stiffness of the joints $K_{\theta 2}$, $K_{\theta 3}$ and $K_{\theta 4}$ are the combined stiffness of each joint for both the inner and outer backbone, where $K_\theta^o i$ is the stiffness for the joints of the outer backbone and $K_\theta^i i$, for $i = 2, 3, 4$.

For the backbone with the outer radius R_o the regular script of the model, as described in chapter 4, can executed. This will result in the kinematics and kinetics of the outer backbone. The kinematics of the outer backbone are related to the inner backbone, due to the connected fingertip. Due to the slider connection at the base of the inner fingertip, the length of the inner backbone will vary as the mechanism is deformed. By determining the length of the inner backbone over the deformation the stiffness of the inner backbone can be determined, By adding the stiffness of the inner to the stiffness of the outer backbone, the combined stiffness is determined. With this combined stiffness then the kinetics of the complex mechanism can be determined and the pull-out force can be plotted and used for a parametric study in the same way as described in chapter 6. A detailed description and elaboration of this extended application can be found in Appendix I.

8.3.2. Extendability on the object

The object that was used in this thesis was a rigid sphere, which is the most basic form to model, as the radius of the object is constant over the entire geometry.
However, when the model is preferred to be applied to design grippers for non-circular objects the model could also be used. In this case, the fifth link, which in this model represented the distance from

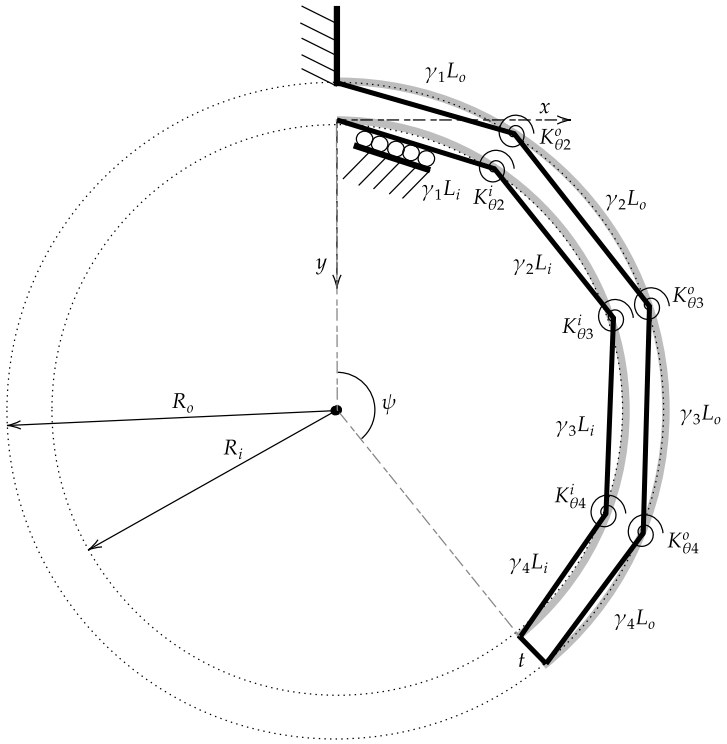

Figure 8.2: Extension of the model for a complex finger design: a gripper with an interconnected double backbone configuration, where t is the distance between the backbones, R_i is the inner radius of the finger and R_o is the outer radius of the finger. The inner backbone can elongate, due to the slider connection at the base.

the center of the object to the tip of the mechanism, can be considered a link with a variable length instead of a constant length. The length of the fifth link could be a function of the surface geometry of the object.
This model can also be extended such that compliant objects can be modeled. This can be accomplished by making the fifth link a variable in the length and adding a spring in the direction of the link, which represents the stiffness of the object. This is, in essence, a Pseudo-Rigid approach for modeling the compliant object.

8.4. Recommendations for future research

In this thesis, the research is done within a defined scope. Where at first a broad study is done about gripper and sleeve literature, as described in chapter 2, a main focus was chosen to study the extendability of the PRB methodology and study relevant design parameters.
To extend this research there are several topics that could be interesting to address in future research.

First, the model in this research only simulated the pull-out force in a single direction, where the mechanism was in static balance and frictionless. In reality, for instance, when grippers are designed, there could be misalignments or different grasping directions and external loads, due to the environment, which leads to a pull-out direction that is not in line with gravity and moments could arise due to the different grasping directions and there could be friction on the object and finger. By adding friction to the object and the finger and placing the base of the fifth link on a planar joint instead of a linear slider a more realistic force development graph could be generated where the object can move in both the x- and y-direction.

Furthermore, when a gripper or an object is moved, the dynamics of that motion will also influence the kinetics. For instance, an acceleration of the object in the x-direction would result in a force in that same direction which influences the kinetics. It could be an interesting topic to study the influence of multiple forces on the mechanism, while holding an object and therefore include the dynamics of the system.

However, this adds complexity as in this case the force distribution and deformation in a multi-finger gripper is different for each finger when for instance the gripper is accelerated in the x-direction.

Moreover, the parametric study in this paper is evaluated primarily for the thickness and enclosing angle of a gripper finger, for two different materials. However, this could be evaluated for other design parameters, such as multiple values for the Young's modulus for different materials, different cross-sections of the finger, resulting in a different area moment of inertia, different widths of the finger, and different object dimensions and weight. The focus of the design parameters that are used in the parametric study can therefore shift according to the main parameters of interest.

Lastly, in chapter 2 a review is given about gripper and sleeve design. In this thesis, the implementation of the sleeve was out of the scope for this thesis, due to the limited time in which this project could be conducted. It could be interesting to study how well the sleeve would function at certain enclosing angles and how much influence the sleeve mechanics have on the kinematics and kinetics of the modeled initially-curved mechanism.

9

Application

In chapter 6 the methodology of the parametric study is described. In this chapter, the application of the model and the parametric study is given in a concrete design. In this chapter, a load case is described that gives requirements for the design. The parametric study is used to make design choices for a final gripper design. The final design is described and shown in this chapter.

9.1. Load case

The requirements of the design are set due to the load case that is chosen. The application of this gripper is in the agri-food gripper technology in which fragile, spherical objects have to be grasped in cluttered environments. The case that is set for this design is therefore:

1. The gripper has to be able to grasp a tomato in cluttered environments, such as a box or a pile of tomatoes or a tomato plant in which it encounters the environment of the plant. Therefore the gripper has to be thin and slim in width.
2. The gripper has to facilitate the use of a belt or a sleeve to create a zero-slip surface, such that damage caused by traction is minimized. Therefore, an inner and outer finger backbone has to be designed.
3. The gripper has to be able to hold the weight of a tomato. The weight of a tomato is chosen to be 100 g for this design case.
4. Geometrically the gripper has to be able to hold the tomato. The tomato is therefore assumed to be a sphere with a radius of 30 mm and three fingers are required to prevent the tomato from slipping out of the finger. The total number of backbones, n_b, is therefore six.

To fulfill these requirements the design parameters are as shown in Table 9.1, where the material of the fingers is chosen to be a leaf spring from 1.4310 stainless steel. This has the advantage of having a high stiffness for thin fingers, such that at a low thickness the fingers still can hold a relatively sufficient amount of weight. This can be concluded from Figure 7.5 in chapter 7. Also, because it is made of a leaf spring, the elastic limit is high, and therefore the deformation that occurs on the finger when retracting would not lead to plastic deformation.

9.2. Parametric study evaluation

In chapter 6 a description is given about the methodology of the parametric sweep and how this results in usable plots that help to make design choices. In chapter 7 the main results of this parametric study are described. In the previous section the known parameters, due to a chosen load case, were described. In this section the choices for the unknown parameters, which are the design parameters are described. These choices were made by using the parametric study as a scientific foundation.

9.2.1. Design choices based on parametric study

As described in chapter 6 a parametric sweep of the main design parameters h, ψ, and E is done. The first choice that is made is the choice of the preferred material type. In the load case requirements were stated about the thickness and width of the gripper finger. These should be small, due to the cluttered environment in which the gripper has to function. From Figure 7.5 in chapter 7 can be concluded that for a stainless steel finger, the thickness of the finger can be smaller at the same load. Another advantage of using a stainless steel leaf spring is that, due to the properties of a leaf spring, the elastic limit is relatively high and therefore it is suitable for retracting a finger in a small enclosure because the deformation that occurs in that retracting phase would not be plastic. For these reasons, the chosen material type for the design of the finger is 1.4310 stainless steel.
The result in Figure 7.5 only shows the relation between the enclosing angle and the finger thickness for a width of 20 mm. To make geometrical design choices the parametric sweep is also done for a 10 mm width and a 15 mm width. The combined result can be found in Figure 9.1. In this plot, the circles represent the intersection between the force limit, which is in this case equal to the gravitational weight of the tomato divided by the number of backbones, as given in Equation 9.1. As the number of backbones in three fingers is six, the weight is therefore also for each backbone a sixth of the total weight of the tomato.

$$F_z = \frac{mg}{n_b} \tag{9.1}$$

In Figure 9.1 it is visible that the thickness of a single backbone can be small. In design projects, design choices are also made based on available resources. In the case of this prototype design at the university only at the moment a 0.25 mm thick stainless steel leaf spring was available, which resulted in choosing this type of leaf spring for the design. As can be seen in Figure 9.1 for this thickness the gripper can hold a 100 g tomato for a lot of combinations of the preferred enclosing angle and width. Due to the requirement of a design that is able to function in a cluttered environment, it is chosen to design a gripper finger with a width of 10 mm and should therefore hold a tomato of 100 g when the finger is enclosed approximately 145 degrees around the object, which makes it also suitable for using a sleeve as the sleeve has a low curvature it has to overcome, which means that the tension in the sleeve material is kept relatively low, compared to a finger that has to make a full 180-degree enclosure.

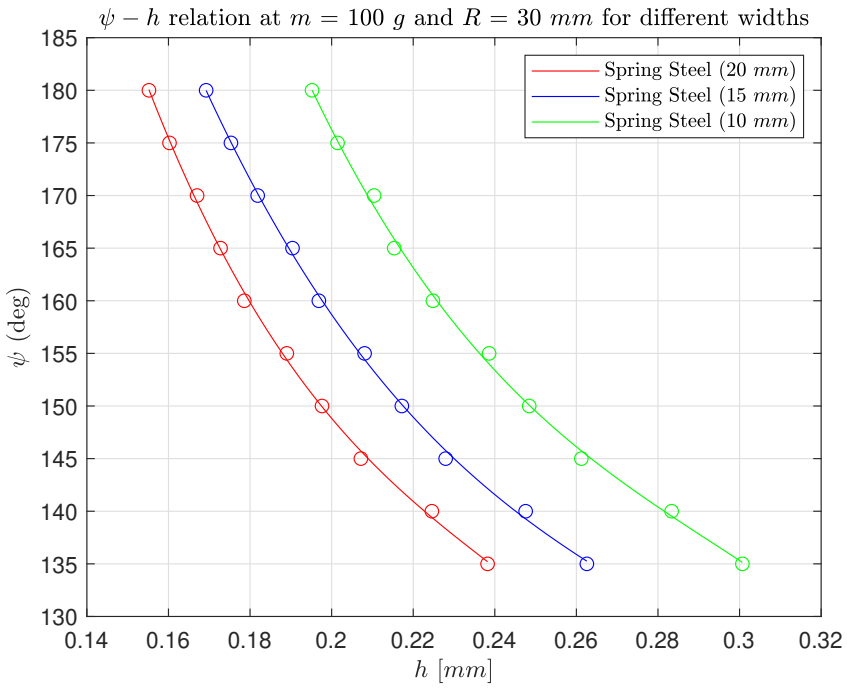

Figure 9.1: Design chart for widths of the finger, w, of 10, 15 and 20 mm when the material is stainless steel.

An overview of the used design values is given in Table 9.1.

Table 9.1: Parameter values that are used for the final design

Parameter	Value	Unit	Description
R	30	$[mm]$	The radius of the tomato and therefore also the radius of the gripper curvature.
m	100	$[g]$	The mass of a tomato.
g	9.81	$[m/s^2]$	The gravitational constant.
n_b	6	$[-]$	Number of backbones.
E	195	$[GPa]$	Young's modulus of 1.4310 stainless steel.
ψ	180	$[°]$	Enclosing angle.
h	0.25	$[mm]$	Thickness of a single backbone.
w	10	$[mm]$	Width of a gripper finger.

9.3. Final design

9.3.1. Solidworks

The final design of the gripper finger consists of an inner backbone (1) and outer backbone (2), such that a belt or sleeve can be used. The backbones are made of a stainless steel 1.4310 leaf spring. These backbones are housed in a 3D-printed PLA guiding hub (3). When the backbones are located at inside the hub, the hub is closed off with a 3D-printed PLA plate (4). The backbones are mounted to the triangular mounting hub (5), which facilitates the connection of three gripper fingers to one motion stage. Further detailed drawings of the part can be found in Appendix J.

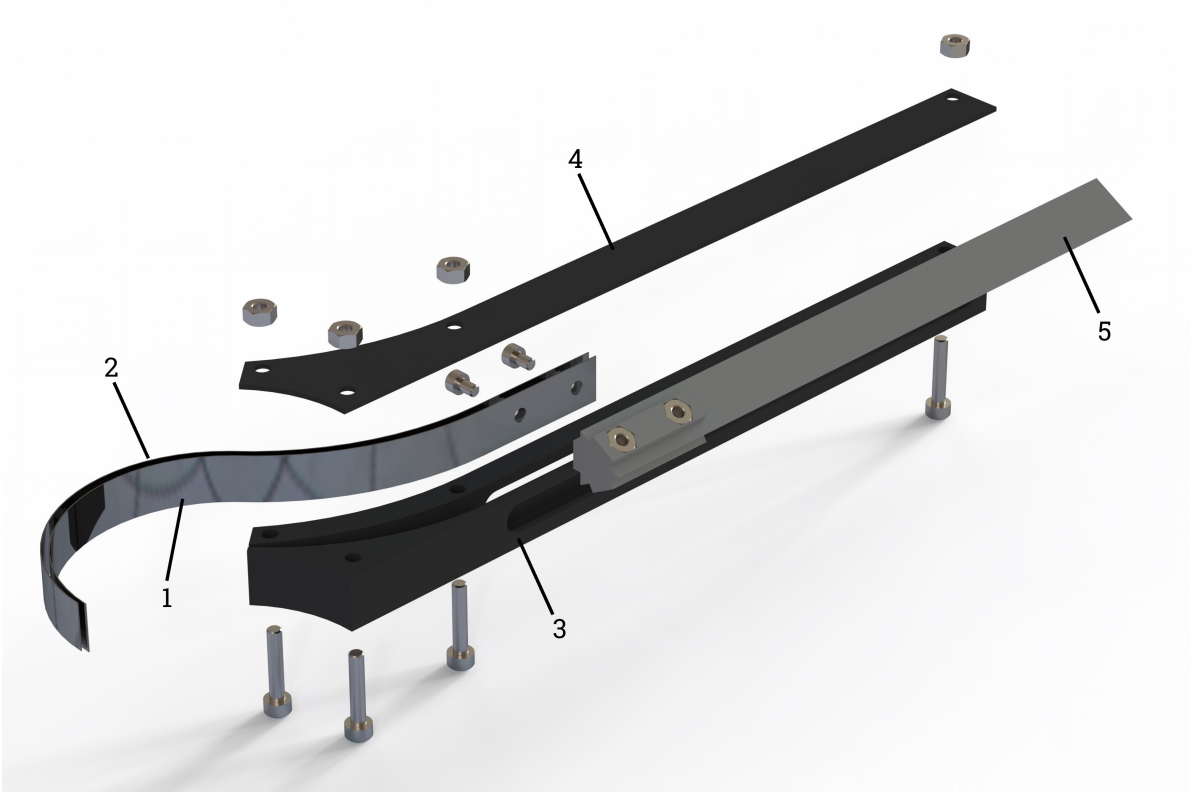

Figure 9.2: An exploded view of the design of a single finger with the triangular mounting part: the design consists of an inner backbone (1) and outer backbone (2), housed in a 3D-printed PLA guiding hub (3) that is closed of with a plate (4). The backbones are mounting to the triangular mounting hub (5).

9.3.2. Manufacturing

The finger backbones are laser cut from a stainless steel (1.4310) leaf spring of a width of 50 mm. The lengths of the cut parts were 650 mm, such that there was enough length to clamp it inside the curving setup, which was used to apply the desired curvature to the leaf springs. When the preferred curvature was made, the parts of the leaf spring that were not part of the final finger were cut off with a plate cutter. The dimensions of the lasercutted leaf springs can be found in the drawing that is depicted in Figure J.1 in Appendix J. The location where the leaf springs have to be cut with the plate cutter is not exactly determined. This is done by trial and error, such that all fingers are correctly connected to the triangle part in the design. In the lasercutted leaf spring, eight holes are cut, through with bolts the backbones can be connected to the triangular moving part. At least two holes need to be left, such that a rigid connection can be made.

The hull from which the stainless steel backbones are retracted and extracted is 3D printed from PLA material. Furthermore, the plate that fits on top of the hull is 3D printed from PLA and can be closed by connecting the hull and the plate with M3 bolts and nuts additionally, the plate is glued on top of the hull when the backbones are located inside the hull. This is done with regular super glue, such that the small section of the hull also has a connection to the top plate which creates a more rigid construction of the overall hull design. The dimensions of the hull and the plate can be found in Figure J.2 and Figure J.3 in Appendix J. Furthermore, the connection parts that are used to connect the three finger hulls together are also 3D printed from PLA. The dimensions of this part can be found in Figure J.4 in Appendix J.

The triangular connection part, which facilitates the movement of the compliant backbones is also 3D printed from PLA. Inside the hexagonal-shaped holes, M3 nuts were glued with regular superglue, such that an easy, but rigid connection can be made between the backbone and the triangular connection part. The dimensions of this part can be found in Figure J.5 in Appendix J.

9.3.3. Final prototype

The final prototype of the gripper, when fully manufactured and assembled, is shown in Figure 9.3. The gripper functions as desired and is able to grasp a tomato with a mass of 100 g. The gripper when it is retracted can be seen in Figure 9.3a and when it is extracted can be seen in Figure 9.3b.

A picture of the prototype grasping a tomato with approximately a diameter of 57 mm and a mass of 97 g is depicted in Figure 9.4, showing that with the design chart a reliable gripper can be designed, that is able to grasp the payload that is used in the parametric study.

(a) The prototype when the finger is retracted.

(b) The prototype when the finger is extracted.

Figure 9.3: A picture of the final prototype in retracted and extracted configuration.

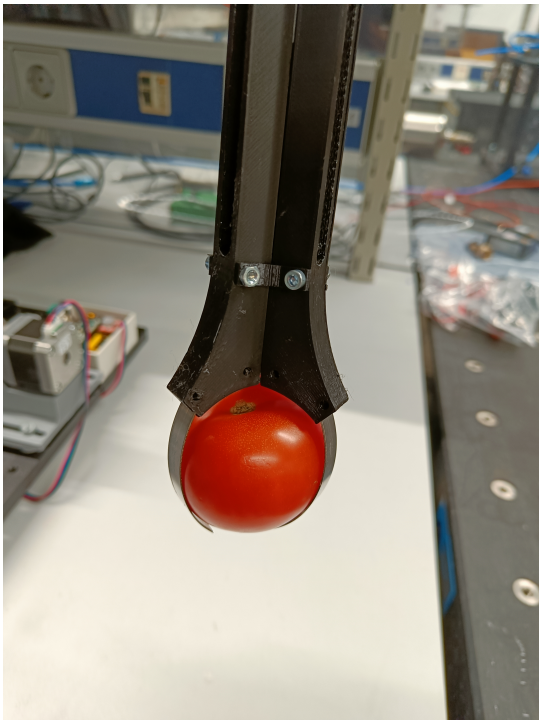

Figure 9.4: A picture of the prototype grasping a tomato with approximately a diameter of 57 mm and a mass of 97 g.

10

Conclusion

In this thesis, the modelling methodology for initially-curved gripper fingers is investigated. Through a literature study, the existing gripper types and methods are analyzed, such that an improved gripper that functions in cluttered and fragile environments could be designed. This literature gave insight into the challenging parameters when designing such a gripper. The literature study led to the main research question:

How can in a structured way knowledge be gained about the relation between important design parameters, such as thickness and enclosing angle, for a certain case study, with the help of a model-based approach?

This research question is answered by defining the project in two main sections, which are the determination of the pull-out force and the parametric study.

First, by using an existing Pseudo-Rigid Body model for initially-curved beams as the foundation and adding an extra link to mimic the extraction of an object from initially curved gripper fingers, the pull-out force of an object being extracted from such fingers is determined to give insight into the payload of a gripper for a defined load case. This load case was defined based on the dimensions and weight of a regular tomato. The determination of the pull-out force is validated by designing a test setup by which the reaction forces at the base of an initially-curved testpiece in the x- and y-direction are measured, while an object, as a disk, is extracted in the y-direction. This is done for multiple testpieces, one of PLA and one of stainless steel. The results showed a similar trend in the force-deflection graph between the simulated and experimental results with an error of the maximum force values of approximately 18 $\%$ for the reaction force in the y-directions for both the PLA and stainless steel testpiece, and an error of approximately 12 $\%$ for the reaction force in the x-direction for the PLA testpiece and approximately 32 $\%$ for the stainless steel testpiece.

Secondly, the developed model is used to do a parametric study, where for multiple array values of the enclosing angle ψ, and thickness h a parametric sweep is done. By determining the intersection points of the plots, where the maximum pull-out force is related to the thickness for different enclosing angles, and the force limit, which is determined by a load case where a gripper of the fingers holds a tomato of 100 g, the relation between the design parameters h and ψ are determined and depicted in a plot.

With this result, the main research question is answered, as the relation between the important design parameters is determined with a model-based approach. Therefore, the results of this thesis provide valuable design charts to help and inspire engineers in designing innovative compliant grippers.

Bibliography

[1] Taqi Abrar et al. “Highly Manoeuvrable Eversion Robot Based on Fusion of Function with Structure”. In: Feb. 2021. DOI: 10.1109/ICRA48506.2021.9561873.

[2] *Best Soft Gripper Manufacturer in 2023 - SoftGripping*. en-US. Running Time: 270. Apr. 2020. URL: https://soft-gripping.com/.

[3] Laura H. Blumenschein et al. “Design, Modeling, Control, and Application of Everting Vine Robots”. In: *Frontiers in Robotics and AI* 7 (2020). ISSN: 2296-9144. URL: https://www.frontiersin.org/articles/10.3389/frobt.2020.548266.

[4] Joran W. Booth et al. “OmniSkins: Robotic skins that turn inanimate objects into multifunctional robots”. In: *Science Robotics* 3.22 (Sept. 2018). Publisher: American Association for the Advancement of Science, eaat1853. DOI: 10.1126/scirobotics.aat1853. URL: https://www.science.org/doi/10.1126/scirobotics.aat1853.

[5] John J Craig. “Mechanics and Control Third Edition”. In: ().

[6] Mohammad H Dado. “Variable parametric pseudo-rigid-body model for large-deflection beams with end loads”. In: *International Journal of Non-Linear Mechanics* 36.7 (Oct. 2001), pp. 1123–1133. ISSN: 0020-7462. DOI: 10.1016/S0020-7462(00)00076-7. URL: https://www.sciencedirect.com/science/article/pii/S0020746200000767 (visited on 01/23/2024).

[7] Steve Davis et al. “Robot prototyping in the design of food processing machinery”. In: *Industrial Robot: An International Journal* 34.2 (Jan. 2007). Ed. by Osman Tokhi. Publisher: Emerald Group Publishing Limited, pp. 135–141. ISSN: 0143-991X. DOI: 10.1108/01439910710727487. URL: https://doi.org/10.1108/01439910710727487.

[8] N. Elango, Nneka Obianuju Onubogu, and S. Ragunathan. “Experimental Study of Non-Contact Robot Gripper for Food Industries”. en. In: *Applied Mechanics and Materials* 232 (2012). Conference Name: Mechanical and Aerospace Engineering, ICMAE2012 ISBN: 9783037855140 Publisher: Trans Tech Publications Ltd, pp. 392–397. ISSN: 1662-7482. DOI: 10.4028/www.scientific.net/AMM.232.392. URL: https://www.scientific.net/AMM.232.392.

[9] Yahya Elsayed et al. “Crimped braided sleeves for soft, actuating arm in robotic abdominal surgery”. In: *Minimally Invasive Therapy & Allied Technologies* 24.4 (July 2015). Publisher: Taylor & Francis _eprint: https://doi.org/10.3109/13645706.2015.1012083, pp. 204–210. ISSN: 1364-5706. DOI: 10.3109/13645706.2015.1012083. URL: https://doi.org/10.3109/13645706.2015.1012083.

[10] Gualtiero Fantoni. “Grasping Everything”. In: Nov. 2013. DOI: 10.13140/2.1.3351.4885.

[11] *FlexCRAFT*. nl-NL. URL: https://www.tudelft.nl/agtech/projects/flexcraft.

[12] Bart Friederich. *Design and Validation of a Manoeuvering Caging Gripper for Cluttered Environments | TU Delft Repositories — resolver.tudelft.nl*. http://resolver.tudelft.nl/uuid:f20e97b0-97a4-43b7-91ec-1acb3bca72ac. [Accessed 05-02-2024]. 2022.

[13] Tatsuhiro Hiramitsu et al. “Experimental Evaluation of Textile Mechanisms Made of Artificial Muscles”. In: *2019 2nd IEEE International Conference on Soft Robotics (RoboSoft)*. Apr. 2019, pp. 1–6. DOI: 10.1109/ROBOSOFT.2019.8722802.

[14] *How Smart Farming Is Transforming Agriculture*. en-US. URL: https://www.meilirobots.com/resources-list/smart-farming-guide.

[15] Venkatasubramanian Kalpathy Venkiteswaran and Hai-Jun Su. “A Versatile 3R Pseudo-Rigid-Body Model for Initially-Curved and Straight Compliant Beams of Uniform Cross-Section”. In: *Journal of Mechanical Design* 140 (June 2018). DOI: 10.1115/1.4040628.

[16] Jamie Luong et al. “Eversion and Retraction of a Soft Robot Towards the Exploration of Coral Reefs”. In: *2019 2nd IEEE International Conference on Soft Robotics (RoboSoft)*. Apr. 2019, pp. 801–807. DOI: 10.1109/ROBOSOFT.2019.8722730.

[17] Yui Makiyama, Zhongkui Wang, and Shinichi Hirai. “A Pneumatic Needle Gripper for Handling Shredded Food Products”. In: *2020 IEEE International Conference on Real-time Computing and Robotics (RCAR)*. Sept. 2020, pp. 183–187. DOI: 10.1109/RCAR49640.2020.9303279.

[18] Nicolas Mouazé and Lionel Birglen. “Bistable compliant underactuated gripper for the gentle grasp of soft objects”. en. In: *Mechanism and Machine Theory* 170 (Apr. 2022), p. 104676. ISSN: 0094-114X. DOI: 10.1016/j.mechmachtheory.2021.104676. URL: https://www.sciencedirect.com/science/article/pii/S0094114X21004067.

[19] *MultiChoiceGripper | Festo USA*. URL: https://www.festo.com/us/en/e/about-festo/research-and-development/bionic-learning-network/highlights-from-2013-to-2014/multichoicegripper-id_33524/.

[20] Atsuo Orita and Mark. R. Cutkosky. “Scalable Electroactive Polymer for Variable Stiffness Suspensions”. In: *IEEE/ASME Transactions on Mechatronics* 21.6 (Dec. 2016). Conference Name: IEEE/ASME Transactions on Mechatronics, pp. 2836–2846. ISSN: 1941-014X. DOI: 10.1109/TMECH.2016.2586484.

[21] Phuoc Thien Phan et al. “Smart textiles using fluid-driven artificial muscle fibers”. en. In: *Scientific Reports* 12.1 (June 2022). Number: 1 Publisher: Nature Publishing Group, p. 11067. ISSN: 2045-2322. DOI: 10.1038/s41598-022-15369-2. URL: https://www.nature.com/articles/s41598-022-15369-2.

[22] Panagiotis Polygerinos et al. “Soft robotic glove for combined assistance and at-home rehabilitation”. en. In: *Robotics and Autonomous Systems*. Wearable Robotics 73 (Nov. 2015), pp. 135–143. ISSN: 0921-8890. DOI: 10.1016/j.robot.2014.08.014. URL: https://www.sciencedirect.com/science/article/pii/S0921889014001729.

[23] *Pre-Formed Vine Robot*. en. May 2018. URL: https://www.vinerobots.org/build-one/pre-formed-vine-robot/.

[24] Pierluigi Rea. *On the Design of Underactuated Finger Mechanisms for Robotic Hands*. en. Publication Title: Advances in Mechatronics. IntechOpen, Aug. 2011. ISBN: 978-953-307-373-6. DOI: 10.5772/24304. URL: https://www.intechopen.com/chapters/18894 (visited on 02/14/2023).

[25] roboapp. *Meat Gripper*. en-US. URL: https://www.appliedrobotics.com/products/automation/grippers/meat-gripper/.

[26] *SensorX Fish X-ray bone detection | Marel*. en. URL: https://marel.com/en/products/sensorx-fish.

[27] *SWITL*. URL: https://www.furukawakikou.co.jp/switl/.

[28] University of Minnesota Wearable Technology Lab. *Active Auxetic Fabrics for Self-Fitting Clothing*. Jan. 2020. URL: https://www.youtube.com/watch?v=PttK2Z-LJ2M.

[29] Venkatasubramanian Kalpathy Venkiteswaran and Hai-Jun Su. “A Versatile 3R Pseudo-Rigid-Body Model for Initially Curved and Straight Compliant Beams of Uniform Cross Section”. en. In: *Journal of Mechanical Design* 140.9 (Sept. 2018), p. 092305. ISSN: 1050-0472, 1528-9001. DOI: 10.1115/1.4040628. URL: https://asmedigitalcollection.asme.org/mechanicaldesign/article/doi/10.1115/1.4040628/473029/A-Versatile-3R-PseudoRigidBody-Model-for-Initially (visited on 09/06/2023).

[30] Venkatasubramanian Kalpathy Venkiteswaran and Hai-Jun Su. “Pseudo-rigid-body models for circular beams under combined tip loads”. In: *Mechanism and Machine Theory* 106 (Dec. 2016), pp. 80–93. ISSN: 0094-114X. DOI: 10.1016/j.mechmachtheory.2016.08.011. URL: https://www.sciencedirect.com/science/article/pii/S0094114X16301847 (visited on 01/23/2024).

[31] *Ventose - Vuototecnica 2023*. URL: https://www.vuototecnica.net/products.php?cat=1.

[32] Zhongkui Wang, Shinichi Hirai, and Sadao Kawamura. “Challenges and Opportunities in Robotic Food Handling: A Review”. In: *Frontiers in Robotics and AI* 8 (2022). ISSN: 2296-9144. URL: https://www.frontiersin.org/articles/10.3389/frobt.2021.789107.

[33] Adeel Zulifqar, Tao Hua, and Hong Hu. “Development of uni-stretch woven fabrics with zero and negative Poisson’s ratio”. en. In: *Textile Research Journal* 88.18 (Sept. 2018). Publisher: SAGE Publications Ltd STM, pp. 2076–2092. ISSN: 0040-5175. DOI: 10.1177/0040517517715095. URL: https://doi.org/10.1177/0040517517715095.

A

MATLAB Model Source Code

A.1. Main Model Script

In subsection A.1.1 the main script of the model is described. In this mainscript several subscript are recalled. The code of these subscripts is provided in the remaining subsections of this section of the appendix.

A.1.1. MainScript.m

```
clearvars
close all
clc

%% Choose the thickness (h) and revolution angle (psi) of the finger & load parameters and
    the correct material:
  E = 195E9;                % Pa (Spring Steel)
% E = 2.55E9;               % Pa (PLA)
h =  0.3/1000; % m
psi = deg2rad(180); % deg
MainParameters;             % Load in the main mechanism/environment parameters
PRBMParameters;             % Load in the parameters from the 3R PRBM method

%% Plot initial vector loop
VectorLoopValues;

%% Optimization problem
nms = 3;

dy = 0.001;
y_start = 0;
y_end = 2*R;
y = y_start:dy:y_end;

dtheta = deg2rad([0 0 0 0 0 0]);
dtheta1 = dtheta(1);
dtheta2 = dtheta(2);
dtheta3 = dtheta(3);
dtheta4 = dtheta(4);
dtheta5 = dtheta(5);
dtheta6 = dtheta(6);

for i = 1:length(y)
    % Initial values
    x0 = [dtheta2 dtheta5];
    x0_i(:,i) = x0
    dtheta34_0 = [dtheta3 dtheta4];
    dtheta34_0i(:,i) = dtheta34_0
    % lb = x0+deg2rad([-2 -5]);
    % ub = x0+deg2rad([2 5]);
    lb = x0 + 1000*dy*deg2rad([-2 -15]);
```

```
    ub = x0 + 1000*dy*deg2rad([2 15]);
    L6 = R+y(i);
    L6_i(i) = L6;

    % Find min PE
    objective = @(x)ObjPE2 (x,dtheta34_0,theta_0,L1,L2,L3,L4,L5,L6,K_theta2,K_theta3,K_theta4
        );

    % MultiStart Optimizer:
    ms = MultiStart('Display','off');
    options=optimset('Algorithm','interior-point','GradObj','off','Hessian','off','tolX',1e
        -10,'TolFun',1e-10,'MaxIter',100,'MaxFunEvals',10000);
    problem = createOptimProblem('fmincon','x0',x0,'lb',lb,'ub',ub,'Aeq',[],'beq',[],'nonlcon
        ',[],'objective',objective,'options',options);
    [x,fval,exitflag,output,solutions] = run(ms,problem,nms);

    dtheta2 = x(1);
    dtheta5 = x(2);

    % calculate mechanism angles
    fun = @(dtheta34)vectorloopequation2(dtheta34,dtheta2,dtheta5,theta_0,L1,L2,L3,L4,L5,L6);

    [dtheta34] = fsolve(fun,dtheta34_0);
    dtheta3 = dtheta34(1);
    dtheta4 = dtheta34(2);

    DataStorage;
end

%% Plotting angles
figure('Name','Angles')
plot(Data(:,7),Data(:,1))
hold on
plot(Data(:,7),Data(:,2))
plot(Data(:,7),Data(:,3))
plot(Data(:,7),Data(:,4))
plot(Data(:,7),Data(:,5))
plot(Data(:,7),Data(:,6))
hold off
xlabel('L6 (m)'), ylabel('\theta (deg)')
title('d\theta')
legend('\delta\theta_1', '\delta\theta_2', '\delta\theta_3', '\delta\theta_4', '\delta\
    theta_5', '\delta\theta_6')

%% Positions
theta1 = zeta_1;
theta2 = zeta_1+zeta_2+deg2rad(Data(:,2));
theta3 = zeta_1+zeta_2+zeta_3+deg2rad(Data(:,2)+Data(:,3));
theta4 = zeta_1+zeta_2+zeta_3+zeta_4+deg2rad(Data(:,2)+Data(:,3)+Data(:,4));

origin = zeros(length(Data(:,1)),2);
r1 = ones(length(Data(:,1)),1).*gamma_1*L*[cos(theta1) sin(theta1)]
r2 = gamma_2*L*[cos(theta2) sin(theta2)]
r3 = gamma_3*L*[cos(theta3) sin(theta3)]
r4 = gamma_4*L*[cos(theta4) sin(theta4)]

Xtot = r1(:,1)+r2(:,1)+r3(:,1)+r4(:,1)
Ytot = r1(:,2)+r2(:,2)+r3(:,2)+r4(:,2)

%% Jacobian calculation
syms dt2 dt3 dt4

t1 = zeta_1;
t2 = zeta_1+zeta_2+dt2;
t3 = zeta_1+zeta_2+zeta_3+dt2+dt3;
t4 = zeta_1+zeta_2+zeta_3+zeta_4+dt2+dt3+dt4;

Xtip = L*(gamma_1*cos(t1)+gamma_2*cos(t2)+gamma_3*cos(t3)+gamma_4*cos(t4))
Ytip = L*(gamma_1*sin(t1)+gamma_2*sin(t2)+gamma_3*sin(t3)+gamma_4*sin(t4))
thetatip = psi+dt2+dt3+dt4

```

```
J = jacobian([Xtip, Ytip, thetatip],[dt2,dt3,dt4] );

for k = 1:length(Data(:,1))
Jsub= subs(J,{dt2 dt3 dt4},{deg2rad(Data(k,2)) deg2rad(Data(k,3)) deg2rad(Data(k,4))})
tau = [K_theta2.*deg2rad(Data(k,2)); K_theta3.*deg2rad(Data(k,3)); K_theta4.*deg2rad(Data(k
    ,4))]
W(:,k) = inv(transpose(Jsub))*tau
end

%% Forces calculated by Jacobian method
Fx2 = W(1,:);
Fy2 = W(2,:);
Ftot2 = sqrt(Fx2.^2+Fy2.^2);

%% Forces calculated by fourth rigid beam (gamma_4*L)
omega = theta_0(5)+deg2rad(Data(:,5))
omega3 = deg2rad(180)-(zeta_1+zeta_2+zeta_3+zeta_4+deg2rad(Data(:,2)+Data(:,3)+Data(:,4)))

T2 = K_theta2.*deg2rad(Data(:,2))
T3 = K_theta3.*deg2rad(Data(:,3))
T4 = K_theta4.*deg2rad(Data(:,4))

X = L*gamma_4*cos(omega3)
Y = L*gamma_4*sin(omega3)

F = T4./(-Y.*cos(omega)-X.*sin(omega))
Fx = F.*cos(omega)
Fy = F.*sin(omega)
Ftot = sqrt(Fx.^2+Fy.^2);

%%
figure()
plot(Data(:,8)-1000*R,Fy, 'r')
% hold on
% plot(Data(:,8)-1000*R,Fx, 'b')
% plot(Data(:,8)-1000*R,Ftot, 'g')
% plot(Data(:,8)-1000*R,Fy2, 'r')
hold on
plot(Data(:,8)-1000*R,Fx2, 'b')
% plot(Data(:,8)-1000*R,Ftot2, 'g')
% % plot(Data(:,8)-1000*R,Fy3, 'r')
% hold on
% plot(Data(:,8)-1000*R,Fx3, 'b')
legend("F_y",'F_x', 'Location','northeastoutside')
xlabel('Displacement y [mm]'), ylabel('Force [N]')
ylim([0 3])
grid on
title('PLA - h = 2mm, R = 40 mm, $\psi$ = 180 deg','Interpreter','latex')
title('Stainless Steel - h = 0.3 mm, R = 40 mm, $\psi$ = 180 deg','Interpreter','latex')

%% Test results leafspring: 0.3 mm
 TestResultsLeafSpring2;

%% Test Results PLA: 2mm (11-12-2023)
 TestResultsPLA_11_12_2023_2mm;

%% Visualisation
VisualPlotResult;
```

In the Main Script several subscripts are used, which are found below.

A.1.2. MainParameters.m

```
% Beam - Material choice: PLA
w = 50/1000;                    % m
I = w*h.^3/12;                  % m^4 --> design freedom

% Tomato parameters and force due to the weight of tomato.
D_tomato = 0.08; % m
R = D_tomato/2;
L = psi*R ;
```

A.1.3. PRBMParameters.m

```
% Load in the Table with the parameters from the 3R paper (Venkiteswaran)
load("Table.mat");

% Table
% Find the row index that corresponds to the closest angle to psi
[~, row] = min(abs(Table(:,1) - rad2deg(psi)));

% Extract the desired values from the table
zeta_1 = Table(row, 2);
gamma_1 = Table(row, 3);
k_theta2 = Table(row, 4);
k_theta3 = Table(row, 5);

% Other value definitions
zeta_2 = psi/4;
zeta_3 = psi/2-2*zeta_1;
gamma_2 = (2/psi)*sin(psi/4-zeta_1);

% Definitions due to symmetry in the PRBM model
k_theta4 = k_theta2;
gamma_4 = gamma_1;
gamma_3 = gamma_2;
zeta_4 = zeta_2;

% Stiffness values
K_theta2 = k_theta2*E*I/L;
K_theta3 = k_theta3*E*I/L;
K_theta4 = k_theta4*E*I/L;
```

Here the loaded table 'Table.mat' is the table as depicted in Table 4.1.

A.1.4. VectorLoopValues.m

```
% Initial positions
theta1_0 = zeta_1;
theta2_0 = zeta_1+zeta_2;
theta3_0 = zeta_1+zeta_2+zeta_3;
theta4_0 = zeta_1+zeta_2+zeta_3+zeta_4;
theta_tip_0 = psi;
theta5_0 = theta_tip_0-deg2rad(90);
theta6_0 = deg2rad(90);

theta_0 = [theta1_0 theta2_0 theta3_0 theta4_0 theta5_0 theta6_0];

% Vector lengths
L1 = gamma_1*L;
L2 = gamma_2*L;
L3 = gamma_3*L;
L4 = gamma_4*L;
L5 = R;
L6_0 = R;

% Plot initial vector loop
origin = [0;0];
r1_0 = [L1*cos(theta1_0); L1*sin(theta1_0)];
r2_0 = [L2*cos(theta2_0); L2*sin(theta2_0)];
r3_0 = [L3*cos(theta3_0); L3*sin(theta3_0)];
r4_0 = [L4*cos(theta4_0); L4*sin(theta4_0)];
r5_0 = [L5*cos(theta5_0); L5*sin(theta5_0)];
r6_0 = [L6_0*cos(theta6_0); L6_0*sin(theta6_0)];

alpha  = linspace(0,360,361)           ;
Circle_x     = R*cosd(alpha)   ;
Circle_y0     = R*sind(alpha) + L6_0 ;

loop_ccw = [origin r1_0 r1_0+r2_0 r1_0+r2_0+r3_0 r1_0+r2_0+r3_0+r4_0];
loop_cw = [origin r6_0 r6_0+r5_0];
% figure('Name','Initial Vector Loop')
plot(Circle_x, Circle_y0, 'k--')
```

```
hold on
plot(loop_ccw(1,:),loop_ccw(2,:), 'r')
plot(loop_cw(1,:),loop_cw(2,:), 'r')
axis equal
```

A.1.5. ObjPE2.m

```
function pe = ObjPE2(x,dtheta34_0,theta_0,L1,L2,L3,L4,L5,L6,K_theta2,K_theta3,K_theta4)

% Objective variable: theta_5
dtheta2 = x(1);
dtheta5 = x(2);

% kinematic equations
options = optimset('Display','off');
fun2 = @(dtheta34)vectorloopequation2(dtheta34,dtheta2,dtheta5,theta_0,L1,L2,L3,L4,L5,L6);
[dtheta34] = fsolve(fun2,dtheta34_0,options);

dtheta3 = dtheta34(1);
dtheta4 = dtheta34(2);

pe = 0.5*K_theta2*dtheta2^2+0.5*K_theta3*dtheta3^2+0.5*K_theta4*dtheta4^2;
```

A.1.6. vectorloopequation2.m

```
function F = vectorloopequation2(dtheta34,dtheta2,dtheta5,theta_0,L1,L2,L3,L4,L5,L6)
% VECTOR LOOP EQUATION
%   F(1) and F(2) are based on the vector loop.
F(1) = L1*cos(theta_0(1))+L2*cos(theta_0(2)+dtheta2)+L3*cos(theta_0(3)+dtheta2+dtheta34(1))+
    L4*cos(theta_0(4)+dtheta2+dtheta34(1)+dtheta34(2))-L5*cos(theta_0(5)+dtheta5);
F(2) = L1*sin(theta_0(1))+L2*sin(theta_0(2)+dtheta2)+L3*sin(theta_0(3)+dtheta2+dtheta34(1))+
    L4*sin(theta_0(4)+dtheta2+dtheta34(1)+dtheta34(2))-L5*sin(theta_0(5)+dtheta5)-L6;
end
```

A.1.7. DataStorage.m

```
% dtheta
Data(i,1) = rad2deg(dtheta1);
Data(i,2) = rad2deg(x(1));
Data(i,3) = rad2deg(dtheta34(1));
Data(i,4) = rad2deg(dtheta34(2));
Data(i,5) = rad2deg(x(2));
Data(i,6) = rad2deg(dtheta6);

%dy
Data(i,7) = L6;
Data(i,8) = 1000*L6; % scaled dataset
```

A.1.8. TestResultsLeafSpring2.m

```
TestDatax1 = readmatrix("23 12 21 12 37 55 Testx.txt");
TestDatax2 = readmatrix("23 12 21 12 39 33 Testx.txt");
TestDatax3 = readmatrix("23 12 21 12 40 55 Testx.txt");
TestDatax4 = readmatrix("23 12 21 12 42 19 Testx.txt");
TestDatax5 = readmatrix("23 12 21 12 43 56 Testx.txt");
TestDatax6 = readmatrix("23 12 21 12 45 23 Testx.txt");
TestDatax7 = readmatrix("23 12 21 12 46 47 Testx.txt");
TestDatax8 = readmatrix("23 12 21 12 50 29 Testx.txt");
TestDatax9 = readmatrix("23 12 21 12 53 07 Testx.txt");
TestDatax10 = readmatrix("23 12 21 12 54 43 Testx.txt");

TestDatay1 = readmatrix("23 12 21 13 16 29 Testy.txt");
TestDatay2 = readmatrix("23 12 21 13 17 43 Testy.txt");
TestDatay3 = readmatrix("23 12 21 13 18 58 Testy.txt");
TestDatay4 = readmatrix("23 12 21 13 20 13 Testy.txt");
TestDatay5 = readmatrix("23 12 21 13 21 29 Testy.txt");
TestDatay6 = readmatrix("23 12 21 13 22 44 Testy.txt");
TestDatay7 = readmatrix("23 12 21 13 23 57 Testy.txt");
TestDatay8 = readmatrix("23 12 21 13 25 13 Testy.txt");
```

```
TestDataty9 = readmatrix("23 12 21 13 26 49 Testy.txt");
TestDataty10 = readmatrix("23 12 21 13 28 03 Testy.txt");

plot((TestDataty1(1,7)-TestDataty1(:,7)),TestDataty1(:,5)-TestDataty1(1,5),'r.')
hold on
plot((TestDataty2(1,7)-TestDataty2(:,7)),TestDataty2(:,5)-TestDataty2(1,5), 'r.')
plot((TestDataty3(1,7)-TestDataty3(:,7)),TestDataty3(:,5)-TestDataty3(1,5), 'r.')
plot((TestDataty4(1,7)-TestDataty4(:,7)),TestDataty4(:,5)-TestDataty4(1,5), 'r.')
plot((TestDataty5(1,7)-TestDataty5(:,7)),TestDataty5(:,5)-TestDataty5(1,5),'r.')
plot((TestDataty6(1,7)-TestDataty6(:,7)),TestDataty6(:,5)-TestDataty6(1,5), 'r.')
plot((TestDataty7(1,7)-TestDataty7(:,7)),TestDataty7(:,5)-TestDataty7(1,5), 'r.')
plot((TestDataty8(1,7)-TestDataty8(:,7)),TestDataty8(:,5)-TestDataty8(1,5), 'r.')
plot((TestDataty9(1,7)-TestDataty9(:,7)),TestDataty9(:,5)-TestDataty9(1,5), 'r.')
plot((TestDataty10(1,7)-TestDataty10(:,7)),TestDataty10(:,5)-TestDataty10(1,5), 'r.')
plot((TestDatax1(1,7)-TestDatax1(:,7)),TestDatax1(:,6)-TestDatax1(1,6), 'b.')
plot((TestDatax2(1,7)-TestDatax2(:,7)),TestDatax2(:,6)-TestDatax2(1,6), 'b.')
plot((TestDatax3(1,7)-TestDatax3(:,7)),TestDatax3(:,6)-TestDatax3(1,6), 'b.')
plot((TestDatax4(1,7)-TestDatax4(:,7)),TestDatax4(:,6)-TestDatax4(1,6), 'b.')
plot((TestDatax5(1,7)-TestDatax5(:,7)),TestDatax5(:,6)-TestDatax5(1,6), 'b.')
plot((TestDatax6(1,7)-TestDatax6(:,7)),TestDatax6(:,6)-TestDatax6(1,6), 'b.')
plot((TestDatax7(1,7)-TestDatax7(:,7)),TestDatax7(:,6)-TestDatax7(1,6), 'b.')
plot((TestDatax8(1,7)-TestDatax8(:,7)),TestDatax8(:,6)-TestDatax8(1,6), 'b.')
plot((TestDatax9(1,7)-TestDatax9(:,7)),TestDatax9(:,6)-TestDatax9(1,6), 'b.')
plot((TestDatax10(1,7)-TestDatax10(:,7)),TestDatax10(:,6)-TestDatax10(1,6), 'b.')
```

A.1.9. TestResultsPLA.m

```
TestDataty1 = readmatrix("23 12 11 11 54 20 Test1y.txt");
TestDataty2 = readmatrix("23 12 11 11 55 46 Test1y.txt");
TestDataty3 = readmatrix("23 12 11 11 57 12 Test1y.txt");
TestDataty4 = readmatrix("23 12 11 11 58 44 Test1y.txt");
TestDataty5 = readmatrix("23 12 11 12 00 03 Test1y.txt");
TestDataty6 = readmatrix("23 12 11 12 01 26 Test1y.txt");
TestDataty7 = readmatrix("23 12 11 12 02 47 Test1y.txt");
TestDataty8 = readmatrix("23 12 11 12 04 06 Test1y.txt");
TestDataty9 = readmatrix("23 12 11 12 05 40 Test1y.txt");
TestDataty10 = readmatrix("23 12 11 12 07 09 Test1y.txt");

TestDatax1 = readmatrix("23 12 11 13 44 50 Test1x.txt");
TestDatax2 = readmatrix("23 12 11 13 46 23 Test1x.txt");
TestDatax3 = readmatrix("23 12 11 13 47 46 Test1x.txt");
TestDatax4 = readmatrix("23 12 11 13 49 16 Test1x.txt");
TestDatax5 = readmatrix("23 12 11 13 50 44 Test1x.txt");
TestDatax6 = readmatrix("23 12 11 13 52 14 Test1x.txt");
TestDatax7 = readmatrix("23 12 11 13 53 38 Test1x.txt");
TestDatax8 = readmatrix("23 12 11 13 55 09 Test1x.txt");
TestDatax9 = readmatrix("23 12 11 13 56 30 Test1x.txt");
TestDatax10 = readmatrix("23 12 11 13 58 12 Test1x.txt");

plot((TestDataty1(1,7)-TestDataty1(:,7)),TestDataty1(:,5)-TestDataty1(1,5),'r.')
hold on
plot((TestDataty2(1,7)-TestDataty2(:,7)),TestDataty2(:,5)-TestDataty2(1,5), 'r.')
plot((TestDataty3(1,7)-TestDataty3(:,7)),TestDataty3(:,5)-TestDataty3(1,5), 'r.')
plot((TestDataty4(1,7)-TestDataty4(:,7)),TestDataty4(:,5)-TestDataty4(1,5), 'r.')
plot((TestDataty5(1,7)-TestDataty5(:,7)),TestDataty5(:,5)-TestDataty5(1,5),'r.')
plot((TestDataty6(1,7)-TestDataty6(:,7)),TestDataty6(:,5)-TestDataty6(1,5), 'r.')
plot((TestDataty7(1,7)-TestDataty7(:,7)),TestDataty7(:,5)-TestDataty7(1,5), 'r.')
plot((TestDataty8(1,7)-TestDataty8(:,7)),TestDataty8(:,5)-TestDataty8(1,5), 'r.')
plot((TestDataty9(1,7)-TestDataty9(:,7)),TestDataty9(:,5)-TestDataty9(1,5), 'r.')
plot((TestDataty10(1,7)-TestDataty10(:,7)),TestDataty10(:,5)-TestDataty10(1,5), 'r.')
plot((TestDatax1(1,7)-TestDatax1(:,7)),TestDatax1(:,6)-TestDatax1(1,6), 'b.')
plot((TestDatax2(1,7)-TestDatax2(:,7)),TestDatax2(:,6)-TestDatax2(1,6), 'b.')
plot((TestDatax3(1,7)-TestDatax3(:,7)),TestDatax3(:,6)-TestDatax3(1,6), 'b.')
plot((TestDatax4(1,7)-TestDatax4(:,7)),TestDatax4(:,6)-TestDatax4(1,6), 'b.')
plot((TestDatax5(1,7)-TestDatax5(:,7)),TestDatax5(:,6)-TestDatax5(1,6), 'b.')
plot((TestDatax6(1,7)-TestDatax6(:,7)),TestDatax6(:,6)-TestDatax6(1,6), 'b.')
plot((TestDatax7(1,7)-TestDatax7(:,7)),TestDatax7(:,6)-TestDatax7(1,6), 'b.')
plot((TestDatax8(1,7)-TestDatax8(:,7)),TestDatax8(:,6)-TestDatax8(1,6), 'b.')
plot((TestDatax9(1,7)-TestDatax9(:,7)),TestDatax9(:,6)-TestDatax9(1,6), 'b.')
plot((TestDatax10(1,7)-TestDatax10(:,7)),TestDatax10(:,6)-TestDatax10(1,6), 'b.')
```

A.1.10. VisualPlotResult.m

```
% Initial positions
figure('Name', '3R plot')

n = [1:1:length(Data(:,1))]

for i2 = 1:length(n)
n0 = n(i2);

theta1 = theta_0(1)+deg2rad(Data(n0,1));
theta2 = theta_0(2)+deg2rad(Data(n0,2));
theta3 = theta_0(3)+deg2rad(Data(n0,2))+deg2rad(Data(n0,3));
theta4 = theta_0(4)+deg2rad(Data(n0,2))+deg2rad(Data(n0,3))+deg2rad(Data(n0,4));
theta5 = theta_0(5)+deg2rad(Data(n0,5));
theta6 = theta_0(6)+deg2rad(Data(n0,6));

theta = [theta1 theta2 theta3 theta4 theta5 theta6];

% Vector lengths
L1 = gamma_1*L;
L2 = gamma_2*L;
L3 = gamma_3*L;
L4 = gamma_4*L;
L5 = R;
L6 = Data(n0,7);

alpha  = linspace(0,360,361)           ;
Circle_x     = R*cosd(alpha)   ;
Circle_y     = R*sind(alpha) + L6 ;

% Plot initial vector loop
origin = [0;0];
r1 = [L1*cos(theta1); L1*sin(theta1)];
r2 = [L2*cos(theta2); L2*sin(theta2)];
r3 = [L3*cos(theta3); L3*sin(theta3)];
r4 = [L4*cos(theta4); L4*sin(theta4)];
r5 = [L5*cos(theta5); L5*sin(theta5)];
r6 = [L6*cos(theta6); L6*sin(theta6)];


loop_ccw = [origin r1 r1+r2 r1+r2+r3 r1+r2+r3+r4];
loop_cw = [origin r6 r6+r5];
loop_ccwmin = -loop_ccw;

plot(Circle_x, Circle_y, 'k--')
hold on
plot(loop_ccw(1,:),loop_ccw(2,:), 'r')
%plot(loop_ccwmin(1,:),loop_ccw(2,:), 'r')
plot(loop_cw(1,:),loop_cw(2,:), 'r')
plot(Xtot(n0),Ytot(n0),'o')
axis([-2*R 2*R 0 3*R])

hold off

H(i2) = getframe(gcf) ;
drawnow
% pause(0.1)
end

% create the video writer with 1 fps
  writerObj = VideoWriter('myVideo2.avi');
  writerObj.FrameRate = 10;
  % set the seconds per image
% open the video writer
open(writerObj);
% write the frames to the video
for ix=1:length(H)
    % convert the image to a frame
    frame = H(ix) ;
    writeVideo(writerObj, frame);
end
```

```
% close the writer object
close(writerObj);



%% For one instance
n0 = 1

theta1 = theta_0(1)+deg2rad(Data(n0,1));
theta2 = theta_0(2)+deg2rad(Data(n0,2));
theta3 = theta_0(3)+deg2rad(Data(n0,2))+deg2rad(Data(n0,3));
theta4 = theta_0(4)+deg2rad(Data(n0,2))+deg2rad(Data(n0,3))+deg2rad(Data(n0,4));
theta5 = theta_0(5)+deg2rad(Data(n0,5));
theta6 = theta_0(6)+deg2rad(Data(n0,6));

theta = [theta1 theta2 theta3 theta4 theta5 theta6];

% Vector lengths
L1 = gamma_1*L;
L2 = gamma_2*L;
L3 = gamma_3*L;
L4 = gamma_4*L;
L5 = R;
L6 = Data(n0,7);

alpha  = linspace(0,360,361)           ;
Circle_x     = R*cosd(alpha)   ;
Circle_y     = R*sind(alpha) + L6 ;

% Plot initial vector loop
origin = [0;0];
r1 = [L1*cos(theta1); L1*sin(theta1)];
r2 = [L2*cos(theta2); L2*sin(theta2)];
r3 = [L3*cos(theta3); L3*sin(theta3)];
r4 = [L4*cos(theta4); L4*sin(theta4)];
r5 = [L5*cos(theta5); L5*sin(theta5)];
r6 = [L6*cos(theta6); L6*sin(theta6)];


loop_ccw = [origin r1 r1+r2 r1+r2+r3 r1+r2+r3+r4];
loop_cw = [origin r6 r6+r5];
loop_ccwmin = -loop_ccw;

figure()
plot(Circle_x, Circle_y, 'k--')
hold on
plot(loop_ccw(1,:),loop_ccw(2,:), 'r')
plot(loop_ccwmin(1,:),loop_ccw(2,:), 'r')
% plot(loop_cw(1,:),loop_cw(2,:), 'r')
axis([-2*R 2*R 0 3*R])

hold off
```

A.2. Parametric Study

```
clearvars
close all
clc

tic
%% Choose the thickness (h) and revolution angle (psi) of the finger & load parameters
E = 195E9;                          % Pa (Spring Steel)
% E = 3.5E9;                        % Pa (PLA)
w = 20/1000;                        % m

% Tomato parameters and force due to the weight of tomato.
D_tomato = 0.06; % m
R = D_tomato/2;

h_val = (0.1:0.01:1)./1000; % m
```

```
psi_val = deg2rad(135:5:180);% deg
nms = 1;

dy = 0.001;
y_start = 0;
y_end = R;
y = y_start:dy:y_end;

Fx = zeros(length(y),length(psi_val),length(h_val));
Fy = zeros(length(y),length(psi_val),length(h_val));

for j = 1:length(h_val)
    for k = 1:length(psi_val)
        h = h_val(j);
        psi = psi_val(k);
        I = w*h.^3/12;                  % m^4 --> design freedom
        L = psi*R ;
        PRBMParameters; % Load in the parameters (gamma, zeta etc.) from the 3R PRBM method

        %% Plot initial vector loop
        VectorLoopValues;

        %% Optimization problem

        dtheta = deg2rad([0 0 0 0 0 0]);
        dtheta1 = dtheta(1);
        dtheta2 = dtheta(2);
        dtheta3 = dtheta(3);
        dtheta4 = dtheta(4);
        dtheta5 = dtheta(5);
        dtheta6 = dtheta(6);

        for i = 1:length(y)
        % Initial values
        x0 = [dtheta2 dtheta5];
        dtheta34_0 = [dtheta3 dtheta4];
        lb = x0 + 1000*dy*deg2rad([-2 -15]);
        ub = x0 + 1000*dy*deg2rad([2 15]);
        L6 = R+y(i);

        % Find min PE
        objective = @(x)ObjPE2 (x,dtheta34_0,theta_0,L1,L2,L3,L4,L5,L6,K_theta2,K_theta3,
            K_theta4);

        % MultiStart Optimizer:
        ms = MultiStart('Display','off');
        options=optimset('Algorithm','interior-point','GradObj','off','Hessian','off','tolX'
            ,1e-10,'TolFun',1e-10,'MaxIter',100,'MaxFunEvals',10000);
        problem = createOptimProblem('fmincon','x0',x0,'lb',lb,'ub',ub,'Aeq',[],'beq',[],'
            nonlcon',[],'objective',objective,'options',options);
        [x,fval,exitflag,output,solutions] = run(ms,problem,nms);

        dtheta2 = x(1);
        dtheta5 = x(2);

        % calculate mechanism angles
        fun = @(dtheta34)vectorloopequation2(dtheta34,dtheta2,dtheta5,theta_0,L1,L2,L3,L4,L5,
            L6);

        [dtheta34] = fsolve(fun,dtheta34_0);
        dtheta3 = dtheta34(1);
        dtheta4 = dtheta34(2);

        DataStorage;
        end

        %% Forces calculated by fourth rigid beam (gamma_4*L)
        omega = theta_0(5)+deg2rad(Data(:,5));
        omega3 = deg2rad(180)-(zeta_1+zeta_2+zeta_3+zeta_4+deg2rad(Data(:,2)+Data(:,3)+Data
            (:,4)));

```

```
        T2 = K_theta2.*deg2rad(Data(:,2));
        T3 = K_theta3.*deg2rad(Data(:,3));
        T4 = K_theta4.*deg2rad(Data(:,4));

        X = L*gamma_4*cos(omega3);
        Y = L*gamma_4*sin(omega3);

        F = T4./(-Y.*cos(omega)-X.*sin(omega));
        Fx(:,k,j) = F.*cos(omega);
        Fy(:,k,j) = F.*sin(omega);
    end
end
toc

%% Cleaning data
Fy_filtered = filloutliers(Fy, 'pchip');

maxFy = squeeze(max(Fy_filtered));
maxFy = filloutliers(maxFy, 'pchip');

%% Fitting maxFy curves
g = 9.81;                   % m/s^2
m_tomato = 0.1;             % kg
Fz_tomato = m_tomato*g;     % Force limit
n_f = 3;                    % number of fingers

figure()
plot(1000*h_val,maxFy(1:end,:))
hold on
yline(Fz_tomato/n_f)
ylim([0 Fz_tomato])
xlabel('$h$ [$mm$]','Interpreter','latex'), ylabel('Max $F_y$ [$N$]','Interpreter','latex')
title('Max $F_y$: $R$ = 30 $mm$, $E$ = 195 $GPa$ (Stainless steel), $n$ = ' + string(n_f) +','
    Interpreter','latex')
legend(["$\psi$ - " + string(rad2deg(psi_val(1:end))) + " deg", "$F_z$"],'Interpreter','latex
    ', 'Location','northeastoutside')
hold off
grid on

for i = 1:length(psi_val)
    p = polyfit(h_val,maxFy(i,:),5);
    x1 = linspace(h_val(1),h_val(end),1000);
    w1(i,:) = polyval(p,x1);
end

figure()
plot(x1,w1)
hold on
yline(Fz_tomato/n_f)

%% Psi - h relation fit and plot
% Given data
maxFy_data = w1;

% Number of rows
num_rows = size(maxFy_data, 1);

% Initialize array to store intersection points
intersection_points = zeros(num_rows, 2);

% Iterate through each row
for i = 1:num_rows
    % Find the intersection point with yline(Fz_tomato/6)
    y_line = Fz_tomato/n_f;
    row_data = maxFy_data(i, :);

    % Find the index where the row_data intersects with y_line
    [~, index] = min(abs(row_data - y_line));

    % Store the intersection point
    intersection_points(i, :) = [x1(index), row_data(index)];
```

```
end
p2 = polyfit(intersection_points(:,1),rad2deg(psi_val(1:end)),3);
x2 = linspace(intersection_points(1,1),intersection_points(end,1),1000);
y2 = polyval(p2,x2);
figure()
plot(intersection_points(:,1),rad2deg(psi_val(1:end)),'o')
hold on
plot(x2,y2)
xlabel('h [m]'), ylabel('\psi (deg)')
legend('Intersection points', 'Fitted')
grid on
title('\psi-thickness relation at m = 100 g and R = 30 mm')
```

B

Determining the kinetics with the Jacobian

B.1. Theory

In the model, the kinetics are determined by using the fourth link of the mechanism and drawing a free-body diagram. This method is fast and therefore is implemented in the parametric study. However, determining the kinetics based on only the deformation of the fourth link makes room for numerical errors, as the deformation angles are determined by minimizing the potential energy and therefore approximating the kinematics. Another, more accurate, method, as described in the paper by K. Venkiteswaran [29], can be used, where the kinetics are defined as shown in Equation B.1. This method, however, is not implemented in the parametric study due to the higher computational load.

$$\vec{\boldsymbol{\tau}} = \mathbf{J}^{\mathbf{T}} \vec{\boldsymbol{W}} \tag{B.1}$$

By rewriting this equation, as in Equation B.2, the external loads are found.

$$\vec{\boldsymbol{W}} = \mathbf{J}^{\mathbf{T}^{-}} 1 \vec{\boldsymbol{\tau}} \tag{B.2}$$

Where, when a force at a certain angle and a moment is applied at the tip of the mechanism, the load vector $\vec{\boldsymbol{W}}$ is defined as

$$\vec{\boldsymbol{W}} = \begin{bmatrix} F\cos(\phi) \\ F\sin(\phi) \\ M \end{bmatrix}$$

and the internal moments, $\vec{\boldsymbol{\tau}}$, of the PRB torsion springs are defined by

$$\vec{\boldsymbol{\tau}} = \begin{bmatrix} K_{\theta 2}\delta\theta_2 \\ K_{\theta 3}\delta\theta_3 \\ K_{\theta 4}\delta\theta_4 \end{bmatrix}$$

and the Jacobian of the mapping of the tip coordinates [5] with respect to the angular rotations is

$$\mathbf{J} = \begin{bmatrix} \frac{\delta X_{tip}}{\delta\delta\theta_2} & \frac{\delta X_{tip}}{\delta\delta\theta_3} & \frac{\delta X_{tip}}{\delta\delta\theta_4} \\ \frac{\delta Y_{tip}}{\delta\delta\theta_2} & \frac{\delta Y_{tip}}{\delta\delta\theta_3} & \frac{\delta Y_{tip}}{\delta\delta\theta_4} \\ \frac{\delta\theta_{tip}}{\delta\delta\theta_2} & \frac{\delta\theta_{tip}}{\delta\delta\theta_3} & \frac{\delta\theta_{tip}}{\delta\delta\theta_4} \end{bmatrix}$$

B.2. Implementation in MATLAB

The calculation of the force with the Jacobian method, as described in this appendix, is implemented in the MATLAB code as depicted below.

```
%% Positions
theta1 = zeta_1;
theta2 = zeta_1+zeta_2+deg2rad(Data(:,2));
theta3 = zeta_1+zeta_2+zeta_3+deg2rad(Data(:,2)+Data(:,3));
theta4 = zeta_1+zeta_2+zeta_3+zeta_4+deg2rad(Data(:,2)+Data(:,3)+Data(:,4));

origin = zeros(length(Data(:,1)),2);
r1 = ones(length(Data(:,1)),1).*gamma_1*L*[cos(theta1) sin(theta1)]
r2 = gamma_2*L*[cos(theta2) sin(theta2)]
r3 = gamma_3*L*[cos(theta3) sin(theta3)]
r4 = gamma_4*L*[cos(theta4) sin(theta4)]

Xtot = r1(:,1)+r2(:,1)+r3(:,1)+r4(:,1)
Ytot = r1(:,2)+r2(:,2)+r3(:,2)+r4(:,2)

% %% Jacobian calculation
syms dt2 dt3 dt4

t1 = zeta_1;
t2 = zeta_1+zeta_2+dt2;
t3 = zeta_1+zeta_2+zeta_3+dt2+dt3;
t4 = zeta_1+zeta_2+zeta_3+zeta_4+dt2+dt3+dt4;

Xtip = L*(gamma_1*cos(t1)+gamma_2*cos(t2)+gamma_3*cos(t3)+gamma_4*cos(t4))
Ytip = L*(gamma_1*sin(t1)+gamma_2*sin(t2)+gamma_3*sin(t3)+gamma_4*sin(t4))
thetatip = psi+dt2+dt3+dt4

J = jacobian([Xtip, Ytip, thetatip],[dt2,dt3,dt4] );

for k = 1:length(Data(:,1))
Jsub= subs(J,{dt2 dt3 dt4},{deg2rad(Data(k,2)) deg2rad(Data(k,3)) deg2rad(Data(k,4))})
tau = [K_theta2.*deg2rad(Data(k,2)); K_theta3.*deg2rad(Data(k,3)); K_theta4.*deg2rad(Data(k
    ,4))]
W(:,k) = inv(transpose(Jsub))*tau
end

%% Forces calculated by Jacobian method
Fx2 = W(1,:);
Fy2 = W(2,:);
Ftot2 = sqrt(Fx2.^2+Fy2.^2);
```

C

Design Iterations

C.1. Experimental setup

C.1.1. First iteration

The first iteration of the test setup was a basic representation of the schematic test setup idea that was depicted in Figure 5.1.
This design consisted of a 3D-printed solid PETG disk mounted on a linear stage that was prefabricated. Several connection parts for the linear stage were designed for 3D printing. The testpiece was a big, thin 3D printed curvature that was mounted to a structure that was connected to the main breadboard. A phone holder was 3D printed and mounted on a bridge made of THORLABS optical rails to do visual measurements with the camera of a phone.
The linear stage that would be used for this design, however, took a long time to be delivered and the 3D printed parts were not designed in a very robust way, which would lead to deflection of the material while measuring the forces. This would then result in errors in the measured reaction force and the actual reaction force.

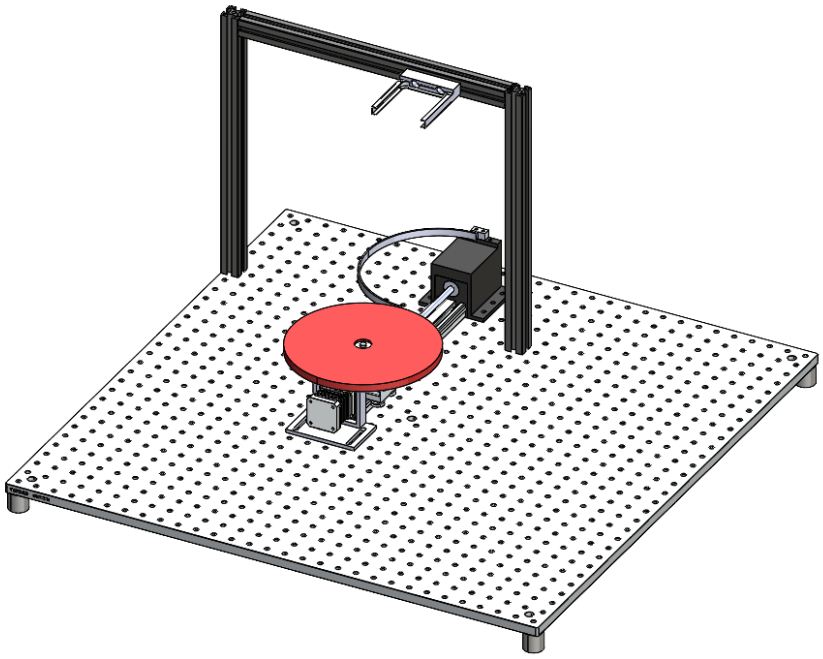

Figure C.1: An illustration of the first concept of the experimental test setup

C.1.2. Second iteration

The second iteration, as depicted in Figure C.2, consists of the same linear slider setup that is used in the final design because this was available at the university at that moment. The disk is mounted to THROLABS optical rails and a bridge is created to connect the optical rails to the linear sliders. Below this bridge a 3D-printed part is mounted that holds the spindle nut. The (unfinished) 3D printed part that would function as the testpiece mounting hub was designed such that in the y-direction the part would push the y-direction load cell.

This design was not further developed as the design was observed to be a stack of different parts, such as the bridge and spindle connection part. This results in possible moments around the x-axis. Therefore, in the final test setup design, the requirements were set that the height of the load cells would be collinear with the axis of the spindle and therefore the center of the height of the disk should also be collinear with this axis.

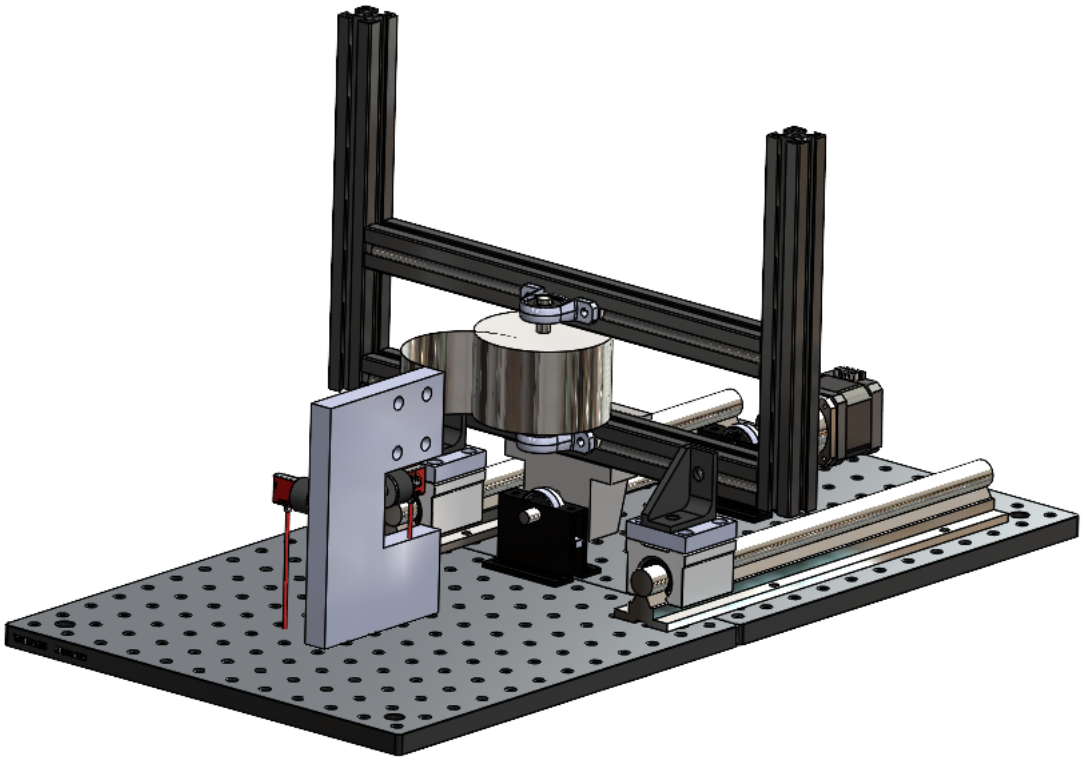

Figure C.2: An illustration of the second concept of the experimental test setup

C.2. Gripper design

C.2.1. First iteration: basic concept

The first iteration of the gripper design contains the basic idea of the initially curved thin fingers that are extracted from and retracted in a finger hull. The first design is similar to the final design, but for a wider finger of a width of 20 mm, and with a lower curvature of the slot inside and thin walls. This design was not yet designed to be implemented in a series of two or three fingers simultaneously and therefore there is not yet a slot that connects the finger to the (triangular) actuation part.

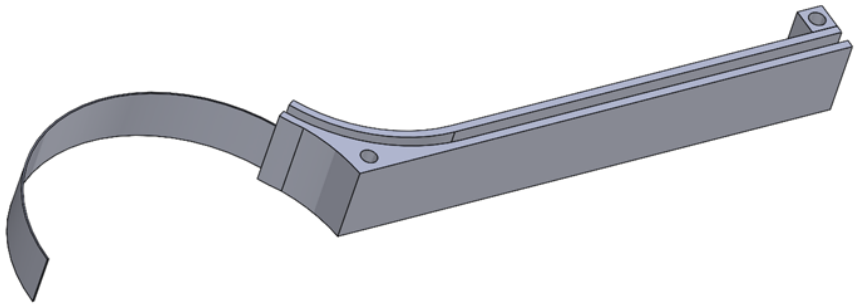

Figure C.3: Design iteration 1: the basic concept.

C.2.2. Second iteration: slot addition

In the second iteration slots for the actuation part are added.

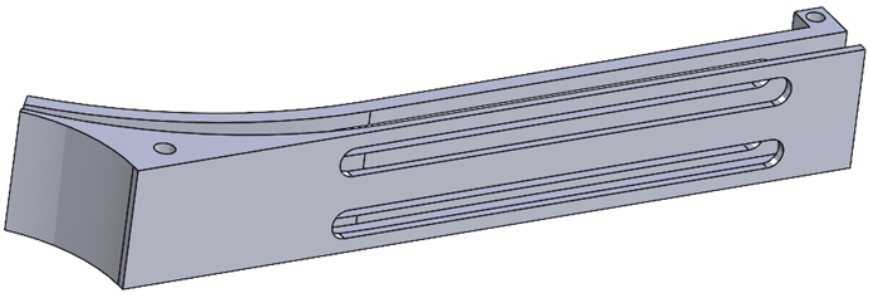

Figure C.4: Design iteration 2: two slots are added.

C.2.3. Third iteration: adjusting printing direction

In the third iteration, the printing direction of the hull is changed, such that the slot for the connection to the actuation part is smooth, while this was not the case when printing in the direction of the first and second iterations. This additionally would mean that a curved top part would be printed and glued to the base. However, connecting the plate to the base was only possible with glue and as there is tension inside the hull, due to the retracting of the leaf spring backbones, this glued connection would not be strong enough. Furthermore, the plate was very thin and therefore hard to print in high quality.

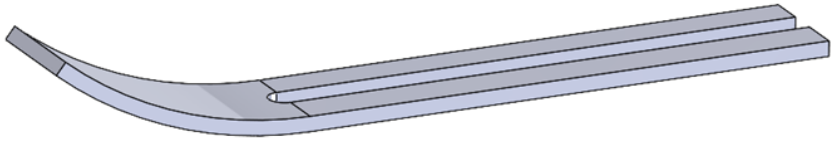

(a) Design iteration 3, the top plate.

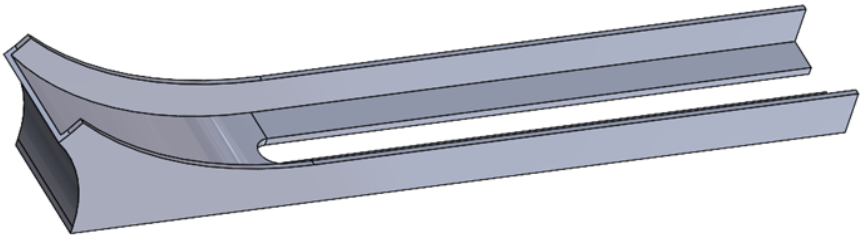

(b) Design iteration 3, the base.

Figure C.5: Design iteration 3: the printing direction was adjusted, resulting in a two-part design of the hull.

C.2.4. Fourth iteration: adjusting bending radius

As in the third iteration, the tension of the retracting of the leaf spring backbone caused problems and it was also observed that retracting the leaf spring with this radius of curvature at the end of the hull caused plastic deformation the idea came to mind to adjust the radius of curvature at the hull to a greater radius.

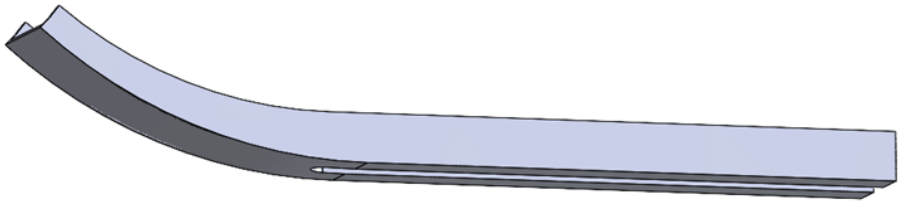

Figure C.6: Design iteration 4: the bending radius is adjusted.

C.2.5. Fifth iteration: triangular connection

In the fifth iteration, the connection of the hulls in a triangular configuration was the main focus point, such that three gripper fingers could function as one gripper. This is a solid design, where the finger is split up into an upper and a lower section in the printer and afterward glued together. However, because of the thin walls and the open back section, there was not a lot of surface to glue the parts together and the design had low stiffness.

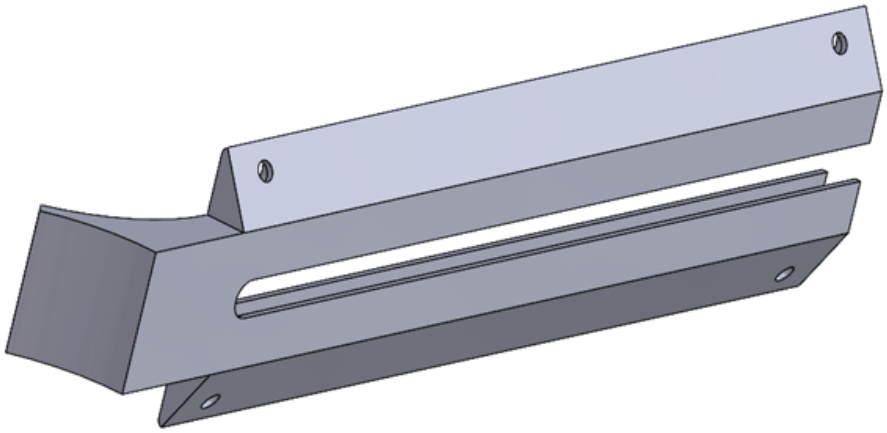

Figure C.7: Design iteration 5: a triangular connection section is added.

C.2.6. Final iteration

In the final iteration, the outside walls of the base were made thicker and the back end was closed off. Furthermore, due to the parametric study, it was observed that the finger could become less wide and therefore the width of the fingers was adjusted to 10 mm. This resulted in the triangular connection design as in the fifth iteration would require too much space for the bolts. Therefore, small connection parts were designed to mount the three finger hulls to each other.

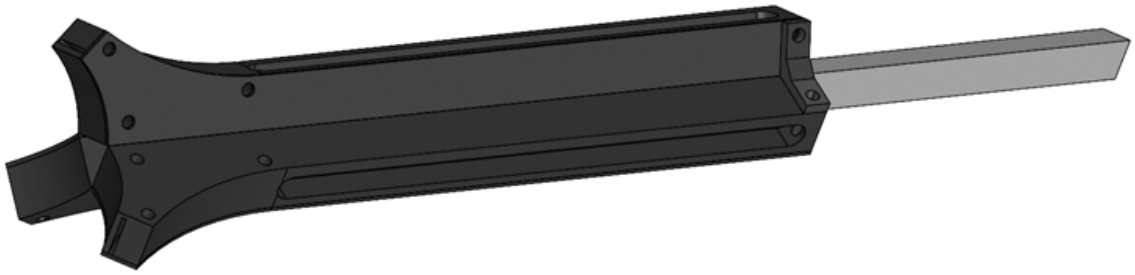

Figure C.8: Illustration of the final design.

D

Motor control with Arduino and UGS Platform

D.1. Arduino GRBL

To be able to use the stepper motor and drive with the UGS platform software the GRBL code has to be uploaded to the Arduino. This code is a parallel port designed for CNC milling. Further instructions and the code can be downloaded from: https://github.com/grbl/grbl

D.2. UGS platform

The stepper motor can be controlled with the software UGS Platorm, which is software that uses universal gcode to move stepper motors in 3 degrees of freedom.
The stepper motor can be initialized by selecting the COM-port in which the Arduino is connected and selecting the same baud-rate as the Arduino is using.
The stepper motor can be moved and the stepsize and speed for moving in each direction can be adjusted by the jog controller. A visualization of the main window of the UGS Platform is shown in Figure D.1.

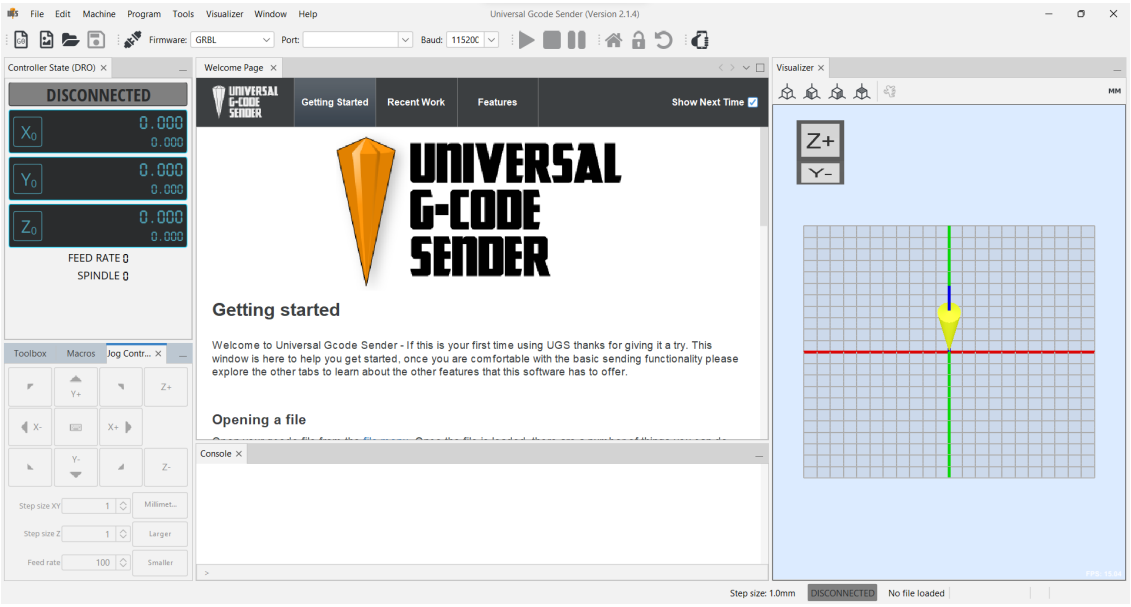

Figure D.1: The main window of the UGS platform. At the top of the window, the COM port and baud-rate can be selected. At the bottom left the jog controller can be found.

E

Testpiece Iterations

E.1. PLA testpieces

The PLA testpieces were 3D-printed, as this was the manufacturing method that was the easiest to implement, and with 3D-printing rapid adjustments, such as change of the thickness or change of the enclosing angle of the testpiece, could be made. This great variation of testpieces can be seen in Figure E.1.

Figure E.1: Different iterations of a PLA testpiece

The first testpiece design was mounted inside the testpiece mounting hub and was therefore removable.

This was done such that multiple tests could be done with the same mounting hub, but different testpieces. This mounting method is shown in Figure E.2. However, it was concluded during testing, that this mounting method would not provide the rigid support as was required for accurate measurements in comparison to the simulation, as in the simulation a cantilever support was assumed for the initially-curved mechanism. Therefore, for the final test, it was chosen to print the testpiece directly to the mounting hub, such that a rigid force transmission between the tip of the testpiece and the connection points of the load cells was accomplished.

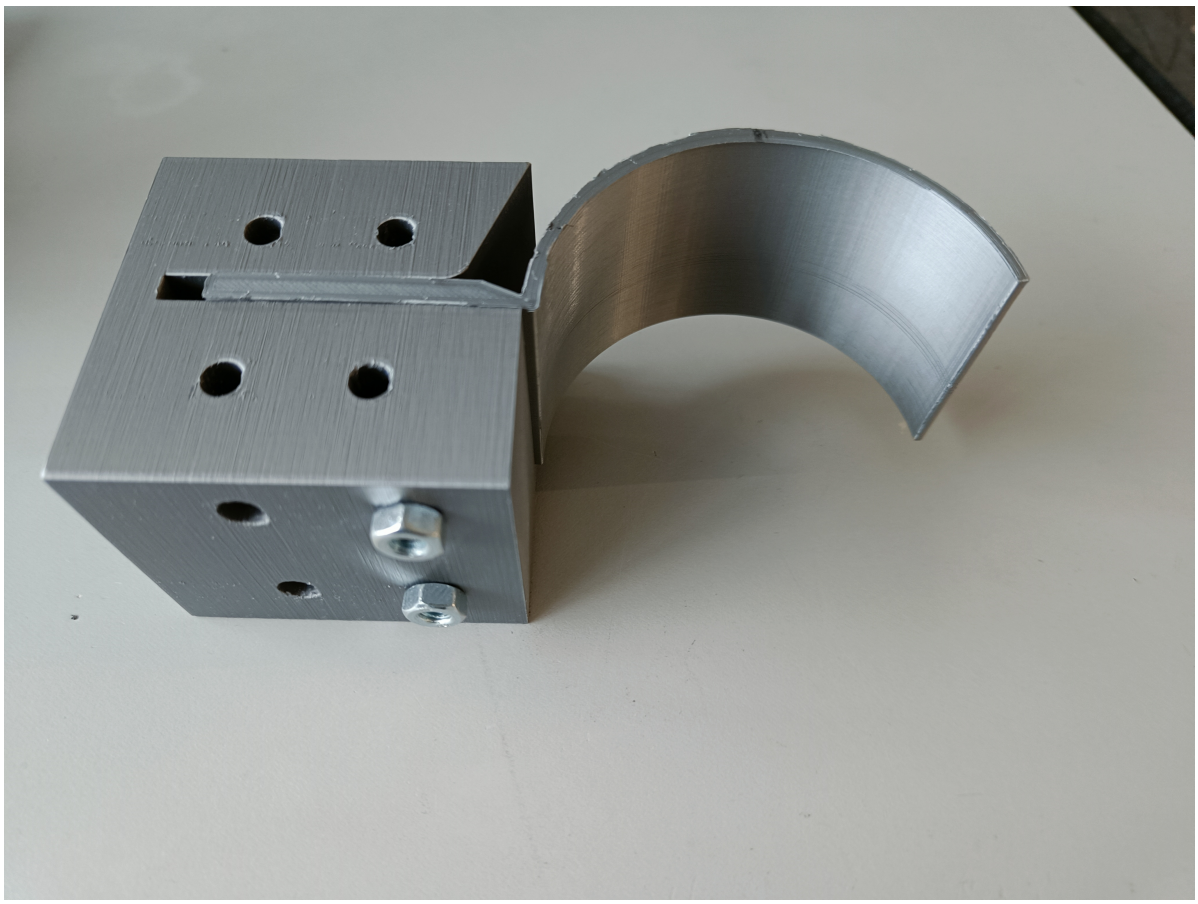

Figure E.2: An early design of the PLA testpiece connection hub

E.2. Steel testpieces

As was observed from the first measurements that were conducted with the PLA testpieces, was that there was an error between the simulated and the measured reaction force. It was hypothesized that the non-homogeneity of the 3D-printed PLA testpiece was the main source of this error. Therefore, steel testpieces were made as this material is homogeneous, and therefore the material properties are known. The steel testpieces are laser cut from a steel plate and bent with cylinders. Testpieces were made with 1 mm, 1.5 mm and 2 mm thickness.
In the final stage of the steel testpieces, the regular steel plate was replaced with stainless steel leaf springs, such that no plastic deformation would occur when the object was extracted from the testpiece.

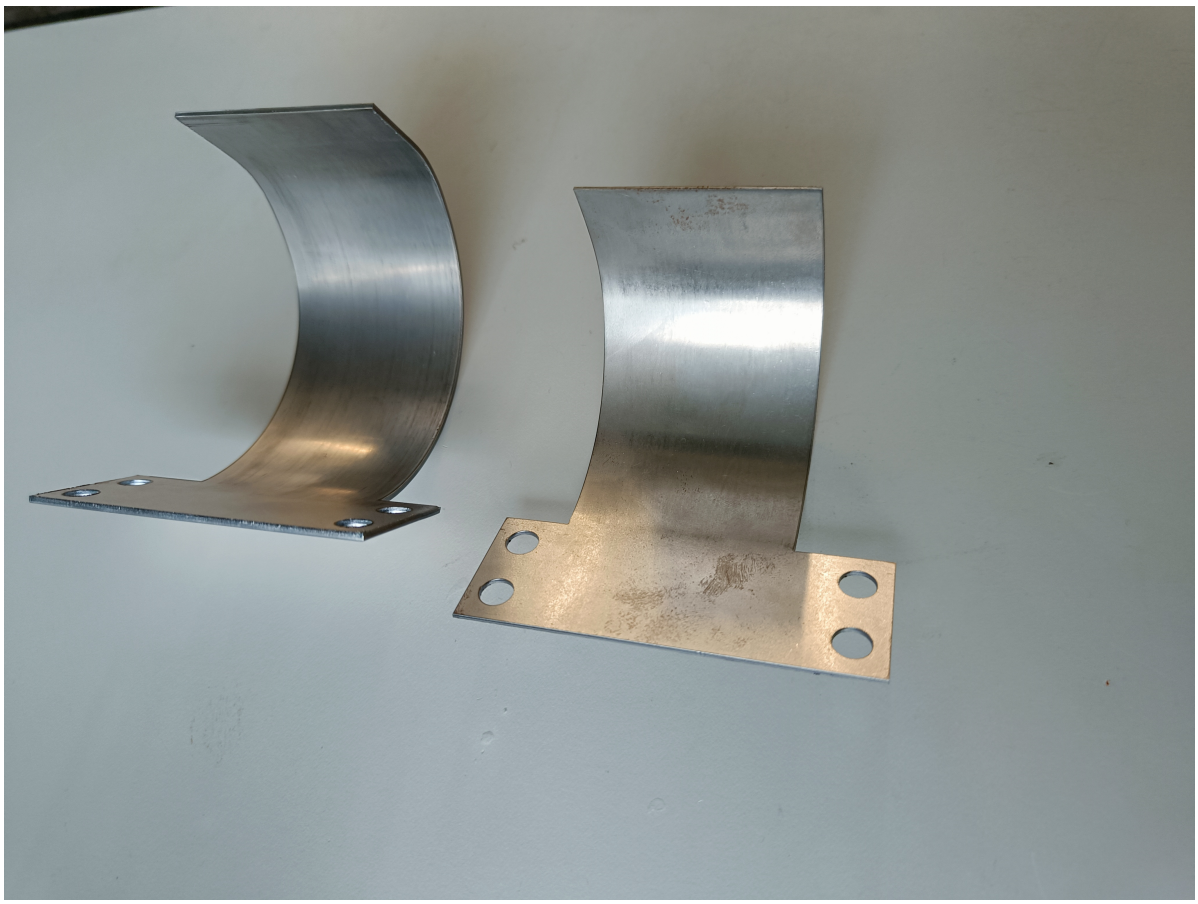

Figure E.3: A picture of two curved steel testpieces of 1 mm thickness.

F

Young's modulus test PLA

To approximate the Young's modulus of 3D printed PLA, which is used in the PLA testpiece, a test is done, from which the force-deflection relation for a PLA beam resulted, as given in Figure F.4.
The test was based on the Euler-Bernoulli beam equations, where in this test a cantilever beam is used with one end on a cantilever support and the other end free and loaded by force F, as shown in Figure F.1. The beam equation for this beam is defined by Equation F.1, where y is the displacement of the tip of the beam in the y-direction, L is the length of the beam, F is the force on the tip, E is the Young's modulus of the beam material and I is the area moment of inertia of the beam, which is defined by $\frac{wh^3}{12}$ for a rectangular cross-sectional area, in which w is the width of the cross-section and h is the height of the cross-section.

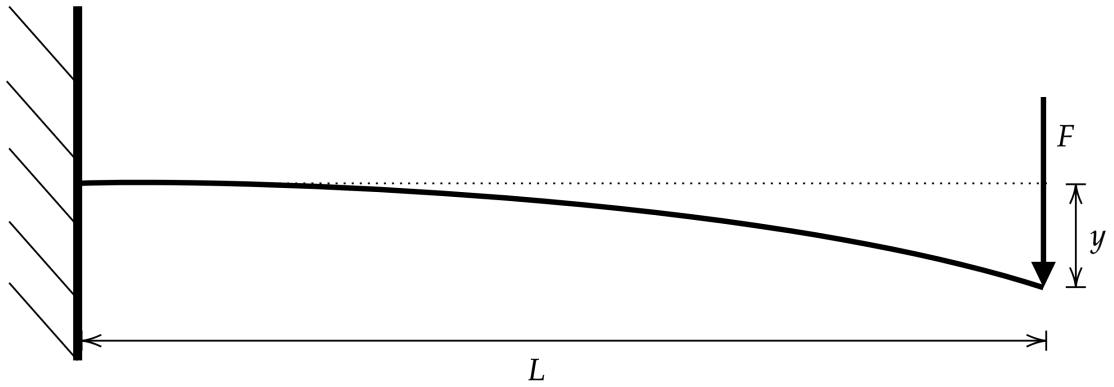

Figure F.1: Cantilever beam as used in the Young's modulus test: F depicts the force on the beam, L depicts the length of the beam and y depicts the deflection of the beam.

$$y = \frac{FL^3}{3EI} \tag{F.1}$$

The beam that is used for this test has a length L of 100 mm, a width w of 25 mm, and a thickness h of 5 mm. The beam and test setup are shown in Figure F.2 and a picture of calibrating the beam at the right position, such that no initial deflection occurs, is shown in Figure F.3.

The beam equations are rewritten such that the Young's modulus can be determined when the force and deflection is known. The rewritten equation is shown in Equation F.2, where $n_e = \frac{\Delta F}{\Delta y}$, which is the ratio between the difference of the measured force and displacement of two data points.

$$E = \frac{n_e L^3}{3I} \tag{F.2}$$

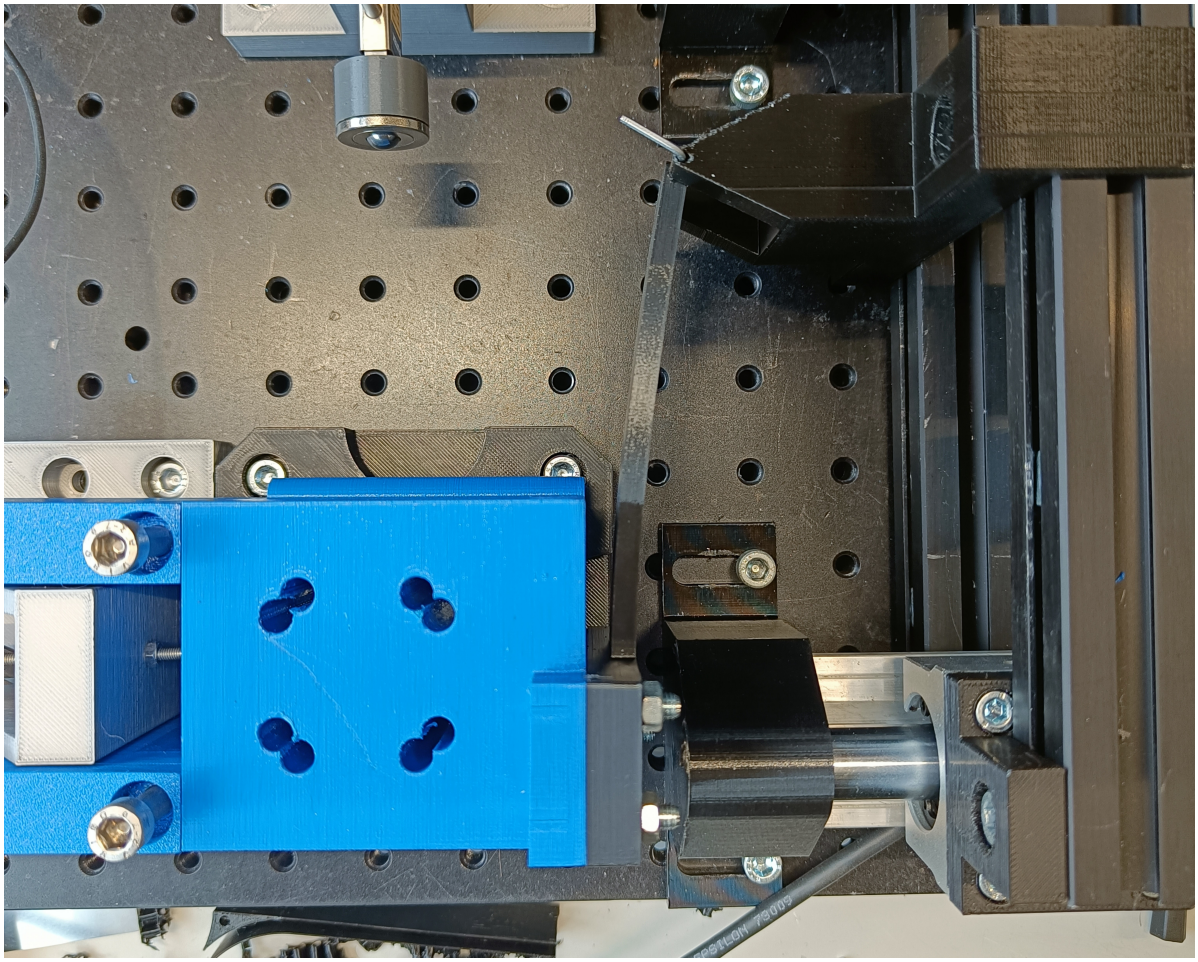

Figure F.2: A picture of the deflected testpiece during the Young's modulus test.

The results are shown in Figure F.4. It can be observed that from approximately a displacement of 4 mm a linear relation between the force and displacement is visual, so the range above the displacement of 4 mm is used for this test, and data points in that range are selected for calculating the force difference and displacement difference in Equation F.2. The resulting Young's modulus is the approximation of the Young's modulus of 3D printed PLA.

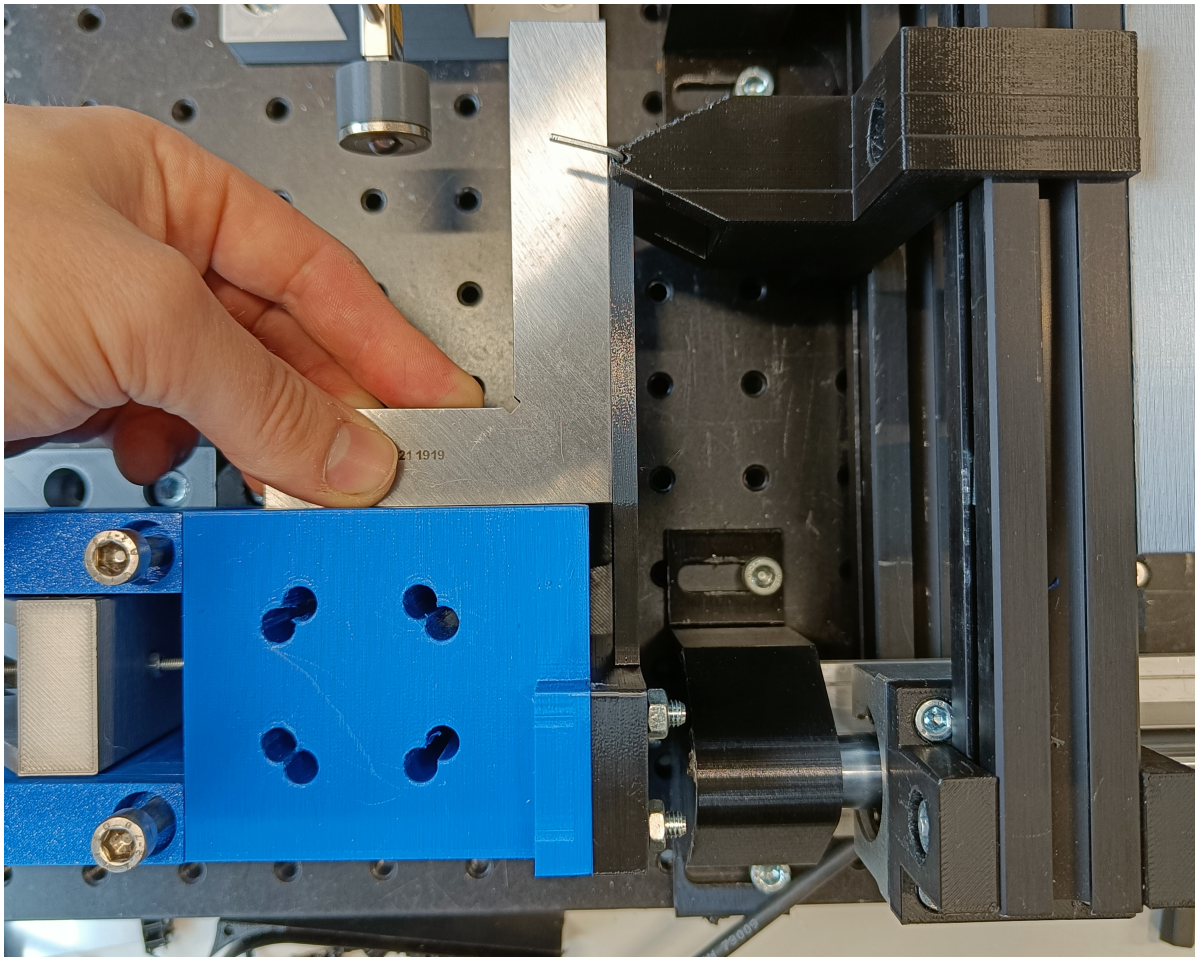

Figure F.3: A picture of the calibration of the correct distance of the motion stage w.r.t. the force measurement stage, such that no initial deflection occurs.

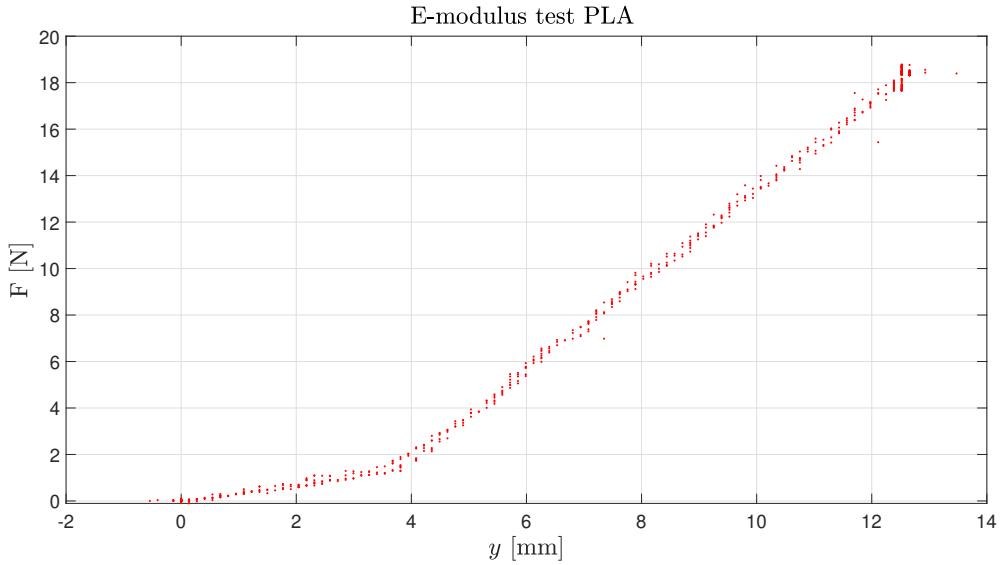

Figure F.4: Results from the test for approximating the Young's modulus of a 3D printed PLA. The red dots represent the measured force at a displacement y.

G

LABVIEW

The graphical programming environment LABVIEW is a software that implements virtual instruments, that can be used in test setups to acquire experimental data. For this thesis, LABVIEW is used to acquire measurement data of the load cells and distance laser.
The front view of the LABVIEW environment is depicted in Figure G.1. Here two main sections are visible. In the upper section, the signal from the load cells is plotted and the signal can be calibrated with the interface next to the signal display. The lower section displays the signal from the distance laser. Above the measurement displays the path for the measurement files can be inserted and the correct analog ports from the NI-USB 6008 I/O device can be selected. Next to the upper display, a button is implemented that can be switched on when the data has to be saved. Below this button, a button containing 'STOP' is implemented to stop the LABVIEW code from executing.

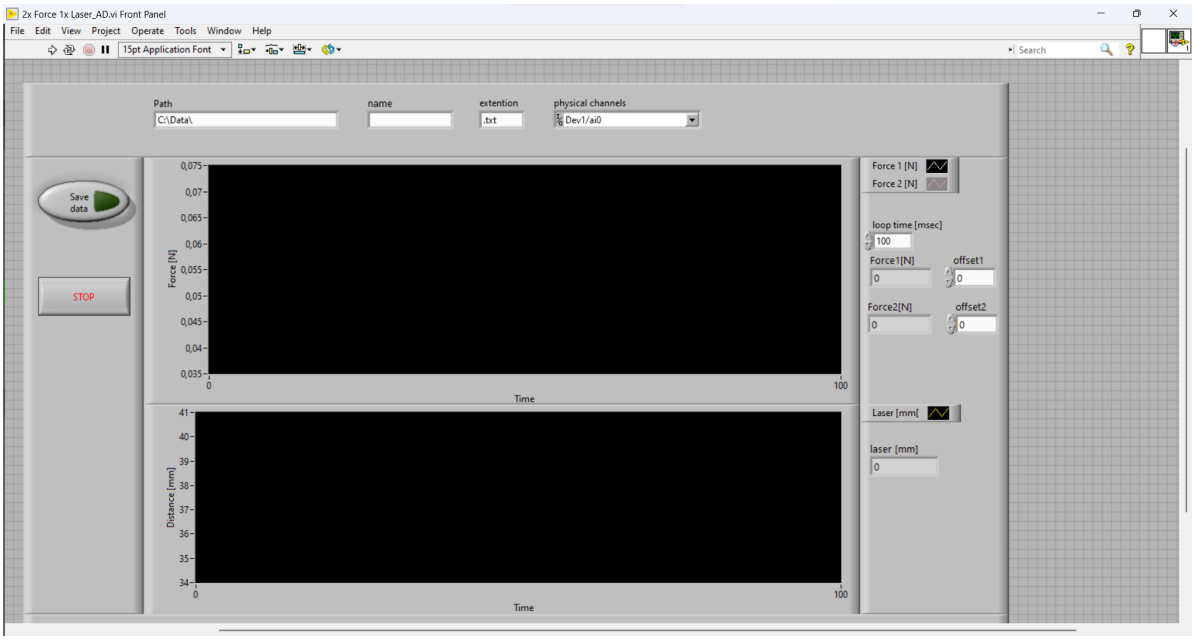

Figure G.1: A screenshot of the front window of the LABVIEW setup.

In Figure G.2 the back-end window of the LABVIEW code is depicted. This visualizes the implemented structures of the code, such that the sensor data is converted from analog to digital, and depicts the instruments that are used to generate the user interface that is displayed in the front window.

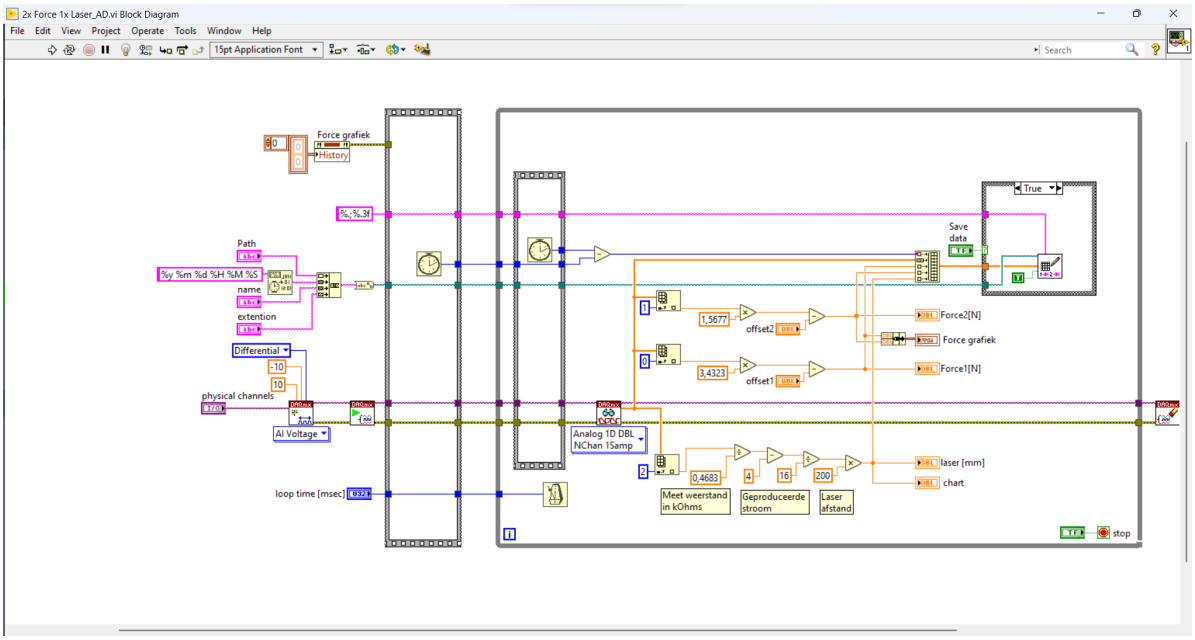

Figure G.2: A screenshot of the back-end window, where the LABVIEW coding structure is depicted.

H

Additional results of parametric study

H.1. Stainless steel

For the implementation of the parametric study in the design for a stainless steel gripper finger, multiple sweeps are done. The load case was based on six backbones, such that a sleeve could be implemented. Multiple widths are studied, which are shown in Figure H.1a, Figure H.2a and Figure H.4a. The resulting relations between the enclosing angle and thickness for each width of the finger are determined by the intersection points of the plots shown above and the force limit. These relations are shown in Figure H.1b, Figure H.2b and Figure H.3b.

H.2. PLA

For PLA just a single width was studied, as the design was already chosen to be made out of stainless steel. The results of a finger with a width of 20 mm are shown in Figure H.4.

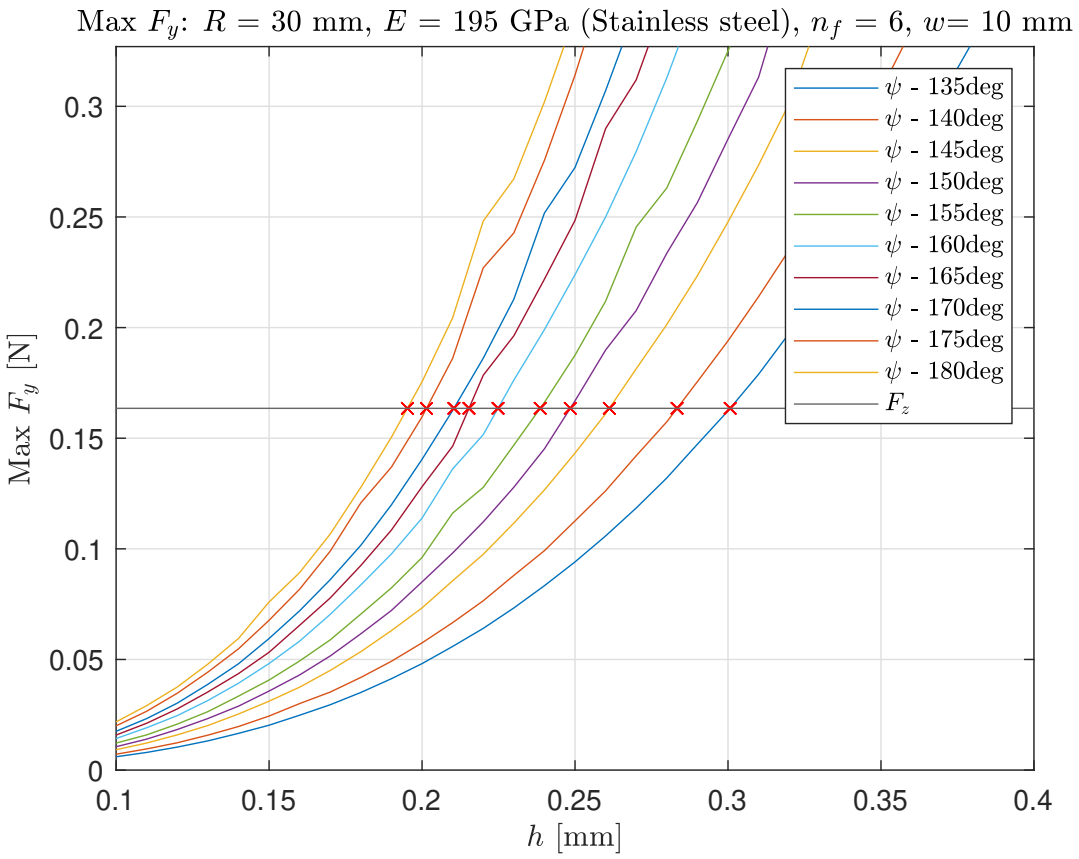

(a) Relation between the maximum pull-out force F_y and the thickness h, for ten different constant values of the enclosing angle ψ. The black line depicts the force limit in the parametric study, based on the payload of the object. The red crosses depict the intersection points between the maximum force-thickness plot and the force limit, resulting in the ultimate combination for a value for h and ψ where the finger can hold the payload. The finger is made from stainless steel and has a width of 10 mm.

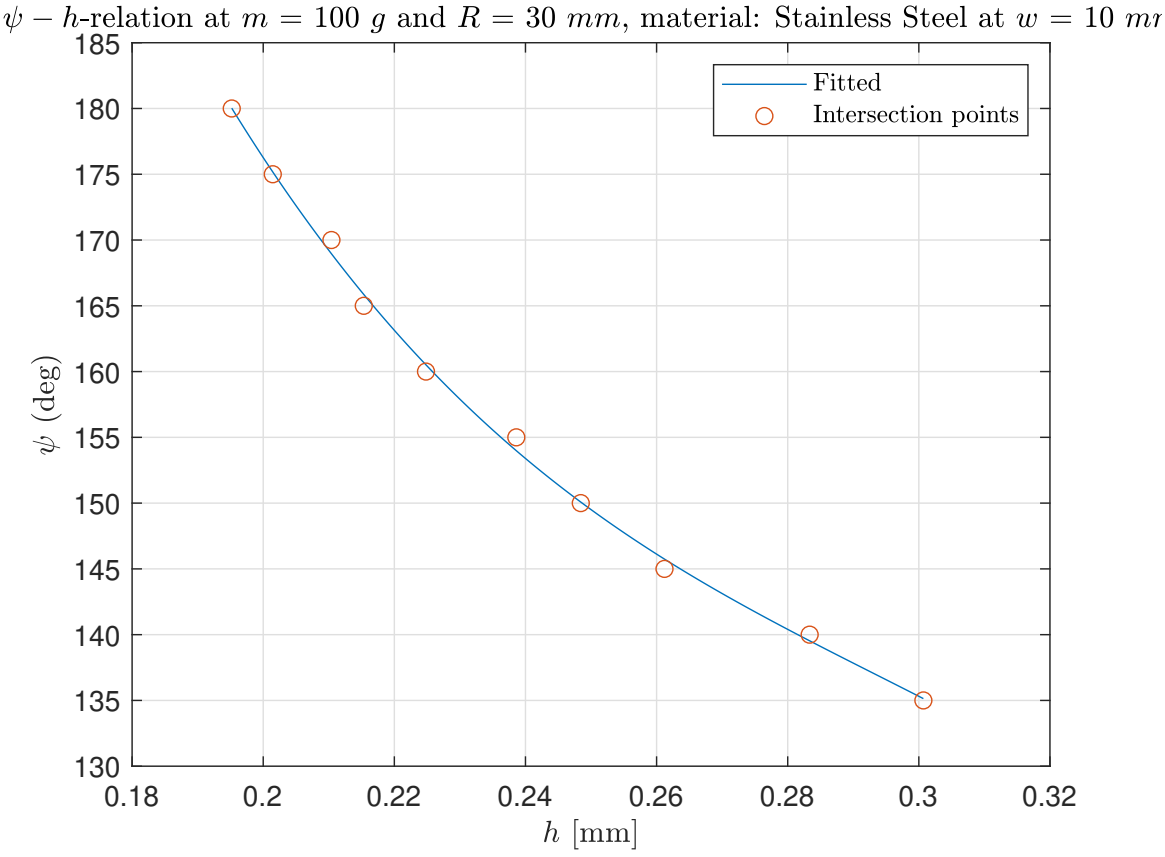

(b) Design chart: the relation between the enclosing angle and the finger thickness for a parametric sweep with stainless steel as chosen material. The circles represent the intersection points and the continuous line is the 3rd-degree fitted polynomial.

Figure H.1: Parametric study results and design chart for a stainless steel finger with a width of 10 mm.

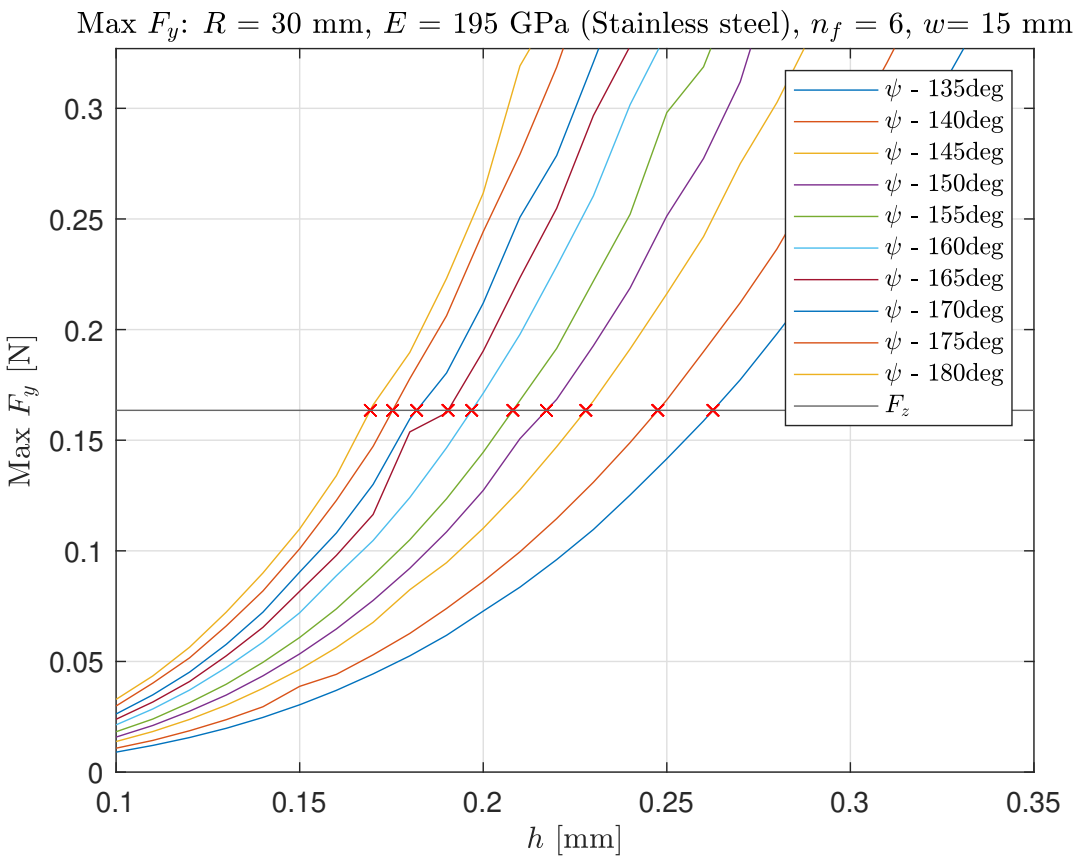

(a) Relation between the maximum pull-out force F_y and the thickness h, for ten different constant values of the enclosing angle ψ. The black line depicts the force limit in the parametric study, based on the payload of the object. The red crosses depict the intersection points between the maximum force-thickness plot and the force limit, resulting in the ultimate combination for a value for h and ψ where the finger can hold the payload. The finger is made from stainless steel and has a width of 15 mm.

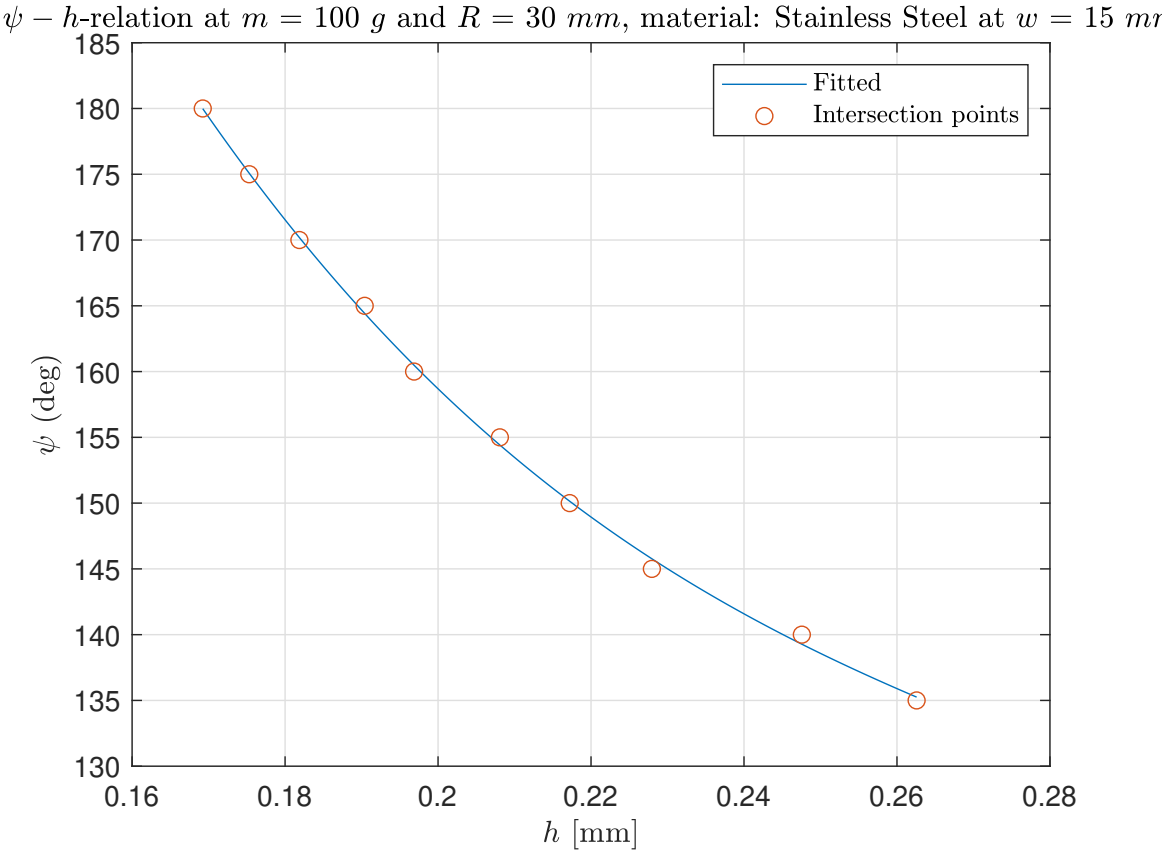

(b) Design chart: the relation between the enclosing angle and the finger thickness for a parametric sweep with stainless steel as chosen material. The circles represent the intersection points and the continuous line is the 3rd-degree fitted polynomial.

Figure H.2: Parametric study results and design chart for a stainless steel finger with a width of 15 mm.

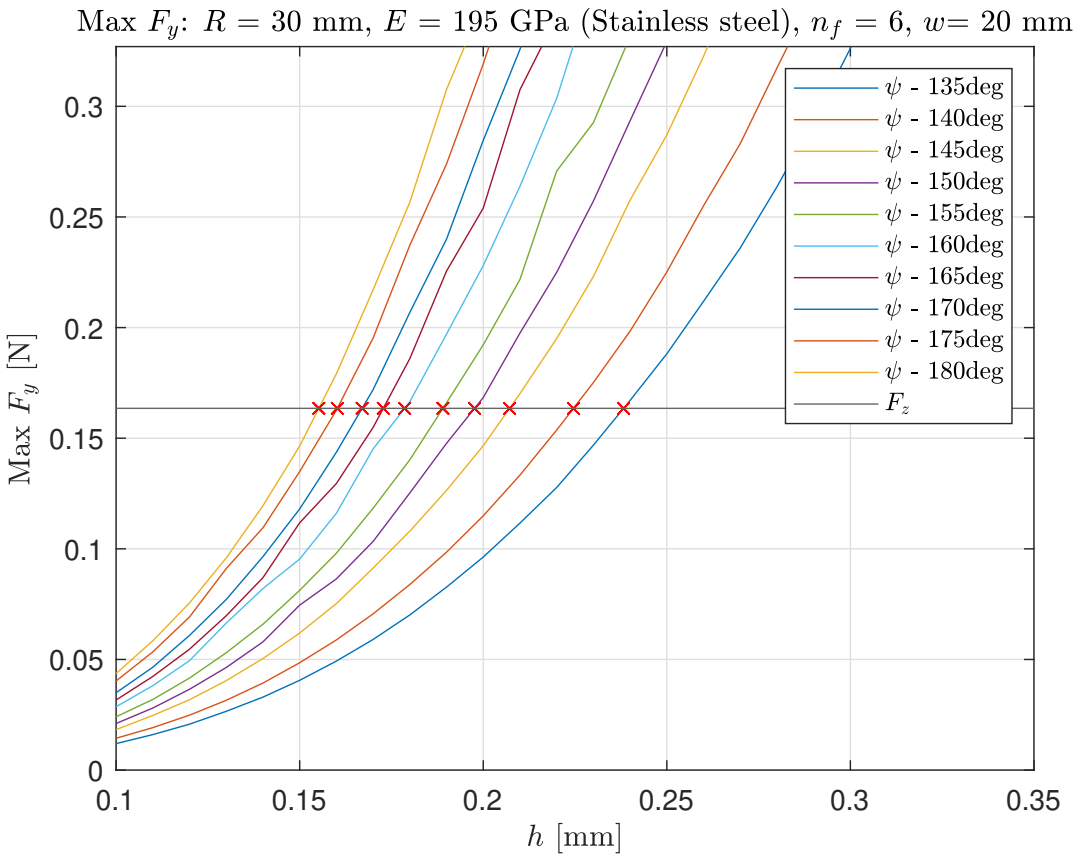

(a) Relation between the maximum pull-out force F_y and the thickness h, for ten different constant values of the enclosing angle ψ. The black line depicts the force limit in the parametric study, based on the payload of the object. The red crosses depict the intersection points between the maximum force-thickness plot and the force limit, resulting in the ultimate combination for a value for h and ψ where the finger can hold the payload. The finger is made from stainless steel and has a width of 20 mm.

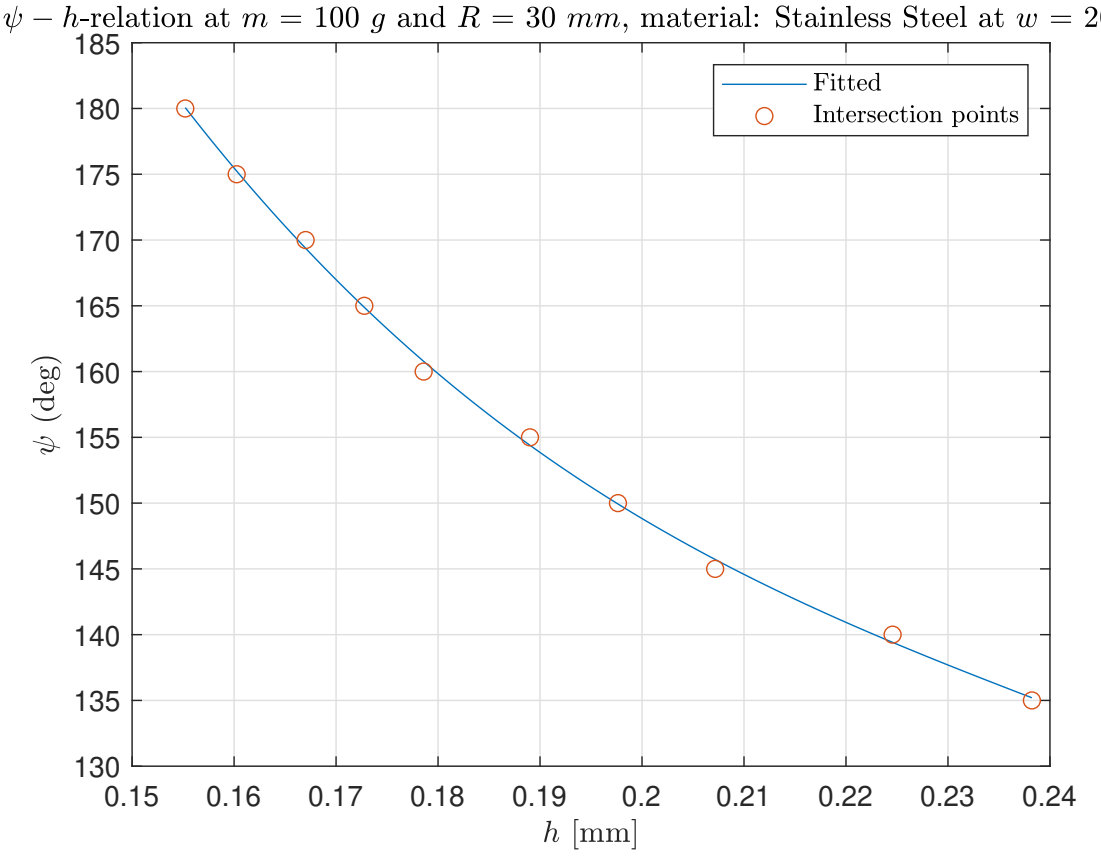

(b) Design chart: the relation between the enclosing angle and the finger thickness for a parametric sweep with stainless steel as chosen material. The circles represent the intersection points and the continuous line is the 3rd-degree fitted polynomial.

Figure H.3: Parametric study results and design chart for a stainless steel finger with a width of 20 mm.

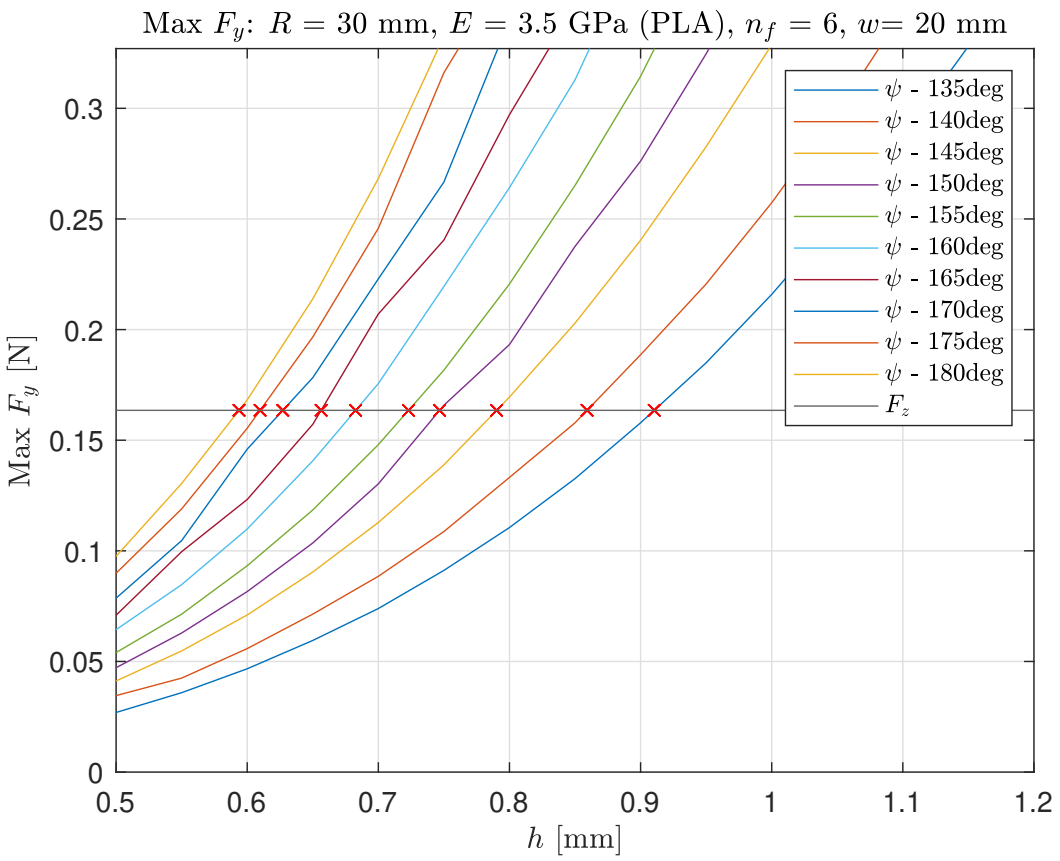

(a) Relation between the maximum pull-out force F_y and the thickness h, for ten different constant values of the enclosing angle ψ. The black line depicts the force limit in the parametric study, based on the payload of the object. The red crosses depict the intersection points between the maximum force-thickness plot and the force limit, resulting in the ultimate combination for a value for h and ψ where the finger can hold the payload. The finger is made from PLA and has a width of 20 mm.

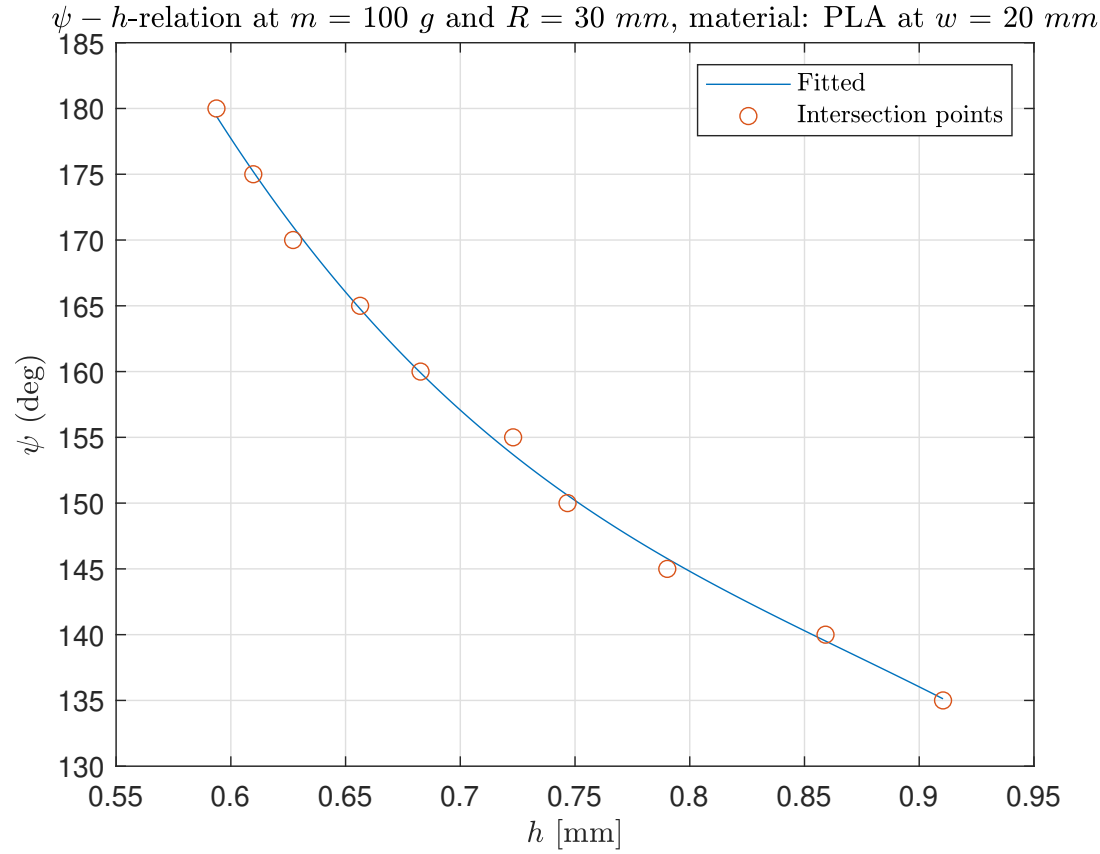

(b) Design chart: the relation between the enclosing angle and the finger thickness for a parametric sweep with PLA as chosen material. The circles represent the intersection points and the continuous line is the 3rd-degree fitted polynomial.

Figure H.4: Parametric study results and design chart for a PLA finger with a width of 20 mm.

I Extended application of model

I.1. Kinematics

To solve the kinematics of the extended application of the model, that is described in chapter 8 and depicted in Figure 8.2, the vector loop is defined in Figure I.1. This vector loop poses a circular traction of the inner tip of the double finger, using the outer length of the double finger as a constraint for the vector lengths, forcing the inner finger to change in length.

This results in the vector balance, as depicted in Equation I.1, where the vectors $\vec{\boldsymbol{r}}_2$, $\vec{\boldsymbol{r}}_3$ and $\vec{\boldsymbol{r}}_4$ follow the paths and directions of the finger links. Vector $\vec{\boldsymbol{r}}_5$ represents inner radius. Vector $\vec{\boldsymbol{r}}_6$ represents the displacement of the object in the y-direction. Vector $\vec{\boldsymbol{r}}_6$ represents the distance t between the inner and outer finger. The vector loop equations are depicted in Equation I.2, where c_i and s_i are substitutions for $\cos(\theta_i)$ and $\sin(\theta_i)$, respectively.

$$\vec{\boldsymbol{r}}_1 + \vec{\boldsymbol{r}}_2 + \vec{\boldsymbol{r}}_3 + \vec{\boldsymbol{r}}_4 = \vec{\boldsymbol{r}}_5 + \vec{\boldsymbol{r}}_6 + \vec{\boldsymbol{r}}_7 \tag{I.1}$$

$$\begin{cases} l_1 c_1 + l_2 c_2 + l_3 c_3 + l_4 c_4 - l_5 c_5 - l_6 c_6 - l_7 c_7 = 0 \\ l_1 s_1 + l_2 s_2 + l_3 s_3 + l_4 s_4 - l_5 s_5 - l_6 s_6 - l_7 c_7 = 0 \end{cases} \tag{I.2}$$

The lengths l_i and angles θ_i are defined as shown in Equation I.3.

$$l = \begin{cases} l_1 = \gamma_1 L_o \\ l_2 = \gamma_2 L_o \\ l_3 = \gamma_3 L_o \\ l_4 = \gamma_4 L_o \\ l_5 = R_i \\ l_6 = R_o + y \\ l_7 = t \end{cases} \qquad \theta = \begin{cases} \theta_1 = \zeta_1 \\ \theta_2 = \theta_1 + \zeta_2 + \delta\theta_2 \\ \theta_3 = \theta_2 + \zeta_3 + \delta\theta_3 \\ \theta_4 = \theta_3 + \zeta_4 + \delta\theta_4 \\ \theta_5 = \psi - \frac{\pi}{2} + \delta\theta_5 \\ \theta_6 = \frac{\pi}{2} \\ \theta_7 = \psi + \delta\theta_2 + \delta\theta_3 + \delta\theta_4 - \frac{\pi}{2} \end{cases} \tag{I.3}$$

I.2. Kinetics

To determine the stiffness of the torsion springs at the joints of the inner linkage the linkage lengths have to be determined. This is done by a kinematic relation, that is based on the definition of the trapezium. This is visualized in Figure I.2. In this figure the angles α_i for $i = 1, 2, 3, 4, 5$ are related and determined

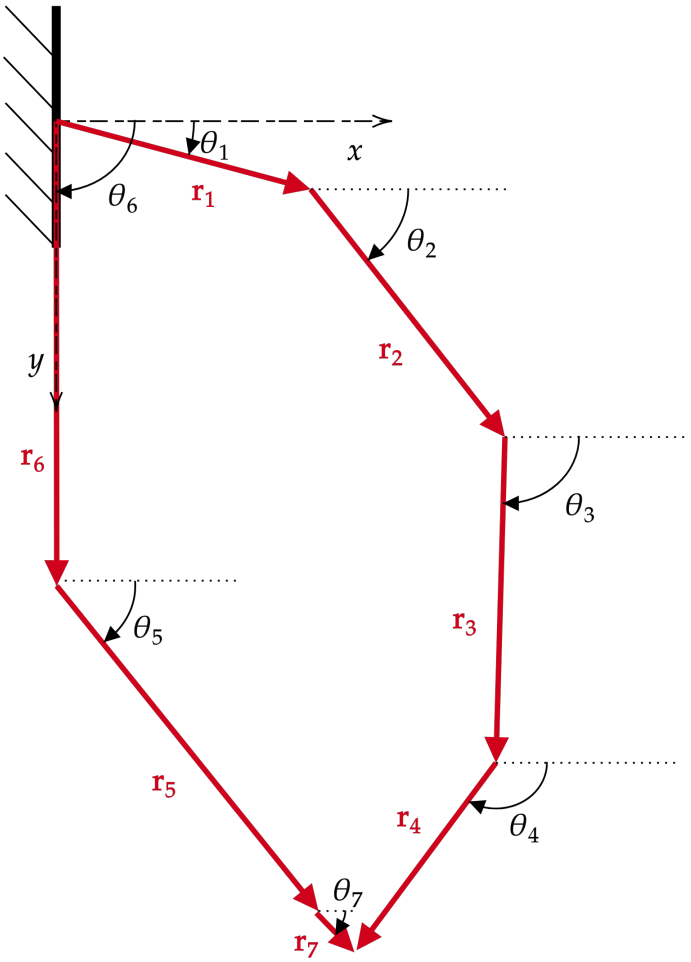

Figure I.1: Vector loop of the extended mechanism: the vectors $\vec{r}_2$, $\vec{r}_3$ and $\vec{r}_4$ follow the paths and directions of the finger links. Vector $\vec{r}_5$ represents inner radius. Vector $\vec{r}_6$ represents the displacement of the object in the y-direction. Vector $\vec{r}_6$ represents the distance t between the inner and outer finger.

in Equation I.4

$$\begin{cases} \alpha_1 = \frac{\pi}{2} - \zeta_1 \\ \alpha_2 = \pi - \alpha_1 - (\zeta_2 + \delta\theta_2) \\ \alpha_3 = \pi - \alpha_2 - (\zeta_3 + \delta\theta_3) \\ \alpha_4 = \pi - \alpha_3 - (\zeta_4 + \delta\theta_4) \\ \alpha_5 = \psi + \delta\theta_2 + \delta\theta_3 + \delta\theta_4 - \frac{\pi}{2} \end{cases} \tag{I.4}$$

The length of the segments of the inner linkage can then be determined by the relations depicted in Equation I.5

$$\begin{cases} l_{i1} = \gamma_1 L_o - t\cos(\alpha_1) \\ l_{i2} = \gamma_2 L_o - t\cos(\alpha_2) \\ l_{i3} = \gamma_3 L_o - t\cos(\alpha_3) \\ l_{i4} = \gamma_4 L_o - t\cos(\alpha_4) \end{cases} \tag{I.5}$$

The total arc length of the inner linkage is then determined by the same pseudo-lengths γ_i, where $i = 1, 2, 3, 4$, as for the outer linkage. This leads to the following relation for the inner arc length L_i, as depicted in Equation I.6.

$$L_i = \frac{l_{i1} + l_{i2} + l_{i3} + l_{i4}}{\gamma_1 + \gamma_2 + \gamma_3 + \gamma_4} \tag{I.6}$$

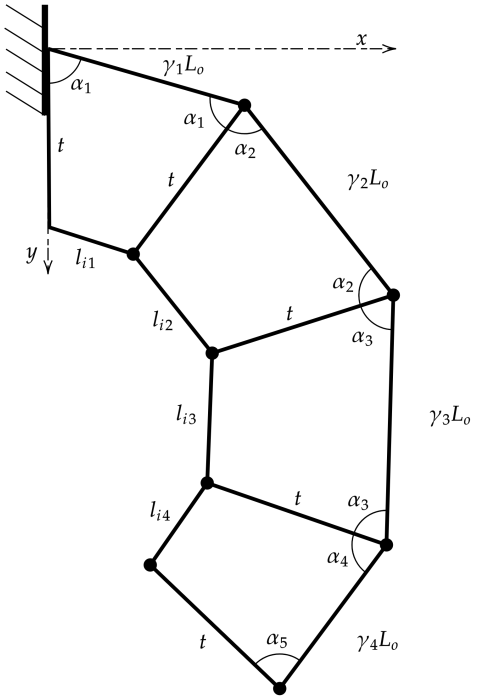

Figure I.2: Trapezium method to determine the inner link lengths based on the outer link lengths and the constraint of the width t between the linkages.

With these lengths the stiffness values of the torsion springs at the joints of the inner linkage can be calculated, as depicted in Equation I.7.

$$\begin{cases} K_{\theta 2i} = \frac{k_{\theta 2} EI}{L_i} \\ K_{\theta 3i} = \frac{k_{\theta 3} EI}{L_i} \\ K_{\theta 4i} = \frac{k_{\theta 4} EI}{L_i} \end{cases} \tag{I.7}$$

The total force can be calculated with the same method as described in chapter 4, but the stiffness $K_{\theta 4}$, that is used to determine the reaction moment of the fourth linkage T_4, has to be replaced with the combined stiffness values of the inner and outer linkage. This results in the force-deflection plots as depicted in Figure I.3. Here, F_x and F_y represent the x- and y-components of the total force F, F_x^i and F_y^i the components of the force due to the inner linkage, and F_x^o and F_y^o the components of the force due to the inner linkage. The total force F is therefore defined as depicted in Equation I.8.

$$F = \sqrt{F_x^2 + F_y^2} = \sqrt{(F_x^i + F_x^o)^2 + (F_y^i + F_y^o)^2} \tag{I.8}$$

I.3. MATLAB code adaptations

I.3.1. General parameters

```
%% Choose the thickness (h) and revolution angle (psi) of the finger & load parameters
E = 195E9;                      % Pa (Spring Steel)
h =  0.2/1000; % (thickness backbone)
t = 4/1000; % distance between backbones
psi = deg2rad(180); % deg
% Load in the main mechanism/environment parameters
% Beam - Material choice: PLA
w = 20/1000;                    % m
I = w*h.^3/12;                  % m^4 --> design freedom

% Tomato parameters and force due to the weight of tomato.
```

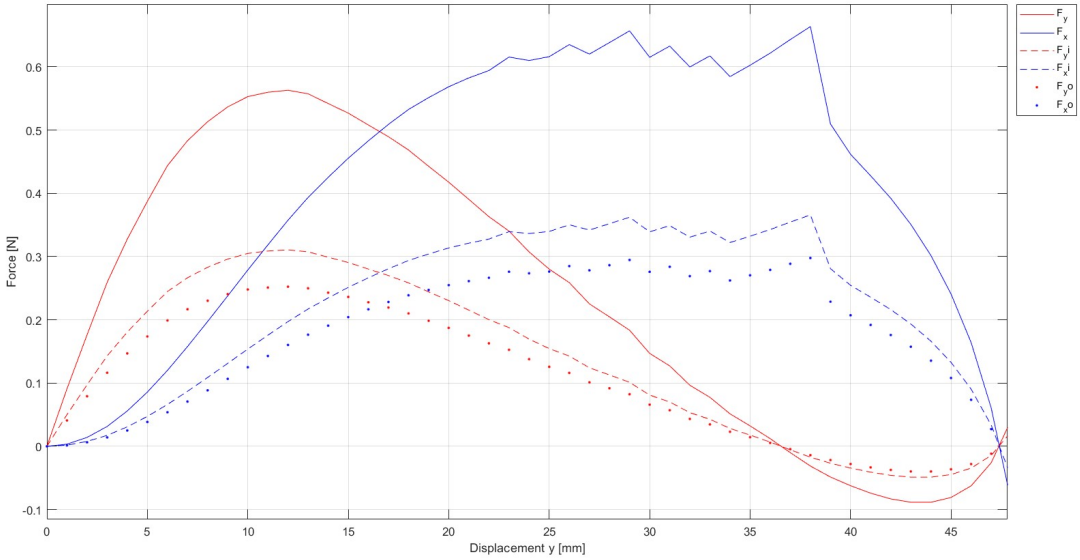

Figure I.3: Force-deflection plot of the simulation of the extended design. The continuous line depicts the total force in the x- and y-direction (F_x and F_y), the dashed line depicts the force contribution of the inner linkage in the x- and y-direction (F_x^i) and (F_y^i), and the dotted line the force contribution of the outer linkage in the x- and y-direction (F_x^o) and (F_y^o).

```
D_tomato = 0.06; % m
R_i = D_tomato/2;
R_o = D_tomato/2+t;
L_o = psi*R_o;  % Length outer backbone
PRBMParameters2; % Load in the parameters (gamma, zeta etc.) from the 3R PRBM method
```

In the subcode PRBMParameters2.m the calculation for the stiffness values is therefore also changed:

```
% Stiffness values
K_theta2 = k_theta2*E*I/L_o;
K_theta3 = k_theta3*E*I/L_o;
K_theta4 = k_theta4*E*I/L_o;
```

I.3.2. VectorLoopValues2.m

```
% Initial positions
theta1_0 = zeta_1;
theta2_0 = zeta_1+zeta_2;
theta3_0 = zeta_1+zeta_2+zeta_3;
theta4_0 = zeta_1+zeta_2+zeta_3+zeta_4;
theta_tip_0 = psi;
theta5_0 = theta_tip_0-deg2rad(90);
theta6_0 = deg2rad(90);
theta7_0 = psi-deg2rad(90);

theta_0 = [theta1_0 theta2_0 theta3_0 theta4_0 theta5_0 theta6_0 theta7_0];

% Vector lengths
L1 = gamma_1*L_o;
L2 = gamma_2*L_o;
L3 = gamma_3*L_o;
L4 = gamma_4*L_o;
L5 = R_i;
L6_0 = R_o;
L7 = t;

% Plot initial vector loop
origin = [0;0];
r1_0 = [L1*cos(theta1_0); L1*sin(theta1_0)];
```

```
r2_0 = [L2*cos(theta2_0); L2*sin(theta2_0)];
r3_0 = [L3*cos(theta3_0); L3*sin(theta3_0)];
r4_0 = [L4*cos(theta4_0); L4*sin(theta4_0)];
r5_0 = [L5*cos(theta5_0); L5*sin(theta5_0)];
r6_0 = [L6_0*cos(theta6_0); L6_0*sin(theta6_0)];
r7_0 = [L7*cos(theta7_0); L7*sin(theta7_0)];

alpha  = linspace(0,360,361)           ;
Circle_x     = R_i*cosd(alpha)   ;
Circle_y0     = R_i*sind(alpha) + L6_0 ;

loop_ccw = [origin r1_0 r1_0+r2_0 r1_0+r2_0+r3_0 r1_0+r2_0+r3_0+r4_0];
loop_cw = [origin r6_0 r6_0+r5_0 r6_0+r5_0+r7_0];
% figure('Name','Initial Vector Loop')
plot(Circle_x, Circle_y0, 'k--')
hold on
plot(loop_ccw(1,:),loop_ccw(2,:), 'r')
plot(loop_cw(1,:),loop_cw(2,:), 'r')
axis equal
```

I.3.3. Optimization section

In the optimization section, the seventh link and corresponding angles have to be added, the sixth link of the vector loop has to be determined by the outer radius R_o and the adjusted functions for the objective (ObjPE3.m), and the vector loop equations (vectorloopequation3.m) have to be replaced. Furthermore, the kinematic results caused by the seventh link have to be added in the subcode for the data storage (DataStorage2.m).

```
%% Optimization problem
nms = 1;

dy = 0.001;
y_start = 0;
y_end = 2*R_o;
y = y_start:dy:y_end;

dtheta = deg2rad([0 0 0 0 0 0 0]);
dtheta1 = dtheta(1);
dtheta2 = dtheta(2);
dtheta3 = dtheta(3);
dtheta4 = dtheta(4);
dtheta5 = dtheta(5);
dtheta6 = dtheta(6);
dtheta7 = dtheta(7);

for i = 1:length(y)
% Initial values
x0 = [dtheta2 dtheta5];
x0_i(:,i) = x0
dtheta34_0 = [dtheta3 dtheta4];
dtheta34_0i(:,i) = dtheta34_0
% lb = x0+deg2rad([-2 -5]);
% ub = x0+deg2rad([2 5]);
lb = x0 + 1000*dy*deg2rad([-2 -15]);
ub = x0 + 1000*dy*deg2rad([2 15]);
L6 = R_o+y(i);
L6_i(i) = L6;

% Find min PE
objective = @(x)ObjPE3 (x,dtheta34_0,theta_0,L1,L2,L3,L4,L5,L6,L7,K_theta2,K_theta3,K_theta4)
    ;

% MultiStart Optimizer:
ms = MultiStart('Display','off');
options=optimset('Algorithm','interior-point','GradObj','off','Hessian','off','tolX',1e-10,'
    TolFun',1e-10,'MaxIter',100,'MaxFunEvals',10000);
problem = createOptimProblem('fmincon','x0',x0,'lb',lb,'ub',ub,'Aeq',[],'beq',[],'nonlcon'
    ,[],'objective',objective,'options',options);
[x,fval,exitflag,output,solutions] = run(ms,problem,nms);

```

```
dtheta2 = x(1);
dtheta5 = x(2);

% calculate mechanism angles
fun = @(dtheta34)vectorloopequation3(dtheta34,dtheta2,dtheta5,theta_0,L1,L2,L3,L4,L5,L6,L7);

[dtheta34] = fsolve(fun,dtheta34_0);
dtheta3 = dtheta34(1);
dtheta4 = dtheta34(2);

DataStorage2;
end
```

I.3.4. ObjPE3.m

```
function pe = ObjPE3(x,dtheta34_0,theta_0,L1,L2,L3,L4,L5,L6,L7,K_theta2,K_theta3,K_theta4)

% Objective variable: theta_5
dtheta2 = x(1);
dtheta5 = x(2);

% kinematic equations
options = optimset('Display','off');
fun2 = @(dtheta34)vectorloopequation3(dtheta34,dtheta2,dtheta5,theta_0,L1,L2,L3,L4,L5,L6,L7);
[dtheta34] = fsolve(fun2,dtheta34_0,options);

dtheta3 = dtheta34(1);
dtheta4 = dtheta34(2);

pe = 0.5*K_theta2*dtheta2^2+0.5*K_theta3*dtheta3^2+0.5*K_theta4*dtheta4^2;
```

I.3.5. vectorloopequation3.m

```
function F = vectorloopequation3(dtheta34,dtheta2,dtheta5,theta_0,L1,L2,L3,L4,L5,L6,L7)
% VECTOR LOOP EQUATION
%   F(1) and F(2) are based on the vector loop.
F(1) = L1*cos(theta_0(1))+L2*cos(theta_0(2)+dtheta2)+L3*cos(theta_0(3)+dtheta2+dtheta34(1))+
    L4*cos(theta_0(4)+dtheta2+dtheta34(1)+dtheta34(2))-L5*cos(theta_0(5)+dtheta5)-L7*cos(
    theta_0(7)+dtheta2+dtheta34(1)+dtheta34(2));
F(2) = L1*sin(theta_0(1))+L2*sin(theta_0(2)+dtheta2)+L3*sin(theta_0(3)+dtheta2+dtheta34(1))+
    L4*sin(theta_0(4)+dtheta2+dtheta34(1)+dtheta34(2))-L5*sin(theta_0(5)+dtheta5)-L6-L7*sin(
    theta_0(7)+dtheta2+dtheta34(1)+dtheta34(2));
end
```

I.3.6. DataStorage2.m

```
Data(i,1) = rad2deg(dtheta1);
Data(i,2) = rad2deg(x(1));
Data(i,3) = rad2deg(dtheta34(1));
Data(i,4) = rad2deg(dtheta34(2));
Data(i,5) = rad2deg(x(2));
Data(i,6) = rad2deg(dtheta6);
Data(i,7) = rad2deg(dtheta7);
%dy
Data(i,8) = L6;
Data(i,9) = 1000*L6; % scaled dataset
```

I.3.7. Determining inner lengths with trapezium method

```
%% Lengths inner linkage
a_1 = ones(length(deg2rad(Data(:,2))),1)*(pi/2)-zeta_1;
a_2 = pi-a_1-(zeta_2+deg2rad(Data(:,2)));
a_3 = pi-a_2-(zeta_3+deg2rad(Data(:,3)));
a_4 = pi-a_3-(zeta_4+deg2rad(Data(:,4)));
a_5 = (pi/2)-(psi+deg2rad(Data(:,2))+deg2rad(Data(:,3))+deg2rad(Data(:,4)));

l1o = gamma_1*L_o;
l2o = gamma_2*L_o;
l3o = gamma_3*L_o;
```

```
l4o = gamma_4*L_o;

l1i = l1o - 2*t.*cos(a_1);
l2i = l2o - 2*t.*cos(a_2);
l3i = l3o - 2*t.*cos(a_3);
l4i = l4o - t.*cos(a_4)-t.*cos(a_5);

li = l1i+l2i+l3i+l4i;
lo = L_o/(gamma_1+gamma_2+gamma_3+gamma_4);
L_i = li*(gamma_1+gamma_2+gamma_3+gamma_4);
```

I.3.8. Kinetics

```
%% Kinetics
K_theta2i = k_theta2*E*I./L_i
K_theta3i = k_theta3*E*I./L_i
K_theta4i = k_theta4*E*I./L_i
K_theta4o = k_theta4*E*I./L_o

T4i = K_theta4i.*deg2rad(Data(:,4))
T4o = K_theta4o.*deg2rad(Data(:,4))
T4 = T4i+T4o
figure()
plot(y,T4o)
hold on
plot(y,T4i)
plot(y,T4)

omega = theta_0(5)+deg2rad(Data(:,5))
omega3 = deg2rad(180)-(zeta_1+zeta_2+zeta_3+zeta_4+deg2rad(Data(:,2)+Data(:,3)+Data(:,4)))

X = L_o*gamma_4*cos(omega3)
Y = L_o*gamma_4*sin(omega3)

F = T4./(-Y.*cos(omega)-X.*sin(omega))
Fi = T4i./(-Y.*cos(omega)-X.*sin(omega))
Fo = T4o./(-Y.*cos(omega)-X.*sin(omega))
Fx = F.*cos(omega)
Fy = F.*sin(omega)
Fxi = Fi.*cos(omega)
Fyi = Fi.*sin(omega)
Fxo = Fo.*cos(omega)
Fyo = Fo.*sin(omega)
%%
figure()
plot(Data(:,9)-1000*R_o,Fy, 'r')
% hold on
hold on
plot(Data(:,9)-1000*R_o,Fx, 'b')
plot(Data(:,9)-1000*R_o,Fyi, 'r--')
plot(Data(:,9)-1000*R_o,Fxi, 'b--')
plot(Data(:,9)-1000*R_o,Fyo, 'r.')
plot(Data(:,9)-1000*R_o,Fxo, 'b.')
legend("F_y",'F_x',"F_yi",'F_xi',"F_yo",'F_xo', 'Location','northeastoutside')
xlabel('Displacement y [mm]'), ylabel('Force [N]')
ylim([0 1.1*max(double(Fx))])
grid on
```

I.3.9. VisualPlotResult2.m

```
%% Initial positions
figure('Name', '3R plot')

n = [1:1:length(Data(:,2))]

for i2 = 1:length(n)
n0 = n(i2);

theta1 = theta_0(1)+deg2rad(Data(n0,1));
theta2 = theta_0(2)+deg2rad(Data(n0,2));
```

```
theta3 = theta_0(3)+deg2rad(Data(n0,2))+deg2rad(Data(n0,3));
theta4 = theta_0(4)+deg2rad(Data(n0,2))+deg2rad(Data(n0,3))+deg2rad(Data(n0,4));
theta5 = theta_0(5)+deg2rad(Data(n0,5));
theta6 = theta_0(6)+deg2rad(Data(n0,6));
theta7 = theta_0(7)+deg2rad(Data(n0,2))+deg2rad(Data(n0,3))+deg2rad(Data(n0,4));
theta = [theta1 theta2 theta3 theta4 theta5 theta6 theta7];

% Vector lengths
L1 = gamma_1*L_o;
L2 = gamma_2*L_o;
L3 = gamma_3*L_o;
L4 = gamma_4*L_o;
L5 = R_i;
L6 = Data(n0,8);
L7 = t;

L1i = l1i(i2);
L2i = l2i(i2);
L3i = l3i(i2);
L4i = l4i(i2);

alpha  = linspace(0,360,361)           ;
Circle_x     = R_o*cosd(alpha)   ;
Circle_y     = R_o*sind(alpha) + L6 ;
Circle_xi     = R_i*cosd(alpha)   ;
Circle_yi     = R_i*sind(alpha) + L6 ;
% Plot initial vector loop
origin = [0;0];
r1 = [L1*cos(theta1); L1*sin(theta1)];
r2 = [L2*cos(theta2); L2*sin(theta2)];
r3 = [L3*cos(theta3); L3*sin(theta3)];
r4 = [L4*cos(theta4); L4*sin(theta4)];
r5 = [L5*cos(theta5); L5*sin(theta5)];
r6 = [L6*cos(theta6); L6*sin(theta6)];
r7 = [L7*cos(theta7); L7*sin(theta7)];

origin_2 = [0;t];
r1i = [L1i*cos(theta1); L1i*sin(theta1)+t];
r2i = [L2i*cos(theta2); L2i*sin(theta2)];
r3i = [L3i*cos(theta3); L3i*sin(theta3)];
r4i = [L4i*cos(theta4); L4i*sin(theta4)];

loop_ccw = [origin r1 r1+r2 r1+r2+r3 r1+r2+r3+r4];
loop_ccwi = [origin_2 r1i r1i+r2i r1i+r2i+r3i r1i+r2i+r3i+r4i r1+r2+r3+r4 ];

loop_cw = [origin r6 r6+r5 r6+r5+r7];
loop_ccwmin = -loop_ccw;

plot(Circle_x, Circle_y, 'k--')
hold on
plot(Circle_xi, Circle_yi, 'k--')
plot(loop_ccw(1,:),loop_ccw(2,:), 'r')
%plot(loop_ccwmin(1,:),loop_ccw(2,:), 'r')
plot(loop_cw(1,:),loop_cw(2,:), 'r')
plot(loop_ccwi(1,:),loop_ccwi(2,:), 'r')
axis([-2*R_o 2*R_o 0 3*R_o])

hold off

H(i2) = getframe(gcf) ;
drawnow
pause(0.2)
end

% create the video writer with 1 fps
  writerObj = VideoWriter('myVideo2.avi');
  writerObj.FrameRate = 10;
  % set the seconds per image
% open the video writer
open(writerObj);
% write the frames to the video
```

```
for ix=1:length(H)
    % convert the image to a frame
    frame = H(ix) ;
    writeVideo(writerObj, frame);
end
% close the writer object
close(writerObj);
```

J

Technical Drawings

In this appendix, the technical drawings of the final prototype are presented.

1. Figure J.1 shows the dimensions of the laser cutter file for the stainless steel fingers.
2. Figure J.2 shows the dimensions of the finger hull, which encapsulates the bent fingers.
3. Figure J.3 shows the dimensions of the top plate of the finger hull, which closes the finger hull when fully assembled.
4. Figure J.4 shows the dimensions of the coupling parts that connect the finger hulls to each other.
5. Figure J.5 shows the dimensions of the triangular-shaped part which connects to the stainless steel fingers and provides actuation of the gripper.

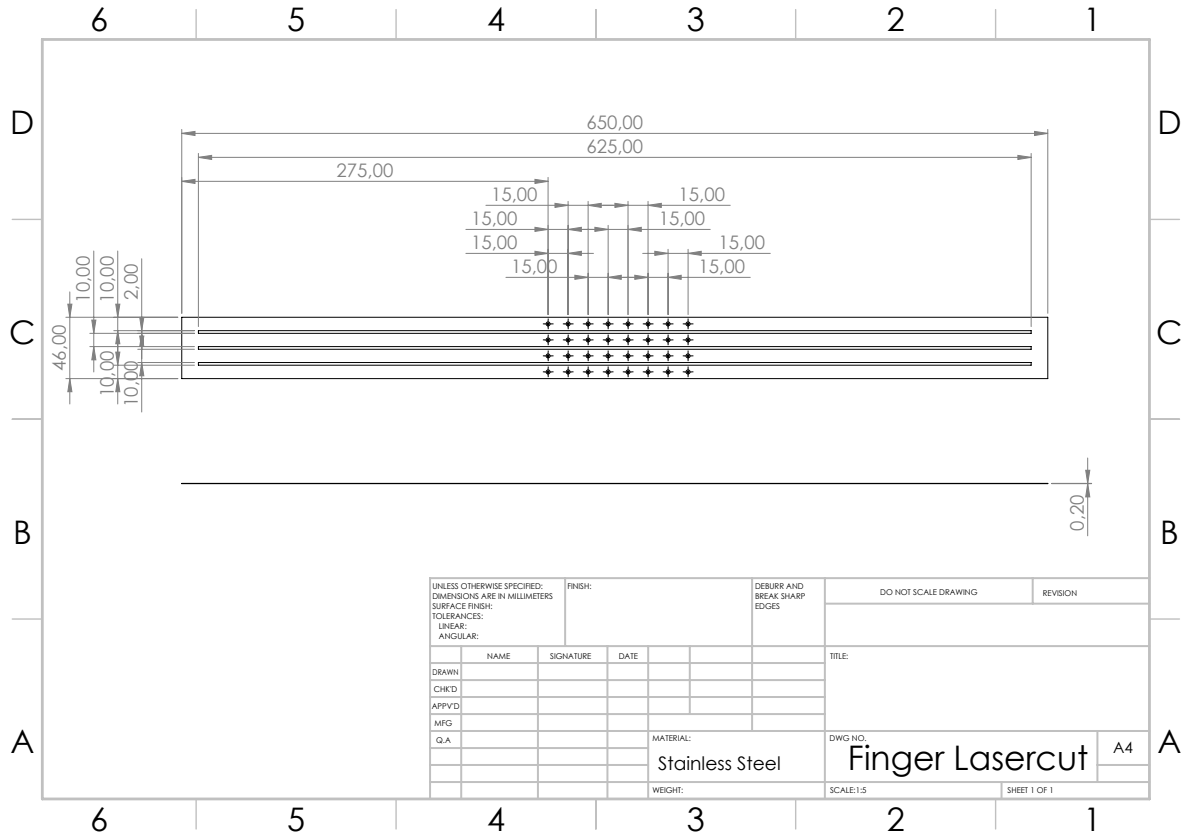

Figure J.1: Dimensions of the laser cutter file for the stainless steel fingers.

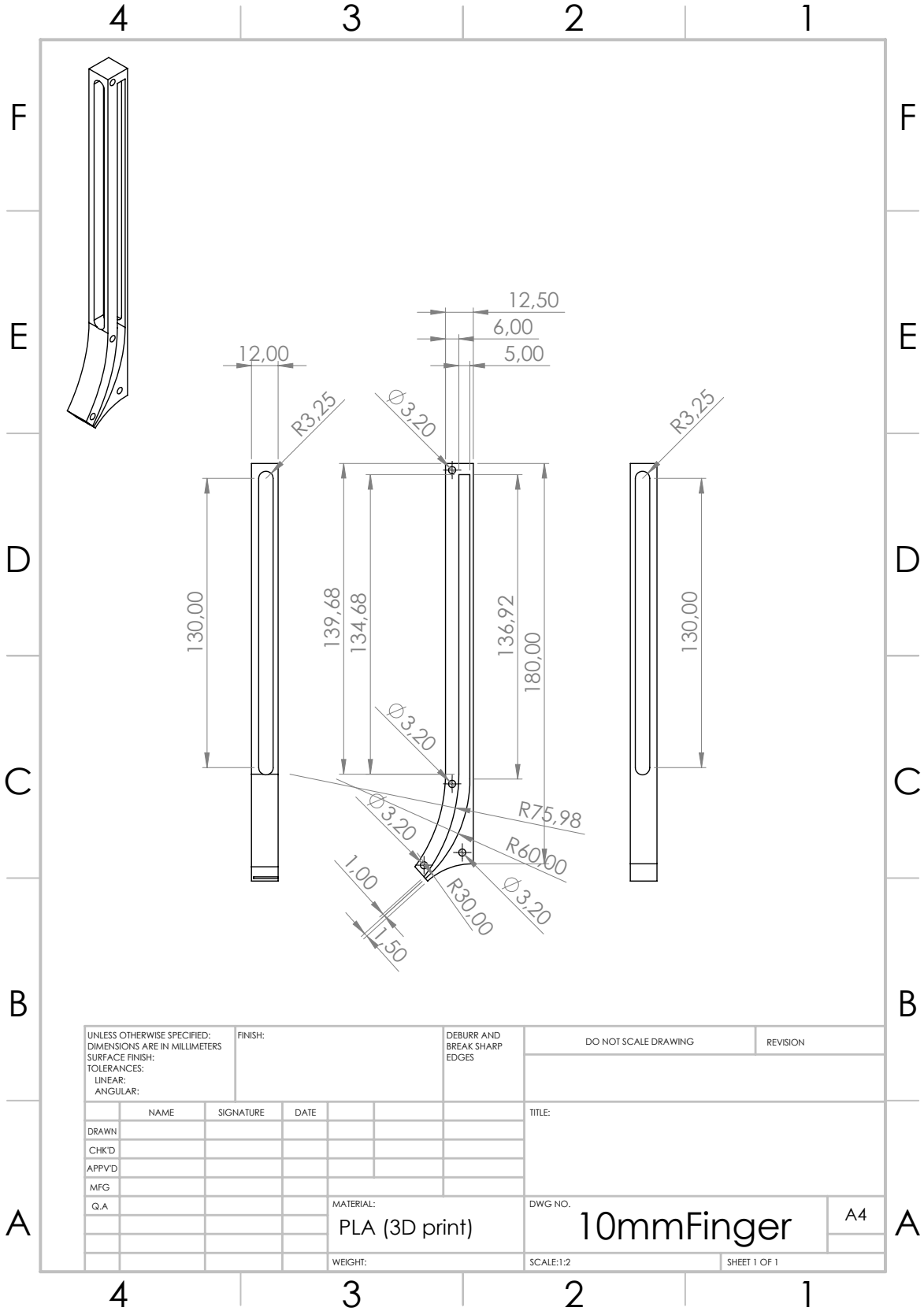

Figure J.2: Dimensions of the finger hull.

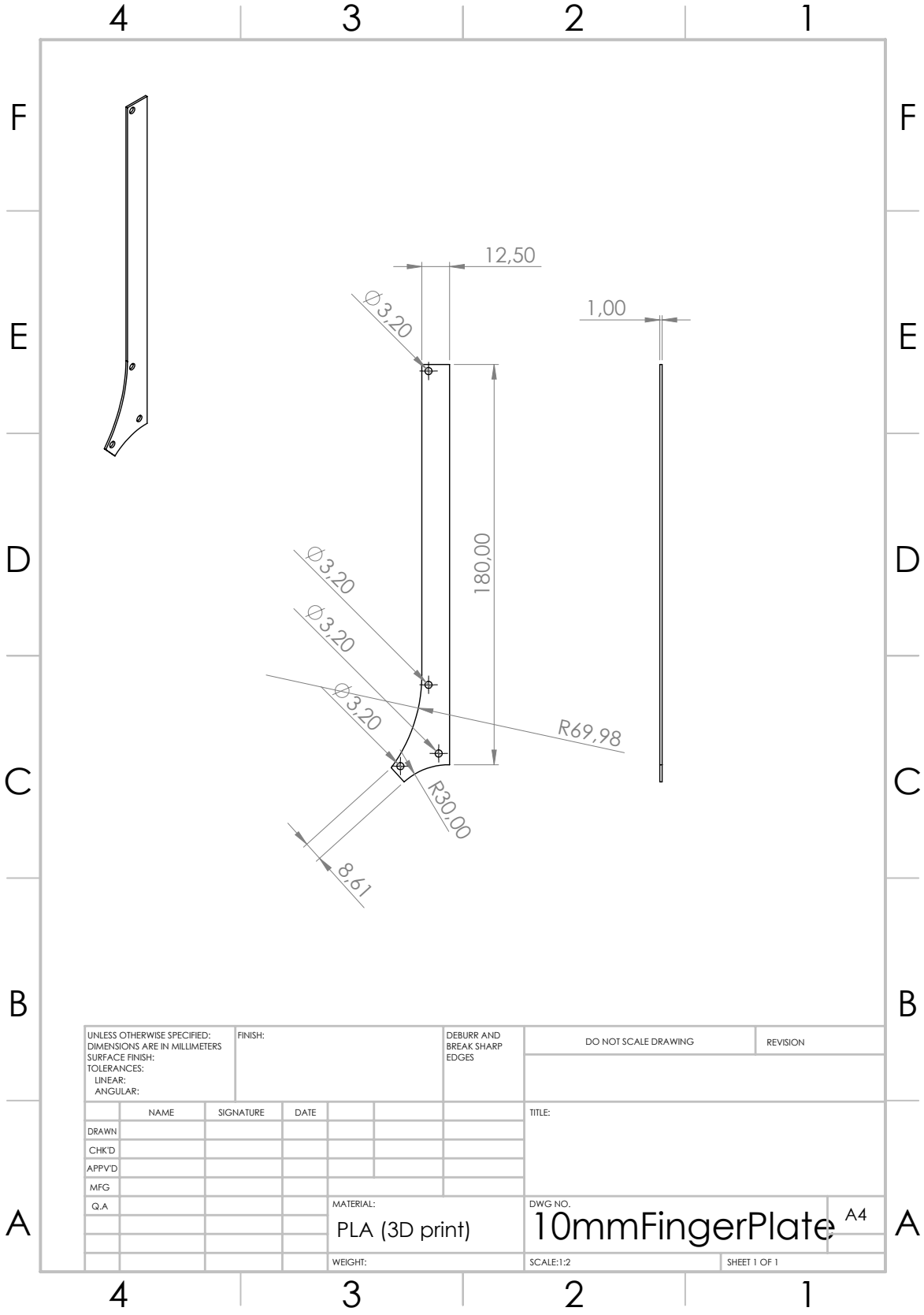

Figure J.3: Dimensions of the plate of the finger hull.

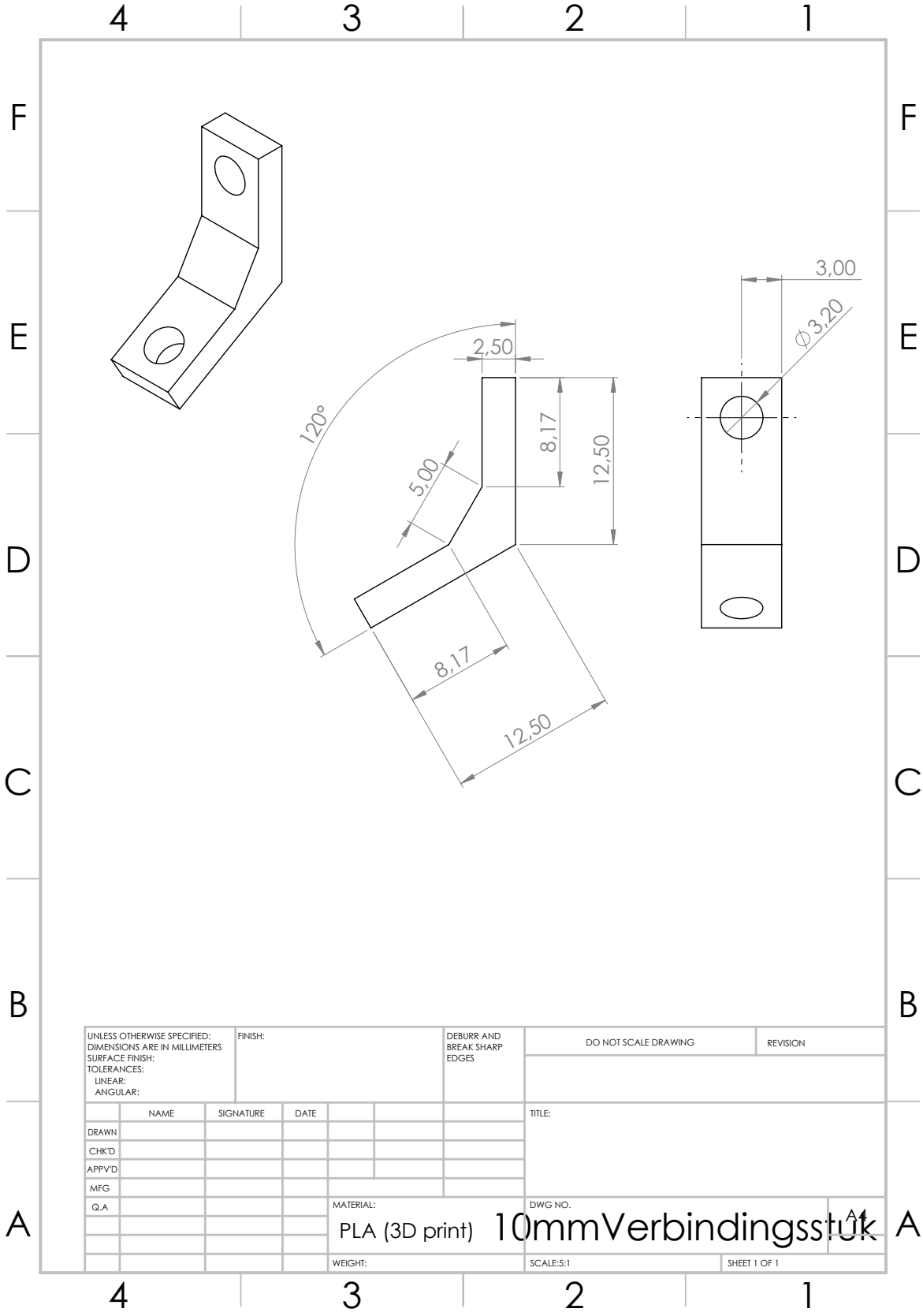

Figure J.4: Dimensions of the couple part of the gripper.

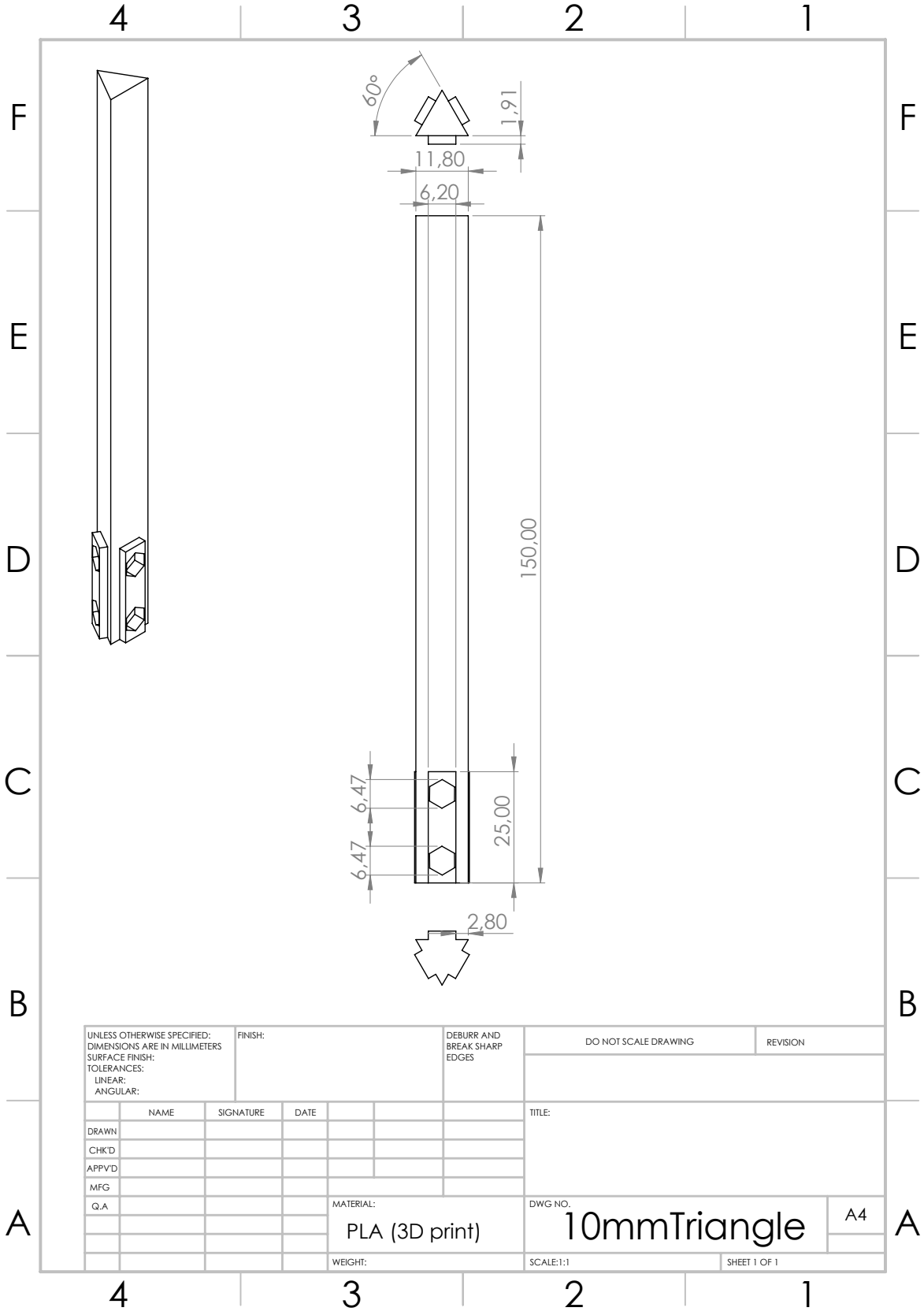

Figure J.5: Dimension of the triangle part of the gripper.

Pull-out force of grippers with initially-curved fingers based on Pseudo-Rigid Body modelling

M. H. Kuntz
Department of Precision and Microsystems Engineering
Delft University of Technology
Delft, The Netherlands

***Abstract*—This paper presents the implementation and extension of an existing Pseudo-Rigid Body Modelling (PRBM) method for modelling initially-curved compliant grippers out of which a circular object is extracted. The goal of this paper is to present and validate the pull-out force modelling for these fingers within defined load conditions to provide comprehensive insights into the relation between important design parameters, such as the enclosing angle and thickness of the finger. This goal is accomplished by extending an existing 3R PRB-model for initially-curved beams with a fifth link that represents the object and analysing the kinematics and kinetics to determine the relation for the pull-out force of a gripper finger with defined dimensions and a known load case. This model is validated with an experimental test setup and errors for the kinetics between 12 and 32 percent were determined, consisting primarily of systematic errors. The validated model is used for a parametric study, where relations between relevant design parameters, such as the enclosing angle and thickness of an initially-curved compliant gripper finger, are determined and visualized in a design chart that can be applied in gripper design.**

I. Introduction

The agri-food industry is undergoing rapid technological advancements, particularly in the domain of automated food grasping and distribution, aiming to enhance efficiency, hygiene, and safety. The development of grippers for grasping robots is one of the big challenges in this automation topic, as the agri-food industry contains objects that are hard to grasp due to their changing geometry, hard-to-reach locations, slippery surfaces, and fragility. Therefore, it is important to design grippers that provide low damage to the object and environment while functioning in cluttered environments.

Several types of grippers exist, such as force-closed grippers, utilizing principles such as suction [1], [2], adhesion [3], [4] or clamping [5], [6], and form-closed grippers [7], often implemented in a finger that encompasses the object, holding it by its structural stiffness. These fingers can comprise rigid linkages, soft robotic bellows or be a compliant mechanism [8], [9]. The latter gain their motion from elastic deformation and are therefore gaining popularity as scientists see the advantages of these mechanisms, such as the use of monolithic mechanisms, that eliminate the use of lubrication and minimize wear, simplified manufacturing, which reduces cost and weight, high performance, which increases precision and shape-adaptive abilities, which reduce the high force peaks and therefore minimize damage. Compliant mechanisms are found in several gripper designs, such as the fin ray gripper [10], topology optimized structures [11] and initially-curved fingers [12]. The latter is very suitable for agri-food grippers, as they encompass the object without applying force on the surface. Therefore, they are suitable for grasping fragile objects in a cluttered environment. Strategies to further reduce undesirable forces to the object and environment include using the principle of zero-slip in design, such as the implementation of eversion mechanisms [13]–[16], and sleeve mechanics [17]–[23] to reduce traction at the surface of the object and their surrounding environment.

However, the main challenge of incorporating the existing initially-curved gripper technology is that the pull-out force for an initially-curved finger with a defined enclosing angle and thickness is unknown beforehand. Knowing the pull-out force is crucial to evaluate the performance of the gripper, as it is a measure of the maximum payload of a gripper before an object escapes the fingers. Essential design parameters, such as the enclosing angle and thickness of the gripper finger, directly influence the pull-out force and therefore exert a substantial influence on the evaluation of performance metrics during the generation of concepts for comprehensive gripper designs.

Therefore, the goal of this study is to present and validate the pull-out force modelling for an initially-curved gripper with a specified enclosing angle and thickness within defined load conditions to provide insightful comprehension of these critical design parameters in compliant gripper design, through a parametric study.

To reach this goal, a model-based approach will be adopted, in which pseudo-rigid body modeling (PRBM) is used as the foundational framework, which will be implemented such that it applies to compliant gripper design. PRB-modelling offers advantages over other modeling methods, as it is parametric-based and enables rapid and accurate computations of complex non-linear force-deflection behavior, making it suitable for parameter-based conceptual design [24].
Existing PRB models [25], [26], where large deformations

for different types of beams are described, such as initially curved beams [27], offer a suitable foundation for this model-based approach. However, implementing these models for pull-out force modelling is challenging, as these models often determine the kinematics of a mechanism by applying a load to the mechanism, while when applying these models to gripper design, the force is the variable that has to be determined due to the extraction of an object that deforms the mechanism. An existing PRB-model, specifically designed for analyzing the kinematics and kinetics associated with extracting a spherical object from initially-curved gripper fingers, will be implemented, by modelling the motion of the object as a fifth rigid link connected to the tip of the pseudolinkage. The model is developed for a spherical object, modelled as a planar disk, that is extracted from a gripper with initially-curved fingers, that encapsulate the object, while assuming frictionless contact. Due to the parametric-based nature of PRB methods, this implementation enables the evaluation of crucial design parameters through a parametric study. The parametric study is conducted for fingers made of polylactic acid (PLA) and stainless steel materials, comparing the thickness and enclosing angle of the finger for a specified load case, resulting in insightful design charts.

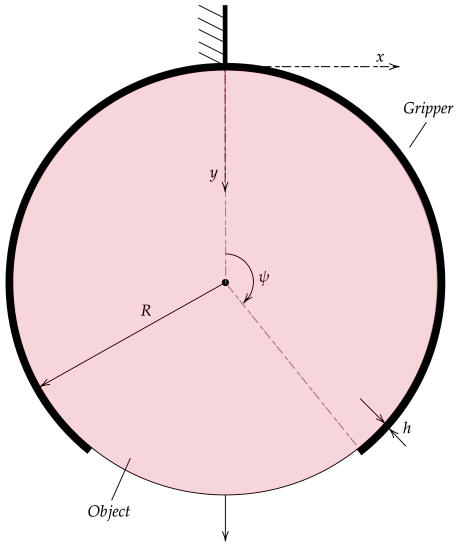

Fig. 1: Problem definition: a gripper with two initially-curved fingers with thickness h and enclosing angle ψ out of which a circular object with radius R is extracted.

The paper is organized as follows. First, in section II, the model is presented as well as the steps that are required to derive the relation for the pull-out force of an initially curved finger by solving the kinematics using vector loop equations and an optimization algorithm. Following this, in section III, the experimental set-up that has been built for validating the model and accuracy assessment is presented. In section IV, the additional steps that are required to perform the parametric study are presented. Following, in section V, the results of the experimental validation and the parametric study are presented. Subsequently, in section VI, a comprehensive discussion of the results and method is given, as well as suggestions for future research. Finally, in section VII, the conclusions of this paper are presented.

II. Methodology

A. Model definitions

The problem in this case study is defined as a gripper with initially-curved fingers with enclosing angle ψ and thickness h out of which a spherical object with radius R and mass m is extracted, as depicted in Figure 1. The inner radius of the fingers is equal to the radius of the object, hence encompassing the object and holding it solely by its structural stiffness and therefore preventing any additional clamping forces. The arc length L of the mechanism is defined as $L = \psi R$. Furthermore, the mechanism has a rectangular cross-section with width w and thickness h, and therefore the second moment of inertia of this cross-section is defined as $I = \frac{wh^3}{12}$. The pull-out force is defined as the y-component of the total reaction force F of a spherical object on the tip of the compliant initially-curved mechanism, that changes as the object is extracted from the mechanism. In this problem, only extraction of the object in the y-direction is considered.

In Figure 2 the Pseudo-Rigid Body model (PRBM) is presented as defined by K. Venkiteswaran [27], which is used as the foundation of the modeling methodology in this paper. Due to the symmetry of the fingers, only a single finger is considered that has frictionless contact with the object at the fingertip. In the model, this finger is replaced by a pseudo-rigid linkage equipped with three torsion springs at the revolute joints. The end of the linkage traces the location of the tip of the actual flexure during deflection and the torsion springs approximate the structural bending stiffness of the finger. The reaction force F between the object and the fingertip has an angle ϕ on the fingertip relative to the x-axis. In this study no moments are present.

The mechanism in the undeformed state is presented in Figure 2a. The mechanism is defined by the link lengths l_1, l_2, l_3 and l_4 and by the initial angles ζ_1, ζ_2, ζ_3 and ζ_4. The length of each segment of the PRB-linkage is defined by $\gamma_i L$, where γ_i represents the pseudo-length for $i = 1, 2, 3, 4$. The initial angle of the first link ζ_1 is defined relative to the x-axis. The initial angle of the remaining three links is defined as the angle relative to the direction of the previous link.

The stiffness of fingers is modelled by applying torsion springs at the joints of the pseudo-linkage. These torsion springs have stiffness $K_{\theta 2}$, $K_{\theta 3}$ and $K_{\theta 4}$ for the three joints, which is determined by the relation as given in Equation 1.

$$K_{\theta i} = k_{\theta i} \frac{EI}{L}, \quad i = 2, 3, 4 \tag{1}$$

In this relation the constant $k_{\theta i}$ represents the pseudo-stiffness of each joint. The values of γ_i, ζ_i and $k_{\theta i}$ are determined by definitions that are given in the paper from K. Venkiteswaran [27] and change when the curvature, e.g. the enclosing angle, changes.

Several assumptions in the model are made, that simplify the relation between several PRB values.
First, the model is defined to be symmetric about the second, central joint and therefore the pseudo-lengths γ_1 and γ_4 are equal, the pseudo-lengths γ_2 and γ_3 are equal and the pseudo-stiffness $k_{\theta 2}$ is equal to $k_{\theta 4}$.
Furthermore, a cantilever support of the mechanism is assumed, which results in the simplification that the first link will not deform. The remaining three links will deform. The angles of deformation are depicted by $\delta\theta_2$, $\delta\theta_3$ and $\delta\theta_4$ as can be seen in Figure 2b, where a schematic of the deformed PRB mechanism is given. The deformation angles are defined relative to the initial angles of each link.

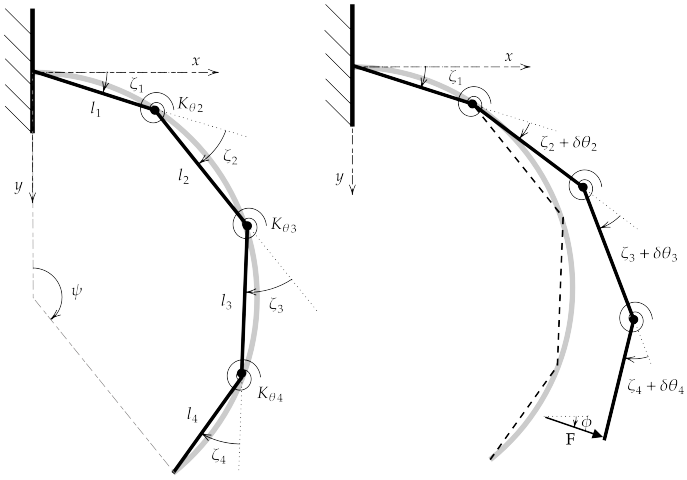

(a) Undeformed state (b) Deformed state

Fig. 2: Model definition: a Pseudo-Rigid Body model with four linkages and three torsion springs at the joints, depicted in the undeformed and deformed state. When a force F is applied at the tip, the linkage deforms.

The existing model is suitable for finding the position of a compliant mechanism under the influence of a specified load and direction applied at the tip. However, in the case of an object being extracted from a mechanism, such as in a gripper configuration, the magnitude and direction of the force are unknown. Moreover, the direction of the force changes as the object descends through the fingers during the opening of the gripper, influenced by the load of the object.

To make the method applicable for this use case, a fifth link is pinned in series to the pseudo-linkage and a joint on a slider to simulate the motion of the object, as shown in Figure 3. This motion is obtained by incrementally displacing the slider in the y-direction, resulting in the deformation of the pseudo-linkage. The link has a length l_5, which is equal to R, the radius of the object. This configuration allows the tip of the linkage to trace the circular path of the surface of the object and rotate freely at the contact point.

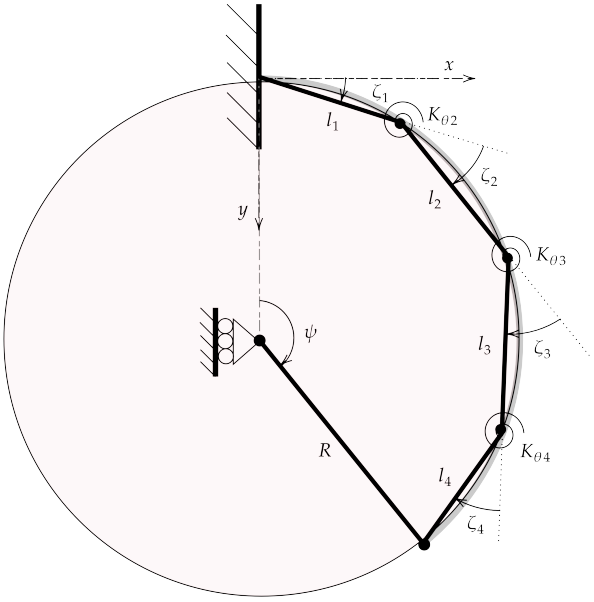

Fig. 3: Model extension: adding a fifth link with radius R in series to the existing linkage to a joint on a slider to mimic the displacement of an object in the y-direction.

B. Kinematics

The kinematic analysis of the linkage is performed using the vector loop, as depicted in Figure 4. In this vector loop $\vec{\boldsymbol{r}}_1$, $\vec{\boldsymbol{r}}_2$, $\vec{\boldsymbol{r}}_3$ and $\vec{\boldsymbol{r}}_4$ are the vectors following the paths and directions of the finger links. Vector $\vec{\boldsymbol{r}}_5$ is the vector following the path and direction of the center of the object to the contact point of the object to the fingertip. Vector $\vec{\boldsymbol{r}}_6$ is the vector that depicts the displacement of the center of the object in the y-direction.

By definition, the vector loop should be closed and therefore the relation between the six vectors is as shown in Equation 2.

$$\vec{\boldsymbol{r}}_1 + \vec{\boldsymbol{r}}_2 + \vec{\boldsymbol{r}}_3 + \vec{\boldsymbol{r}}_4 = \vec{\boldsymbol{r}}_5 + \vec{\boldsymbol{r}}_6 \tag{2}$$

When $\cos(\theta_i)$ and $\sin(\theta_i)$ are abbreviated to c_i and s_i, the vector loop equations can be seen in Equation 3.

$$\begin{cases} l_1 c_1 + l_2 c_2 + l_3 c_3 + l_4 c_4 - l_5 c_5 - l_6 c_6 = 0 \\ l_1 s_1 + l_2 s_2 + l_3 s_3 + l_4 s_4 - l_5 s_5 - l_6 s_6 = 0 \end{cases} \tag{3}$$

The lengths l_i and angles θ_i are defined in Equation 4.

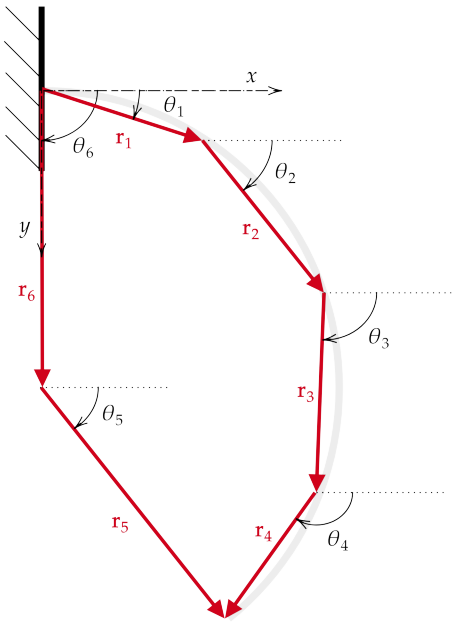

Fig. 4: Vector loop: the vectors $\vec{r}_2$, $\vec{r}_3$ and $\vec{r}_4$ follow the paths and directions of the finger links. Vector $\vec{r}_5$ represents the object. Vector $\vec{r}_6$ represents the displacement of the object in the y-direction.

$$\begin{cases} l_1 = \gamma_1 L \\ l_2 = \gamma_2 L \\ l_3 = \gamma_3 L \\ l_4 = \gamma_4 L \\ l_5 = R \\ l_6 = R + y \end{cases} \quad \begin{cases} \theta_1 = \zeta_1 \\ \theta_2 = \theta_1 + \zeta_2 + \delta\theta_2 \\ \theta_3 = \theta_2 + \zeta_3 + \delta\theta_3 \\ \theta_4 = \theta_3 + \zeta_4 + \delta\theta_4 \\ \theta_5 = \psi - \frac{\pi}{2} + \delta\theta_5 \\ \theta_6 = \frac{\pi}{2} \end{cases} \tag{4}$$

Considering the variable y as an input with incremental steps Δy, the number of unknowns in the vector loop reduces to four, which are $\delta\theta_2$, $\delta\theta_3$, $\delta\theta_4$ and $\delta\theta_5$. However, there are only two equations to solve the kinematics.

To solve this problem, an optimization algorithm is implemented that minimizes the potential energy of the system, as defined in Equation 5. In this optimization process, $\delta\theta_2$ and $\delta\theta_5$ are considered optimization variables that are used to determine the remaining two unknowns, $\delta\theta_3$ and $\delta\theta_4$. In the algorithm the optimization variables are contained in the vector $\vec{\boldsymbol{x}}$, and the unknown deformation angles that are solved are contained in the vector $\vec{\boldsymbol{\delta\theta_{34}}}$ and the vector $\vec{\boldsymbol{\delta\theta}}$ contains all the values of the deformation angles to solve the vector loop in the iteration.

$$V = \frac{1}{2} K_{\theta 2} \delta\theta_2^2 + \frac{1}{2} K_{\theta 3} \delta\theta_3^2 + \frac{1}{2} K_{\theta 4} \delta\theta_4^2 \tag{5}$$

The first step is to set the initial values for the algorithm to set the correct starting point of the algorithm. These initial values are depicted in Table I.

For the displacement of the base joint of the fifth link, the displacement vector y is initialized, which contains the starting

TABLE I: The initial values for the optimization algorithm, containing the initial deformation angles of the mechanism $\vec{\boldsymbol{\delta\theta}}$, the optimization variables $\vec{\boldsymbol{x}}$, and the to-be solved unknown deformation angles $\vec{\boldsymbol{\delta\theta_{34}}}$.

Vector	**Variables**	**Initial values**
$\vec{\boldsymbol{\delta\theta}}$	$[\delta\theta_1 \ \delta\theta_2 \ \delta\theta_3 \ \delta\theta_4 \ \delta\theta_5 \ \delta\theta_6]$	$[0 \ 0 \ 0 \ 0 \ 0 \ 0]$
$\vec{\boldsymbol{x}}$	$[\delta\theta_2 \ \delta\theta_5]$	$[0 \ 0]$
$\vec{\boldsymbol{\delta\theta_{34}}}$	$[\delta\theta_3 \ \delta\theta_4]$	$[0 \ 0]$

y-coordinate y_s, the stepsize Δy, and the end y-coordinate y_e, as shown in Equation 6. The step size can be adjusted to reach the desired accuracy and computational time. The starting point y_s is equal to zero and the endpoint y_e is equal to $2R$ to simulate the full extraction of the object from the gripper.

$$y = [y_s : \Delta y : y_e] = [0 : \Delta y : 2R] \tag{6}$$

As multiple local minima can be found, the optimization variables have upper and lower boundaries, denoted by respectively u_b and l_b, that ensure the correct mechanism configuration. Different types of configurations of the mechanism can occur, wherein the minimization algorithm the same absolute angles are found, but for specific link couples, the configuration is mirrored, resulting in unrealistic solutions, as these results would penetrate the surface of the object. By imposing a constrained range of solutions, the physically plausible configuration is forced.

The boundaries evolve with each iteration, leveraging the outcomes of the previous iteration as a starting point. The constrained space has an upper and lower value of respectively 3 and -3 degrees for $\delta\theta_2$ and the constrained space for $\delta\theta_5$ has an upper and lower value of respectively 15 and -15 degrees. These values are fine-tuned by trial and error while considering not constraining the kinematics, but only forcing the correct configuration. The definition of the boundaries is given in Equation 7. The constrained spaces have a scaling factor c, which is equal to $1000 \cdot \Delta y$, such that correct scaling occurs when a higher or lower value of Δy is used and the relative size of the boundaries stays correct.

$$\begin{bmatrix} l_b \\ u_b \end{bmatrix} = \vec{\boldsymbol{x}} + c \begin{bmatrix} -3 & -15 \\ 3 & 15 \end{bmatrix} \tag{7}$$

The optimization variables are iterated within the interior-point solving algorithm, *fmincon*, in MATLAB. The objective function is to find the minimal potential energy as given in Equation 5. For all instances of the optimization values the potential energy will be calculated and the values of the optimization variable that has minimal potential energy, within specified tolerances, determine the values of $\delta\theta_2$ and $\delta\theta_5$ are used in solving the vector loop equations, as given in Equation 3, to find the remaining unknown values, $\delta\theta_3$ and $\delta\theta_4$.

At the end of each iteration, the values of the optimization

vector $\vec{x}$ and objective vector $\vec{\delta\theta_{34}}$ are stored and updated with the solved values of $\delta\theta_2$, $\delta\theta_3$, $\delta\theta_4$ and $\delta\theta_5$. This process is iterated for each displacement of the object in the y-direction, with the specified stepsize Δy.

C. Kinetics

The result of the optimization is the kinematic configuration for each displacement y, which is used to determine the kinetics of the mechanism. To determine the maximum pull-out force of the mechanism only the fourth segment of the PRB mechanism is required, which is the segment at which contact is made between the object and the finger. A free-body diagram of the fourth PRB segment is illustrated in Figure 5.

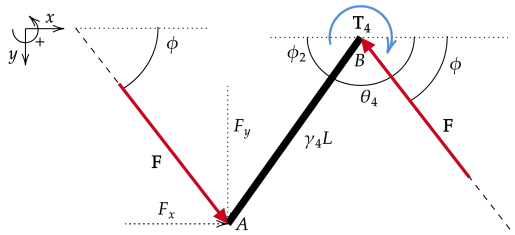

Fig. 5: Free body diagram of the fourth PRB link: the force F at an angle ϕ, applied by the object on the fourth link of the PRB linkage, has an equal reaction force F at the joint between the third and fourth link. Furthermore, at this same joint, a reaction torque T_4, caused by the deformation of the torsion spring, is applied.

In the free-body diagram, $\gamma_4 L$ is the length of the fourth link in the PRB mechanism, and the angles ϕ and ϕ_2 are respectively the angle of the reaction force on the fourth link of the mechanism and the angle of the fourth link with respect to the x-axis as defined in Equation 8.

$$\begin{cases} \phi = \delta\theta_5 \\ \phi_2 = \pi - \delta\theta_4 \end{cases} \tag{8}$$

Furthermore, the force F is the reaction force between the object and the fingertip, and T_4 is the torque that results from the torsional deformation of the PRB torsion spring at the third joint of the PRB mechanism. This torque is defined in Equation 9.

$$T_4 = K_{\theta 4}\delta\theta_4 \tag{9}$$

Applying moment balance at equilibrium allows the derivation of the relation for the force in the y direction, e.g. the pull-out force. The relation for the pull-out force F_y is given in Equation 10.

$$F_y = \frac{T_4}{\gamma_4 L(n\cos(\phi_2) + \sin(\phi_2))} \tag{10}$$

In the relation for the pull-out force, the parameter n is used to make the equation more readable, which equals equals the ratio between the x- and y-components of the tip reaction force F, where this ratio is defined as shown in Equation 11.

$$n = \frac{F_y}{F_x} = \tan(\phi) \tag{11}$$

By following the procedure that is described in this section, the first and main sub-goal of this paper is accomplished, which contains determining the pull-out force for a defined mechanism and object in a specified load case.

III. Experimental Validation

The goal of this experimental validation is to recreate an accurate real-world representation of the model, where the results of the model, which are the reaction forces on the tip of the model, for several design parameters ψ and h can be compared to the real-world forces on test pieces with similar design parameters. The key elements to accomplish this goal are to design a test setup that measures the reaction forces at the support of the mechanism and by moving an object in the y-direction to simulate the pull-out motion that is modeled. This is depicted in the basic concept of the setup in Figure 6. The realized test setup with a description of its main components can be found in Figure 7.

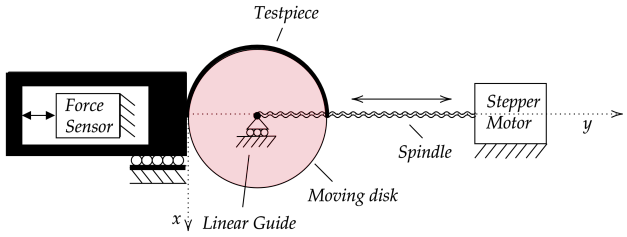

Fig. 6: Illustration of the test setup: the moving disk is extracted in the y-direction from the curved testpiece with a linear stage consisting of a linear guide and a spindle, driven by a stepper motor. The reaction forces on the freely moving testpiece are measured by compressing on a force sensor mounted to the environment.

A. Test setup

The test setup can be categorized into three main sections:

1) Motion stage: The moving object, disk, that is mounted on a linear guiding stage and is actuated via a spindle to a stepper motor.
2) Force measurement stage: The section where the test-pieces are mounted and connected to the load cells such that the reaction forces can be measured.
3) Measurement devices: The different sensors in the test setup, such as the load cells to measure the reaction force and a distance sensor to measure linear displacement of the motion stage.

These sections are visualized in Figure 7, where also a numbered overview of the setup is given.

The motion stage consists of a disk (1), turned from aluminum bars, with a radius of 80 mm and a height of 50 mm (excluding the axis), which represents the circular object that is extracted from the mechanism. Two KP8

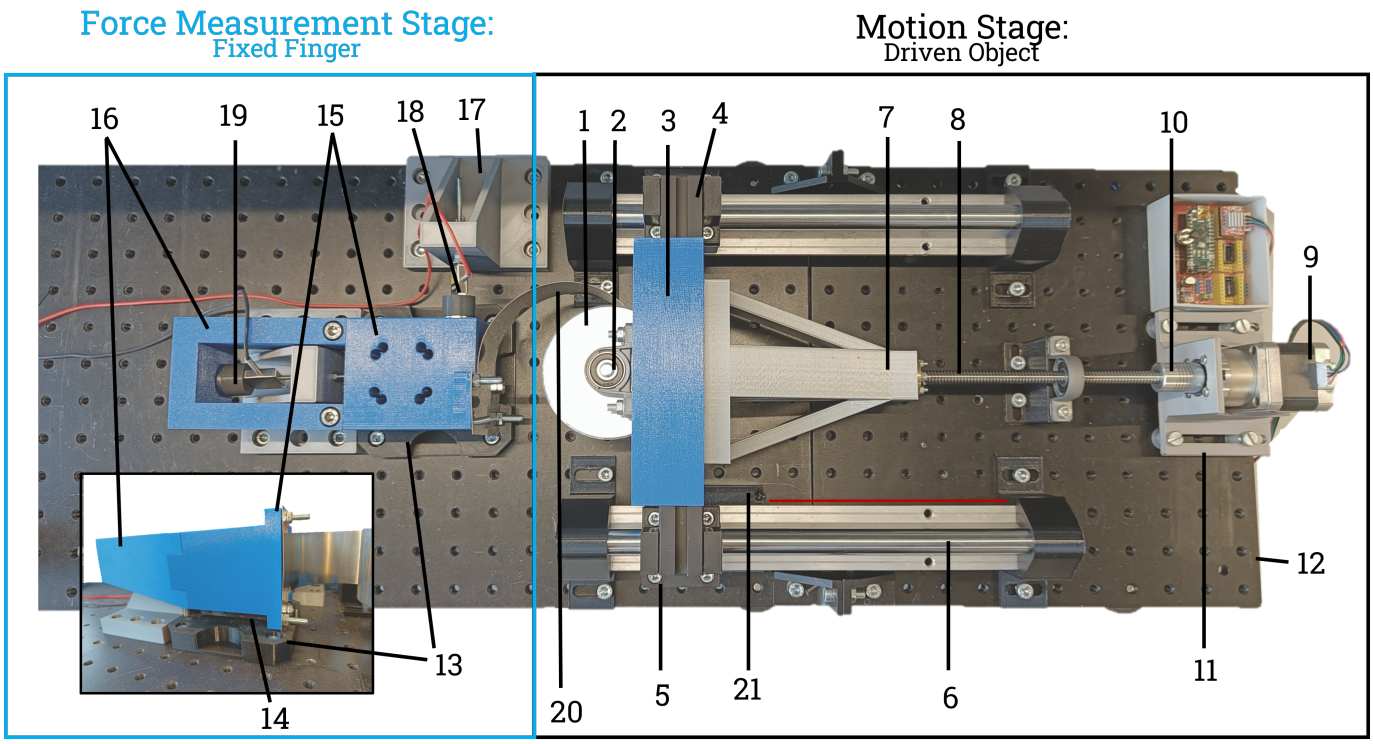

Fig. 7: Numbered overview of the test setup: The motion stage (black) consists of a driven object (1) on a linear slider (5, 6) driven by a spindle (8) and a stepper motor (9) with bellow (10) without friction due to bearings (2). The force measurement stage (blue), consists of the testpiece (20) connected to a two-piece mounting hub (15, 16) on a linear slider (14). The measurement devices consist of a load cell for measuring reaction forces in the x- and y-direction (18, 19) and a laser sensor (21) for measuring the displacement of the object. The setup consists of 3D-printed mounting structures (3, 7, 11, 13, 17), optical rails (4), and a main breadboard (12).

ball bearings (2) ensure frictionless rotation of the disk. A 3D-printed structure (3) connects the bearings and aligns the disk's top surface parallel to the xy-plane. THORLABS XE25L225/M optical rails (4), linked to SBR16UU linear bearings (5), enhance the dynamic framework. The spindle (8), which is connected to the disk via a 3D-printed structure (7), connects to the NEMA17-05GM stepper motor (9) via a bellow coupling (10). The motor is supported by a 3D-printed stage (11) that rests on soft plastic spacers to reduce any more vibrations and is controlled by an Arduino Nano board and an A4988 stepper driver via software called UGS Platform. All parts are connected with M6 bolts and nuts.

The force measurement stage consists of a 3D-printed baseplate (13), which is mounted on top of the THORLABS MB2020/M aluminum breadboard (12) and provides connection points for the PMB RTS-2065 linear motion stage (14) in both the x- and y-direction, such that in both directions reaction forces can be measured. Connected via M3 screws, the main 3D-printed testpiece mounting hub features two sections. The main section (15) remains connected to the linear motion stage, serving as the test piece hub. For testing in the y-direction, the second section (16) connects to the first section via M6 bolts and nuts, forming a saddle to enable compression against the y-direction load cell. The load cells for the x-direction (18) and for the y-direction (19) are mounted on stiff 3D-printed structures (17). The testpieces (20) are connected to the main hub. In the validation, stainless steel and PLA testpieces are used. The stainless steel testpiece connects to the main hub with M4 bolts and nuts. The PLA testpiece is integrated directly into the solid 3D-printed hub.

To validate the kinetics of the model the reaction force and displacement of the disk have to be measured. The forces are measured by using a Futek LSB200 load cell of a resolution of 22 N and 44 N for respectively the measurement in y-direction and x-direction. Load cells incorporate a roller ball mount to ensure a point contact, align with the measuring direction, and prevent friction during tangential movement.

The displacement of the object is measured by using a Micro-Epsilon ILD1420-500 laser sensor (21), which is enclosed in a 3D-printed structure and attached with M6 bolts to the lower optical rails. The laser targets the linear guide mount, offering a suitable black smooth surface for optical measurements. The signals of the measurement devices are processed using an NI USB 6008 I/O device. Using

LABVIEW software, analog sensor signals are converted into readable digital data for plotting signal measurements over time.

B. Conducting the experiment

The measurements are conducted with testpieces made of polylactic acid (PLA) and stainless steel grade 1.4310.

The PLA testpiece was 3D printed with a hundred percent infill to make the solid as homogeneous as possible. Due to the non-homogeneous characteristics of the 3D printed PLA, a small test was done to determine the Young's modulus for the simulation of a 3D printed PLA, resulting in a Young's modulus for PLA of 2.55 GPa. The PLA testpiece has an enclosing angle of 180 degrees, a thickness of 2 mm, a width of 50 mm, and a radius of 40 mm, which matches the width and radius of the disk.

For the stainless steel testpiece, laser-cut stainless steel material with a Young's modulus of 195 GPa is shaped into a curved gripper finger with an enclosing angle of 180 degrees, a thickness of 0.3 mm, a width of 50 mm and a radius of 40 mm.

The testpieces and the mounting hub are connected to the PMB RTS-2065 linear slider in the direction that provides the correct degree of freedom for measuring the reaction forces in either the x- or y-direction. First, reaction forces in the y-direction are recorded, followed by measurements in the x-direction.

The experimental setup involves calibrating load cells for zero-force output and placing the disk at the initial position, such that the testpiece is in the undeformed state. In LABVIEW the correct sensors are selected, data-saving is enabled and with the UGS Platform software, the object is moved in the y-direction to measure the reaction forces and create the force-displacement graphs. These measurements are conducted ten times for each direction and each testpiece, minimizing random precision errors. The experimental data is processed in MATLAB to generate the desired plots and compare the results with the simulated result. This analysis is done by determining the maximum values of both the experimental and simulated results, as well as the error between these maximum values. For determining this error the median of the maximum values of the experimental results is used.

IV. Parametric study

The validated model can be used to do a parametric study, where the model is executed multiple times with a defined load case and changing values for the design parameters ψ and h. This is called a parametric sweep. For all combinations of assigned values for these parameters the model is executed, giving insight into the relation between these parameters and which combination of these values can carry a certain payload, such as the weight of a tomato. By doing this parametric sweep for multiple materials, relevant design charts are generated.

In the parametric study, certain values remain constant throughout the model iterations defined by the load case. In this study, a load case is chosen that is based on the design of an enclosing gripper that functions in a cluttered environment with tomatoes. The gripper consists of three fingers, which are equally spaced to prevent the object from falling out. The radius and mass of the object are derived from typical tomato properties, and the gripper fingers have a small width. The constant values that are used for this parametric study are found in Table II.

TABLE II: The constant values that are used in the parametric study.

Constant	Value	Unit	Description
R	30	$[mm]$	The radius of the object.
m	100	$[g]$	The mass of the object.
g	9.81	$[m/s^2]$	The gravitational constant.
n_f	3	$[-]$	Number of fingers.
w	20	$[mm]$	Width of a gripper finger.

The main variables of the parametric study are the design parameters, which are the enclosing angle ψ and finger thickness h. Furthermore, the Young's modulus, E, is also considered a variable as the study covers both PLA and stainless steel as materials.
The array values that were used for the sweep can be found in Table III.

TABLE III: The array values that are used in the parametric sweep.

Variable	Values sweep 1	Values sweep 2	Unit
E	3.5 (PLA)	195 (Stainless steel)	$[GPa]$
h	[0.5 : 0.05 : 2.5]	[0.1 : 0.01 : 1]	$[mm]$
ψ	[135 : 5 : 180]	[135 : 5 : 180]	$[^\circ]$

For each of the three values that are shown in Table III all combinations of these values are made and for each combination the model, as described in section II, is executed. For each iteration, the maximum value of the pull-out force F_y is stored in a dataset. These maximum values are plotted against the array of thickness values, resulting in force-thickness plots with nonlinear lines for each enclosing angle instance. A dummy plot of such a result is depicted in Figure 8. Within this plot, a force-limit line is incorporated, representing the pull-out force limit for a specific load case, defined as $F_z = mg$.

By interpolating the nonlinear maximum values, the intersection points between the force-thickness plots and the force limit are calculated. These points yield a relationship between thickness and enclosing angle for the given load case and are plotted, through which a 3rd-degree polynomial is fitted to create the desired design chart.

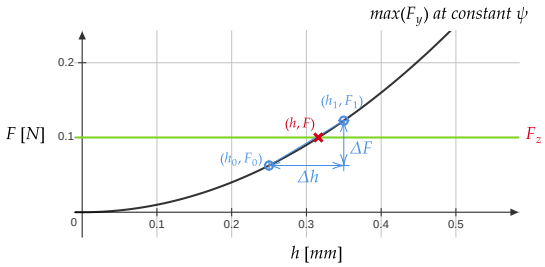

Fig. 8: A dummy plot of the maximum pull-out force with respect to the thickness (black line), for each value of the enclosing angle, and the pull-out force of the object in a certain load case (red line), which is defined as the force limit. The difference between the x-axis values (h_0 and h_1) and y-axis values (F_0 and F_1) of resp. the thickness and the maximum values of the force are shown for two coordinates in the plot in order to calculate the interpolation values.

V. Results

A. Experimental validation

The force-deflection plot displayed in Figure 9 presents the experimental and simulated results. In this graph the red line depicts the reaction force in the y-direction and the blue line depicts the reaction force in the x-direction. The continuous line represents the simulated result and the dotted lines represent the measured results. In Figure 9a the result is shown for a testpiece with PLA material and in Figure 9b for a testpiece of stainless steel material. From both results, it is observed that the trend of the simulated result is very similar to the measured result, where only a difference in the amplitude of the plot is visible, and at the end of the simulated result the reaction force in the x-direction quickly in contrast to the measured result. Furthermore, the shape of the simulated result for the testpiece of stainless steel material is a little off for the reaction force in both the x- and y-direction in comparison to the measured result, while for the results of the testpiece of PLA material the shape of the simulated result is similar to the measured result.

It is observed that the maximum value of the reaction force in the x-direction is at a displacement of approximately 45 mm and the maximum value of the reaction force in the y-direction is reached at a displacement of approximately 15 mm. These maximum values of the simulated and measured results can be found in Table IV as well as the error between these maximum values of the simulation and the experiment. The errors are depicted in both the absolute error between the maximum results of the simulated and measured results and the percentile error, which is determined as a ratio of the absolute error and the measured result. The error of the pull-out force, which is the reaction force in the y-direction is around 18 percent, while the error of the reaction force in the x-direction is smaller, approximately 13 percent, for the PLA test and much bigger, approximately 32 percent, for the stainless steel test.

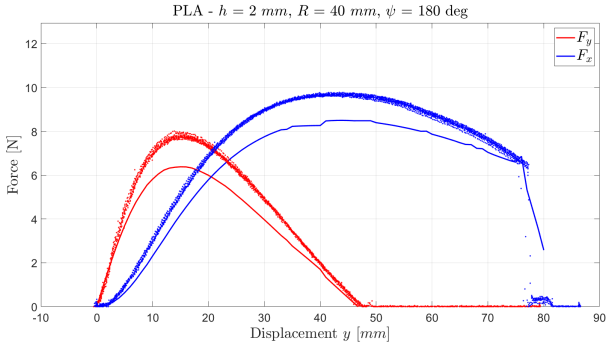

(a) Resulted reaction forces for the polylactic acid (PLA) testpiece.

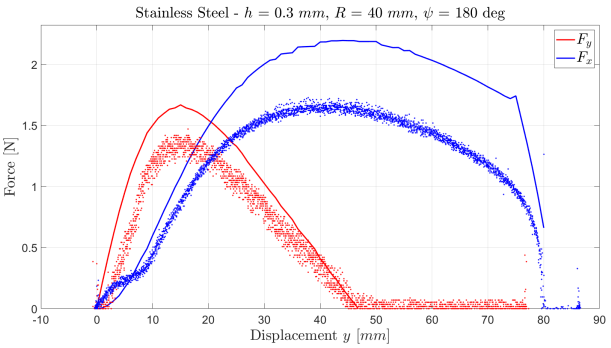

(b) Resulted reaction forces for the stainless steel 1.4310 testpiece.

Fig. 9: Simulated and measured results of the tip reaction force development in the x-direction (blue) en y-direction (red) when an object is extracted from the gripper in the y-direction. The continuous line is the simulated result and the dots are the measured results.

TABLE IV: The maximum values for both simulated and measured results, for both the tests with PLA and stainless steel as material, along with the corresponding errors. The errors are presented as absolute differences between the maximum values of the simulated and measured results ($e_{|\Delta|}$) and as a percentage of the measured values (e).

		Sim. $[N]$	**Exp.** $[N]$	$e_{\lvert\Delta\rvert}$ $[N]$	e [%]
PLA	max F_x	8.5036	9.6960	1.1924	12.30
	max F_y	6.3847	7.7795	1.3948	17.93
Stainless steel	max F_x	2.1956	1.6670	0.5286	31.71
	max F_y	1.6540	1.4000	0.2540	18.14

B. Parametric study

The results of the parametric sweep for the PLA finger can be seen in Figure 10a and for the stainless steel finger in Figure 10b. In these plots, the nonlinear lines represent the maximum values of the pull-out force for each instance of the finger thickness h, in which the enclosing angle ψ is kept at a constant value. Ten instances of this plot for a value of the enclosing angle ranging from 135 degrees to 180 degrees are depicted in the graph. The force limit, which is the payload of the tomato, is depicted in black and is divided by the number of fingers that the gripper has. The red crosses depict the

intersection points between the ten plots and the force limit, resulting in the ultimate combination for a value for h and ψ where the finger can hold the payload.

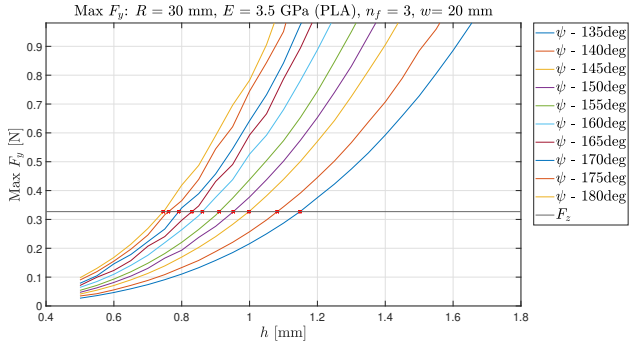

(a) Parametric results for polylactic acid (PLA) as chosen material.

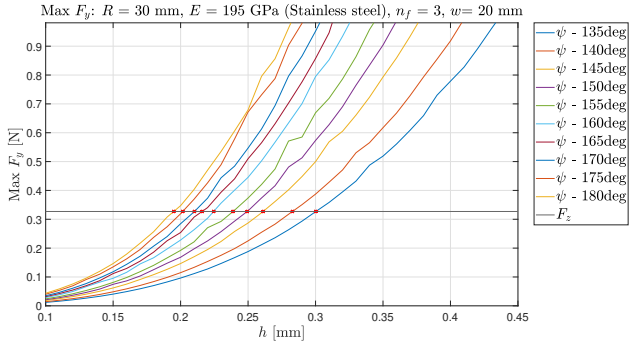

(b) Parametric results for stainless steel 1.4310 as chosen material.

Fig. 10: Relation between the maximum pull-out force F_y and the thickness h, for ten different constant values of the enclosing angle ψ. The black line depicts the force limit in the parametric study, based on the payload of the object. The red crosses depict the intersection points between the maximum force-thickness plot and the force limit, resulting in the ultimate combination for a value for h and ψ where the finger can hold the payload.

The generated design chart, that relates the thickness h and enclosing angle ψ for the described load case, is depicted in Figure 11 for both PLA and stainless steel as material. The circles represent the intersection points. A 3rd-degree polynomial is fitted for these intersection points, which is depicted in the figure by the continuous lines, and shows a nonlinear relation between the enclosing angle and finger thickness can be observed.

VI. Discussion

A. Experimental results

The results obtained by the experimental setup show a similar trend in the force development as the simulated results, showing that the model predicts the direction of the reaction force between the object and the fingertip accurately. Furthermore, recognizable locations of the force development, such as the maximum values and the intersection points with the x-axis of the plot, match both the measured and simulated

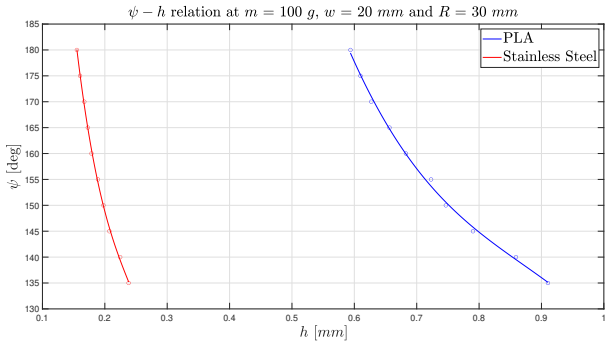

Fig. 11: Design chart: Relation between thickness and enclosing angle for PLA and stainless steel. The circles represent the intersection points of the maximum force plots with the force limit. The continuous line is the plot of the 3rd-degree fitted polynomial. This line depicts the limit for a combination of design parameters for which the design can hold the payload that is defined in the title of the plot.

results. This shows that the maximum reaction force in the x-direction and the change of direction in the force in the y-direction is at a displacement of 45 mm, which is a little further than the radius of the object. Furthermore, it is observed that the measured reaction force in the y-direction has no negative component, which is explained by the fact that the load cells were only compressed when the testpiece was being pulled due to the extraction of the object, while after 45 mm displacement the testpiece was pushed back by the object, resulting in loss of contact to the load cells.

However, also errors are observed between the measured and simulated results, primarily visible in the magnitude of the force and the deviating trend of the force development for the stainless steel testpiece. These errors are categorized as systematic errors and measurement errors, where the systematic errors lead to a scaling error of the overall results and the measurement errors lead to discrepancies between the results for each experiment iteration.

First, systematic errors arise due to incorrect assignment of the values for the parameters in the model, discrepancies due to manufacturing, and due to the calibration and resolution of the load cells.

The main discrepancies in the parameters of the model are in the geometrical parameters and the material parameters. Discrepancies in the geometrical parameters, such as the enclosing angle and thickness of the finger, arise while manufacturing the testpieces. For the PLA testpiece, this contains errors due to the tolerances, support types and nozzle size of the 3D printer. For the stainless steel, this contains errors in bending the leaf spring, which is hard to do for an accurate curvature, and errors due to the tolerance and heat settings of the laser cutter. Both manufacturing

methods also influence the material properties, such as the Young's modulus, of the testpieces. For the PLA testpiece, this contains non-homogeneity of the material, due to the 3D printed layers. For the stainless steel testpiece due to the heat of the laser cutter material properties are influenced. A difference between the modeled and actual Young's modulus and geometrical parameters therefore explains why the experimental result of the PLA test is higher than the simulated result, while for the stainless steel testpiece, the experimental result is lower than the simulated result.

Furthermore, in Figure 9b a notable spread is observed in the experimental result, which is explained due to the resolution of the load cells, which were designed for loads up to 22 N for the y-direction and 44 N for the x-direction, while the actual reaction forces are not exceeding 2 N. Employing higher-resolution load cells would enhance accuracy. Also, the calibration of the load cells is a factor that could result in small deviations.

Lastly, measurement errors occur, particularly arising from misalignments in the setup. The setup is accurately aligned, but for each iteration, the testpiece has to be aligned such that initially no reaction force is measured, which is hard as small deviations in the alignment have a significant influence on the measured reaction force, especially for the stainless testpiece with an imperfect curvature. Furthermore, the force measurement stage is rotated 90 degrees when changes the measurement direction changes, resulting in small misalignments during this operation. These measurement errors, therefore, explain the deviations in the force development between the measured and simulated results, especially in the results with the stainless steel testpiece.

The contribution of the systematic or measurement errors to the total error value can be determined by using the scaling factor C_e. The scaling factor is determined as given in Equation 12.

$$C_e = \frac{F_y^e}{F_y^s} \tag{12}$$

In this equation F_y^s is the simulated result of the maximum pull-out force and F_y^e is the median of the measured results of the maximum pull-out force. By multiplying the simulated result by this scaling factor the error between the measurements and simulation in the y-direction becomes zero, as can be seen in Figure 12, and therefore the error between the measurements of reaction forces in the x-direction and in the y-direction can be determined. The remaining error values are then assumed to be systematic errors.
The scaling factor for the measurements with the stainless steel testpiece is equal to 0.8464 and results in a measurement error between the resulted reaction forces in x- and y-direction of 8.75 %.
The scaling factor for the measurements with the PLA testpiece is equal to 1.2185 and results in a measurement error between the resulted reaction forces in x- and y-direction of 0.0687 %.

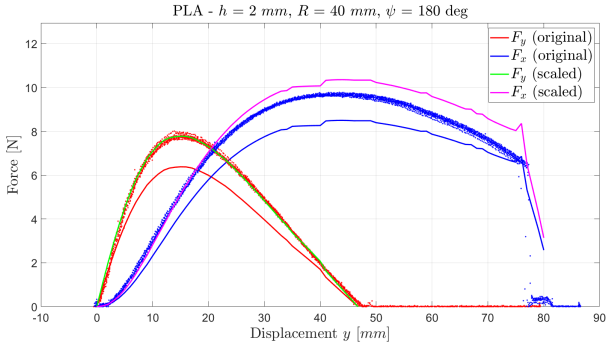

(a) Resulted and scaled reaction forces for the polylactic acid (PLA) testpiece, where $C_e = 1.2185$.

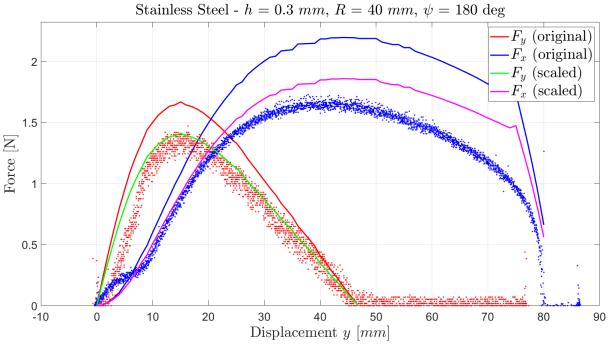

(b) Resulted and scaled reaction forces for the stainless steel 1.4310 testpiece, where $C_e = 0.8464$.

Fig. 12: Influence of the systematic errors on the results: the results scaled with error scaling factor C_e are depicted by the green and magenta lines. The original force results are depicted by the blue and red lines.

From Figure 12 it can be seen that when the systematic errors are reduced, which would, for instance, be possible by using the correct Young's modulus, the determination of the pull-out force over the whole displacement is very accurate and the determination of the reaction force in the x-direction is very accurate for approximately the first 30 mm of displacement, which is 75 % of the radius of the object and therefore the most important section of the simulation when it is implemented in design.

B. Parametric study

The results of the parametric study, depicted in Figure 10, show a nonlinear correlation between the maximum pull-out force and the thickness. The distance between these plots for different enclosing angles increases when the forces become higher, showing an increased impact of the design parameters h and ψ for higher forces. As the force limit is dependent on the number of fingers that are used, engineers can determine the appropriate number of fingers by identifying intersection points between this force limit and nonlinear plots within the desired range. Figure 10 functions therefore as a valuable tool

for an engineer to determine the wide range of possibilities of design choices when the payload of the object is known.
The resulted design chart, which is depicted in Figure 11, illustrates a nonlinear relation between the main design parameters h and ψ. For stainless steel fingers, thickness values exhibit minimal change with varying enclosing angles, while for PLA, the effect is more pronounced. Engineers can select the value of the most crucial design parameter at the limit, determining the value for the other design parameter accordingly. Additionally, the chart helps the engineer to decide which material would fit the best to the desired design.

However, improvements to obtain better results can be made, as the result of the parametric sweep can be more accurate and smooth if the range of interest for the swept parameters is determined, such that a more local study could be done. While linear interpolation is currently used to find intersection points between maximum force plots and the force limit, it introduces some deviations.
Another method to increase accuracy and smoothness in the parametric study is to use more parameters and therefore a higher resolution array of parameters, although this comes with the cost of a higher computational time.
Lastly, an assumption is made that the intersection points can be fitted by a 3rd-degree polynomial for the design chart, but another order of fitting could result in a more accurate approximation of the trend.

C. Extendability and future research

The problem analyzed in this paper was the stationary lifting of a circular object by two initially-curved gripper fingers based on agri-food grippers for tomatoes. However, the model can be used in other applications where similarly shaped objects need to be grasped, such as medical grippers that grasp soft or tissue-like objects.

The model can also be extended to handle different-shaped objects. For instance, the length of the fifth link, which now represents the radius of the circular object, can be considered a variable rather than a constant, such that it represents non-circular objects or compliant objects, which could mimic the non-rigid behavior of a soft object, such as a tomato.
Moreover, the model can be extended to more complex designs, such as incorporating fingers with multiple interconnected backbones. These backbones are kinematically related and therefore the kinetics can be determined when the configuration of a single backbone is modeled.

Future research could focus on the addition of friction of the object and finger on the behavior of the pull-out force and different extraction directions of the object by placing the base of the fifth link on a planar joint instead of a linear slider. Furthermore, a dynamic study of the model could be done, by implementing the force caused by the acceleration of the object and the mass of the fingers. However, this adds complexity as in this case the force distribution and deformation in a multi-finger gripper is different for each finger when for instance the gripper is accelerated in the x-direction.

Lastly, the parametric study in this paper is evaluated primarily for the thickness and enclosing angle of a gripper finger, for two different materials. However, this could be evaluated for other design parameters, such as multiple values for the Young's modulus for different materials, different cross-sections of the finger, resulting in a different area moment of inertia, different widths of the finger, and different object dimensions and weight. The focus of the design parameters that are used in the parametric study can therefore shift according to the main parameters of interest.

VII. Conclusion

The goal of this study was defined by two main sections, which are the determination of the pull-out force and the parametric study.

First, by using an existing Pseudo-Rigid Body model for initially-curved beams as the foundation and adding an extra link to mimic the extraction of an object from initially curved gripper fingers, the pull-out force of an object being extracted from such fingers is determined to give insight into the payload of a gripper for a defined load case. The payload and load case were defined based on the dimensions and weight of a regular tomato being extracted from a gripper. The determination of the pull-out force is validated by designing a test setup by which the reaction forces at the base of an initially-curved testpiece in the x- and y-direction are measured, while an object, as a disk, is extracted in the y-direction. This is done for multiple testpieces, one of PLA and one of stainless steel. The results showed a similar trend in the force-deflection graph between the simulated and experimental results with an error of the maximum force values of approximately 18 $\%$ for the reaction force in the y-directions for both the PLA and stainless steel testpiece, and an error of approximately 12 $\%$ for the reaction force in the x-direction for the PLA testpiece and approximately 32 $\%$ for the stainless steel testpiece.

Secondly, the developed model is used to do a parametric study, where for multiple array values of the enclosing angle ψ, and thickness h a parametric sweep is done. By determining the intersection points of the plots, where the maximum pull-out force is related to the thickness for different enclosing angles, and the force limit, which is determined by a load case where a gripper of the fingers holds a tomato of 100 g, the relation between the design parameters h and ψ are determined and depicted in a plot.

With this result, the goal of this study is accomplished, as the relation between the important design parameters is determined with a model-based approach. Therefore, the results of

this paper provide valuable design charts to help and inspire engineers in designing innovative compliant grippers.

REFERENCES

[1] N. Elango, N. Obianuju Onubogu, and S. Ragunathan, "Experimental Study of Non-Contact Robot Gripper for Food Industries," *Applied Mechanics and Materials*, vol. 232, pp. 392–397, 2012, conference Name: Mechanical and Aerospace Engineering, ICMAE2012 ISBN: 9783037855140 Publisher: Trans Tech Publications Ltd. [Online]. Available: https://www.scientific.net/AMM.232.392

[2] "Ventose - Vuototecnica 2023." [Online]. Available: https://www.vuototecnica.net/products.php?cat=1

[3] S. Davis, J. W. Casson, R. J. Moreno Masey, M. King, J. O. Gray, and D. G. Caldwell, "Robot prototyping in the design of food processing machinery," *Industrial Robot: An International Journal*, vol. 34, no. 2, pp. 135–141, Jan. 2007, publisher: Emerald Group Publishing Limited. [Online]. Available: https://doi.org/10.1108/01439910710727487

[4] G. Fantoni, "Grasping Everything," Nov. 2013.

[5] "Best Soft Gripper Manufacturer in 2023 - SoftGripping," Apr. 2020, running Time: 270. [Online]. Available: https://soft-gripping.com/

[6] "MultiChoiceGripper | Festo USA." [Online]. Available: https://www.festo.com/us/en/e/about-festo/research-and-development/bionic-learning-network/highlights-from-2013-to-2014/multichoicegripper-id_33524/

[7] roboapp, "Meat Gripper." [Online]. Available: https://www.appliedrobotics.com/products/automation/grippers/meat-gripper/

[8] L. L. Howell and S. B. Magleby, *Handbook of Compliant Mechanisms*. John Wiley Sons, 2013.

[9] L. L. Howell, "Compliant Mechanisms," in *21st Century Kinematics*. London: Springer, 2013.

[10] W. Crooks, G. Vukasin, M. O'Sullivan, W. Messner, and C. Rogers, "Fin Ray® Effect Inspired Soft Robotic Gripper: From the RoboSoft Grand Challenge toward Optimization," *Frontiers in Robotics and AI*, vol. 3, 2016. [Online]. Available: https://www.frontiersin.org/articles/10.3389/frobt.2016.00070

[11] S. Min and Y. Kim, "Topology Optimization of Compliant Mechanism with Geometrical Advantage," *JSME International Journal*, vol. 47, no. 2, 2004.

[12] B. Friederich, "Design and Validation of a Manoeuvering Caging Gripper for Cluttered Environments — TU Delft Repositories — resolver.tudelft.nl," http://resolver.tudelft.nl/uuid:f20e97b0-97a4-43b7-91ec-1acb3bca72ac, 2022, [Accessed 05-02-2024].

[13] J. Luong, P. Glick, A. Ong, M. S. deVries, S. Sandin, E. W. Hawkes, and M. T. Tolley, "Eversion and Retraction of a Soft Robot Towards the Exploration of Coral Reefs," in *2019 2nd IEEE International Conference on Soft Robotics (RoboSoft)*, Apr. 2019, pp. 801–807.

[14] L. H. Blumenschein, M. M. Coad, D. A. Haggerty, A. M. Okamura, and E. W. Hawkes, "Design, Modeling, Control, and Application of Everting Vine Robots," *Frontiers in Robotics and AI*, vol. 7, 2020. [Online]. Available: https://www.frontiersin.org/articles/10.3389/frobt.2020.548266

[15] T. Abrar, F. Putzu, A. A. A. Rizqi, G. Hareesh, and K. Althoefer, "Highly Manoeuvrable Eversion Robot Based on Fusion of Function with Structure," Feb. 2021.

[16] "Pre-Formed Vine Robot," May 2018. [Online]. Available: https://www.vinerobots.org/build-one/pre-formed-vine-robot/

[17] J. W. Booth, D. Shah, J. C. Case, E. L. White, M. C. Yuen, O. Cyr-Choiniere, and R. Kramer-Bottiglio, "OmniSkins: Robotic skins that turn inanimate objects into multifunctional robots," *Science Robotics*, vol. 3, no. 22, p. eaat1853, Sep. 2018, publisher: American Association for the Advancement of Science. [Online]. Available: https://www.science.org/doi/10.1126/scirobotics.aat1853

[18] T. Hiramitsu, K. Suzumori, H. Nabae, and G. Endo, "Experimental Evaluation of Textile Mechanisms Made of Artificial Muscles," in *2019 2nd IEEE International Conference on Soft Robotics (RoboSoft)*, Apr. 2019, pp. 1–6.

[19] A. Zulifqar, T. Hua, and H. Hu, "Development of uni-stretch woven fabrics with zero and negative Poisson's ratio," *Textile Research Journal*, vol. 88, no. 18, pp. 2076–2092, Sep. 2018, publisher: SAGE Publications Ltd STM. [Online]. Available: https://doi.org/10.1177/0040517517715095

[20] A. Orita and M. R. Cutkosky, "Scalable Electroactive Polymer for Variable Stiffness Suspensions," *IEEE/ASME Transactions on Mechatronics*, vol. 21, no. 6, pp. 2836–2846, Dec. 2016, conference Name: IEEE/ASME Transactions on Mechatronics.

[21] P. T. Phan, M. T. Thai, T. T. Hoang, J. Davies, C. C. Nguyen, H.-P. Phan, N. H. Lovell, and T. N. Do, "Smart textiles using fluid-driven artificial muscle fibers," *Scientific Reports*, vol. 12, no. 1, p. 11067, Jun. 2022, number: 1 Publisher: Nature Publishing Group. [Online]. Available: https://www.nature.com/articles/s41598-022-15369-2

[22] Y. Elsayed, C. Lekakou, T. Ranzani, M. Cianchetti, M. Morino, A. Arezzo, A. Menciassi, T. Geng, and C. M. Saaj, "Crimped braided sleeves for soft, actuating arm in robotic abdominal surgery," *Minimally Invasive Therapy & Allied Technologies*, vol. 24, no. 4, pp. 204–210, Jul. 2015, publisher: Taylor & Francis _eprint: https://doi.org/10.3109/13645706.2015.1012083. [Online]. Available: https://doi.org/10.3109/13645706.2015.1012083

[23] University of Minnesota Wearable Technology Lab, "Active Auxetic Fabrics for Self-Fitting Clothing," Jan. 2020. [Online]. Available: https://www.youtube.com/watch?v=PttK2Z-LJ2M

[24] G. Hao, J. Yu, and H. Li, "A brief review on nonlinear modeling methods and applications of compliant mechanisms," *Frontiers of Mechanical Engineering*, vol. 11, no. 2, pp. 119–128, Jun. 2016. [Online]. Available: https://doi.org/10.1007/s11465-016-0387-9

[25] M. H. Dado, "Variable parametric pseudo-rigid-body model for large-deflection beams with end loads," *International Journal of Non-Linear Mechanics*, vol. 36, no. 7, pp. 1123–1133, Oct. 2001. [Online]. Available: https://www.sciencedirect.com/science/article/pii/S0020746200000767

[26] V. K. Venkiteswaran and H.-J. Su, "Pseudo-rigid-body models for circular beams under combined tip loads," *Mechanism and Machine Theory*, vol. 106, pp. 80–93, Dec. 2016. [Online]. Available: https://www.sciencedirect.com/science/article/pii/S0094114X16301847

[27] V. Kalpathy Venkiteswaran and H.-J. Su, "A Versatile 3R Pseudo-Rigid-Body Model for Initially-Curved and Straight Compliant Beams of Uniform Cross-Section," *Journal of Mechanical Design*, vol. 140, Jun. 2018.